

9-14-2017

Laser Heating of Graphite and Pulsed Laser Ablation of Titanium and Aluminum

William A. Bauer

Follow this and additional works at: <https://scholar.afit.edu/etd>

Part of the [Optics Commons](#)

Recommended Citation

Bauer, William A., "Laser Heating of Graphite and Pulsed Laser Ablation of Titanium and Aluminum" (2017). *Theses and Dissertations*. 1616.

<https://scholar.afit.edu/etd/1616>

This Dissertation is brought to you for free and open access by the Student Graduate Works at AFIT Scholar. It has been accepted for inclusion in Theses and Dissertations by an authorized administrator of AFIT Scholar. For more information, please contact richard.mansfield@afit.edu.



**LASER HEATING OF GRAPHITE AND PULSED LASER ABLATION OF
TITANIUM AND ALUMINUM**

DISSERTATION

William A. Bauer, Captain, USAF

AFIT-ENP-DS-17-S-020

**DEPARTMENT OF THE AIR FORCE
AIR UNIVERSITY**

AIR FORCE INSTITUTE OF TECHNOLOGY

Wright-Patterson Air Force Base, Ohio

DISTRIBUTION STATEMENT A.
APPROVED FOR PUBLIC RELEASE; DISTRIBUTION UNLIMITED.

The views expressed in this thesis are those of the author and do not reflect the official policy or position of the United States Air Force, Department of Defense, or the United States Government. This material is declared a work of the U.S. Government and is not subject to copyright protection in the United States.

AFIT-ENP-DS-17-S-020

LASER HEATING OF GRAPHITE AND PULSED LASER ABLATION OF
TITANIUM AND ALUMINUM

DISSERTATION

Presented to the Faculty

Department of Engineering Physics

Graduate School of Engineering and Management

Air Force Institute of Technology

Air University

Air Education and Training Command

In Partial Fulfillment of the Requirements for the

Degree of Doctor of Philosophy

William A. Bauer, BS, MS

Captain, USAF

August 2017

DISTRIBUTION STATEMENT A.
APPROVED FOR PUBLIC RELEASE; DISTRIBUTION UNLIMITED.

AFIT-ENP-DS-17-S-020

LASER HEATING OF GRAPHITE AND PULSED LASER ABLATION OF
TITANIUM AND ALUMINUM

William A. Bauer, BS, MS
Captain, USAF

Committee Membership:

Glen P. Perram, Ph.D.
Chairman

William F. Bailey, Ph.D.
Member

Robert B. Greendyke, Ph.D.
Member

ADEDEJI B. BADIRU, Ph.D.
Dean, Graduate School of Engineering
and Management

Abstract

An experimental study was conducted on continuous wave and pulsed laser interaction with graphite, Al, and Ti. The spectroscopy and plume dynamics from the heating and ablation of these materials was examined to characterize laser weapons effects, develop graphite response for thermal protection systems, and provide optical diagnostics for materials processing. Tactical missions for laser weapons include a wide variety of targets, increasing the demands on the laser lethality community. New approaches to reducing the dimensionality of laser and materials interactions are necessary to increase predictive capability.

Porous graphite samples were irradiated with up to 3.5 kW/cm² and 1 MJ deposited energy from a continuous wave ytterbium 1.07 μm fiber laser. Visible emission spectroscopy reveals C₂ Swan (d³Π_g - a³Π_u) Δv=±2, ±1, and 0 sequences, CN red (A²Π - X²Σ⁺) Δv=-4, -3 sequences, CN violet (B²Σ⁺ - X²Σ⁺) Δv=+1, 0 sequences and Li, Na, and K ²P_{3/2,1/2} - ²S_{1/2} doublets. Surface temperatures increased from ~2,500 K at 0.7 kW/cm² to ~4,000 K at 3.5 kW/cm². Spectral emissivity at 3.9 μm ranging from 0.74-0.93 increases by ~8% after laser irradiation. Spectral simulations demonstrate that the ratio of C₂(d) and CN(A) column densities are independent of sample porosity. Column densities increase from 0.00093 to 1.6x10¹² molecules/cm² for CN(A) and 0.00014 to 1.4x10⁹ molecules/cm² for C₂(d) as laser intensities increases from 1.4 to 3.5 kW/cm². Surface temperatures increase by 134 K and CN(A) and C₂ (d) emission increase by 100% and 4,200%, respectively, in stagnation air flow of 5 m/s.

Emissive plumes from pulsed laser ablation of bulk Ti and Al from KrF laser irradiation at laser fluence up to 3.5 J/cm^2 and argon background pressures of 0-1 Torr have been observed using gated ICCD imagery. Mass loss for Ti increases from $0.1 - 0.8 \text{ } \mu\text{g/pulse}$ as pulse energy increase from $174 - 282 \text{ mJ/pulse}$ ($35 - 170 \text{ photons/atom}$) and decreases by $\sim 30 \%$ as pressure increases from vacuum to 1 Torr. Early plume energies are described by free expansion velocities of 1.57 ± 0.02 and of $1.81 \pm 0.07 \text{ cm}/\mu\text{s}$ for Ti and Al, respectively and up to 90% of the incoming laser energy can be attributed to the Al shock front in the mid-field. The ablation thresholds of $90 \pm 27 \text{ mJ}$ ($1.12 \pm 0.34 \text{ J/cm}^2$) for Ti and $126 \pm 13 \text{ mJ}$ ($1.58 \pm 0.16 \text{ J/cm}^2$) for Al also represent 30–70 % of the incident laser energy. The decrease in mass loss at higher pressures is attributed to plasma shielding of the target surface.

Emissive plumes resulting from pulsed ablation of titanium targets have been observed using a gated ICCD camera to characterize the evolution of velocity distributions as the plume expands into vacuum, Ar and He backgrounds. Shifted Maxwell Boltzmann distributions with flow speeds of $u > 0.1 \text{ cm}/\mu\text{s}$ are adequate only for neutral Ti expansion into vacuum. Ionized Ti velocity distribution shows deviation from a conventional shifted Maxwell-Boltzmann distribution. Near the target, the time of flight data clearly indicates several distinct distributions for the neutral Ti, with faster component consistent with the ionized Ti velocity distribution. Expansion into He and Ar are clearly non-Maxwellian, with the highest velocity groups suffering collisions in the shock front. Leading edge velocities decrease more rapidly for Ar, consistent with momentum conservation. Expansion into He maintains the appearance of the vacuum distribution at low velocities

but shows a decrease in the leading-edge velocity and an enhancement of the intensity of the highest-velocity groups at farther target distances. Determination of velocity distributions from time of flight data is complicated by translation-to-electronic excitation rates, intraplume collisional dynamics, and non-hydrodynamic conditions.

Acknowledgments

My sincerest gratitude goes to my wife as I could not have worked the long nights to complete the enclosed research without her support. I would also like to thank my son for all of the moments he made me stop, smile, and realize that my most important jobs in life are being his father and a good husband to my wife.

I would like to express my gratitude to my advisor, Dr. Perram. Our many long conversations about the enclosed work were paramount to my success. However, I value more our conversations on life, and I appreciate him serving as a good mentor, role-model, and friend.

I am grateful to my committee members, Dr. Bailey and Dr. Greendyke, for their assistance in guiding me in my research and providing thought-provoking comments. I am also grateful to the members of Dr. Perram's research group for listening to all of my wild theories on the enclosed work and critically pointing out when they were too crazy to be real!

I would like to thank Dr. Tim Haugan and his research group for graciously allowing me to use their lab space and providing equipment and consumables to accomplish my work.

I would like to thank Mr. Greg Smith, Mr. Mike Ranft, Mr. John Murphy, and Dr. Dan Felker for all of their support and ideas in the lab that were paramount to ensuring that I accomplished the enclosed experiments successfully.

Finally, I would like to thank my sponsor the HEL-JTO for the financial support to accomplish this work.

William A. Bauer

Table of Contents

	Page
Abstract.....	iv
Acknowledgments.....	vii
Table of Contents.....	viii
List of Figures.....	xi
List of Tables.....	xvii
I. Introduction.....	1
II. Background.....	5
2.1 Laser Material (Solid) Interactions.....	5
2.2 Laser Plume Interactions (Pulsed).....	8
2.3 Pulsed laser ablation plume expansion.....	10
2.4 C ₂ and CN Spectroscopy.....	11
2.5 Laser Heating of Graphite.....	16
III. Visible emission from C ₂ and CN during cw laser-irradiated graphite.....	18
3.1 Introduction.....	18
3.2 Experiment.....	22
3.3 Results and discussion.....	25
3.3.1 Plume Visible Spectra.....	25
3.3.2 Surface Temperatures.....	31
3.3.3 Plume Temperatures.....	36
3.3.4 Column Density.....	37

3.3.5 Buoyant Versus Stagnant Flow.....	40
3.4 Conclusion	41
IV. Comparison of plume dynamics for laser ablated metals: Al and Ti	43
4.1 Introduction.....	43
4.2 Experiment.....	45
4.3 Results and discussion	50
4.3.1 Mass Loss	50
4.3.2 Plume Imagery.....	54
4.3.3 Dependence of plume dynamics on pressure and laser energy.....	61
4.4 Conclusion	74
V. Laser ablated Ti velocity distribution dynamics	75
5.1 Introduction.....	75
5.2 Experiment.....	77
5.3 Results and Discussion.....	79
5.3.1 Velocity Distributions from Emission Images.....	79
5.3.2. Velocity Distribution in Vacuum.....	82
5.3.3. Pressure Dependent Velocity Distribution	91
5.4 Conclusion	101
VII. Conclusions	102
6.1 Visible emission from C ₂ and CN during cw laser-irradiated graphite.....	102
6.2 Comparison of plume dynamics for laser ablated metals: Al and Ti.....	103
6.3 Laser ablated Ti velocity distribution dynamics	104
6.4 Recommendations for Future Work.....	105
Appendix A. Molecular Spectroscopy Constants	109

Bibliography 111

List of Figures

Figure		Page
1.	(a) C ₂ Swan band potential energy curves (recreated from [80]) and (b) CN potential energy curves (recreated from [86]).....	13
2.	(a) C ₂ Swan $\Delta v=0$ simulation and (b) CN red $\Delta v=-3$ simulation for $T_r=4800$, $T_v=4,800$, and $\Delta\lambda=0.75$ nm.	16
3.	Experiment Apparatus.....	23
4.	Typical spectrum observed for 1.9 kW/cm ² irradiation of coarse graphite.	26
5.	Typical fit of C ₂ d ³ Π _g -a ³ Π _u $\Delta v=0$ sequence for: (top) 3.5 kW/cm ² and medium porosity with rotational temperature $T_r=4885 \pm 320$ K, vibrational temperature $T_v=4787 \pm 852$ K, and column density $n'l = 8.1 \pm 0.8 \times 10^8$ molecules/cm ² , (middle) 3 kW/cm ² and medium porosity with $T_r=4679 \pm 372$ K, $T_v=3811 \pm 742$ K, and $n'l = 5.8 \pm 0.6 \times 10^8$ molecules/cm ² , and (bottom) 1.4 kW/cm ² and coarse porosity with $T_r=3568 \pm 161$ K, $T_v=3276 \pm 345$ K, and $n'l = 4.9 \pm 0.2 \times 10^6$ molecules/cm ² . The intensity for the bottom spectrum is scaled by a factor of 30, reflecting the low column density.	28
6.	Typical fit of CN A ² Π-X ² Σ ⁺ $\Delta v=-3$ sequence for: (top) 3.5 kW/cm ² and medium porosity with $T_r=4300 \pm 295$ K, $T_v=3989 \pm 170$ K, and $n'l = 1.2 \pm 0.1 \times 10^{12}$ molecules/cm ² , (middle) 3kW/cm ² and medium porosity with $T_r=4150 \pm 249$ K, $T_v=3799 \pm 142$ K, and $n'l = 1.1 \pm 0.09 \times 10^{12}$ molecules/cm ² , and (bottom) 1.4 kW/cm ² and coarse porosity with $T_r=3217 \pm 92$ K, $T_v=3661 \pm 73$ K, and $n'l = 2.7 \pm 0.1 \times 10^{10}$ molecules/cm ² . The intensity for the bottom spectrum is scaled by a factor of 30, reflecting the low column density.	29

7. Resolidification of ejected material from a medium porosity sample irradiated at 3 kW/cm ² after (a) 9 s, (b) 10 s, and (c) 40 s.	31
8. Evolving ratio for C ₂ Swan and CN red column densities at (○) 1.4 kW/cm ² , (□) 1.9 kW/cm ² , (x) 3 kW/cm ² and (Δ) 3.5 kW/cm ² for medium porosity graphite. The corresponding temporally evolving surface temperature (T _s) is shown in the bottom plot.....	33
9. (a) Dependence of surface temperature on laser irradiance for: (○) medium, (◇) coarse, (x) fine, and (Δ) isomolded graphite and (b) Dependence of column density on laser irradiance for (●) C ₂ Swan and (▲) CN red. The C ₂ Swan densities are increased by a factor of 10 ³ to share a common axis.	35
10. Surface temperatures, T _s and plume temperatures: (○) T _r from CN red, (□) T _r from C ₂ Swan, (▲) T _v from CN red, for all graphite porosities and laser irradiances. Prior results for T _r from C ₂ Swan bands reported in [22] (★). A reference line for equal surface and plume temperatures is also provided (--).	36
11. (a) [C ₂ (d)]/[CN(A)] density ratio vs surface temperature and (b) [C ₂]/[CN] density ratio vs plume temperature compared with (–) analysis from NASA's Chemical Equilibrium Analysis (CEA) code. The C ₂ and CN densities were calculated with an electronic temperature equal to the CN(A) rotational temperature and the error bounds for [C ₂]/[CN] values in (b) were on average 13%.....	38
12. Experiment apparatus in (a) x-y plane (b) and x-z plane (dimensions specific to 50 mm lens imaging system) and (c) laser pulse shape for (.) 282 mJ/pulse, (--) 240 mJ/pulse, and (-) 174 mJ/pulse.....	46

13. (a) Laser spot at target from thermal paper burn pattern, (b) optical microscope image of Ti damage, and (c) Ti 224 mJ/pulse ablation plume in 500 mTorr Ar at 141 ns delay. 47
14. (a) Dependence of mass loss on laser energy (●) Ti vacuum, (★) Ti 50 mTorr, (▶) Ti 500 mTorr, (■) Ti 1000 mTorr, (○) Al vacuum, (☆) Al 50 mTorr, (▷) Al 500 mTorr, (□) Al 1000 mTorr, and (b) dependence of mass loss on background pressure (▲) Ti 174 mJ/pulse, (●) Ti 224 mJ/pulse, (△) Al 174 mJ/pulse, (○) Al 224 mJ/pulse, and (□) Al 282 mJ/pulse..... 51
15. Intensity contour images of Ti ablation at 224 mJ 1000 mTorr Ar at (a) 97 ns, (b) 295 ns, (c) 684 ns, (d) 1.13 μ s, (e) 2.8 μ s, and (f) 9.85 μ s delay times. 55
16. Intensity contours of 224 mJ Al ablation in 500 mTorr Ar at 6.1 μ s delay showing vortices as plume slows..... 56
17. Centerline intensity for 224 mJ 1000 mTorr Ti ablation at (a) 145 ns, (b) 350 ns, and (c) 940 ns and for 224 mJ 1000 mTorr Al ablation at delays of (d) 135 ns, (e) 160 ns, and (f) 390 ns. Solid lines represent broadband signals, dashed lines represent the excited neutral species (Ti I or Al I), and dotted lines represent the excited ionized species (Ti II or Al II). 58
18. Filtered imaging intensity dependence on time for Ti II in (●) vacuum, (▲) 500 mTorr, and (■) 1000 mTorr and for Al II in (○) vacuum and (□) 1000 mTorr..... 59
19. Ti ablation intensity contour images and intensity along the centerline of the plume at 240 mJ/pulse laser energy and Ar pressures of (a-b) vacuum, (c-d) 50 mTorr, (e-f) 500 mTorr, and (g-h) 1 Torr at 1.2 μ s delay. Contact front thickness (δ) is defined as the

distance between the 25% and 75% of maximum intensity (I_{\max}) at the plume leading edge.	60
20. Ti ablation intensity contour images and intensity along the centerline of the plume at 500 mTorr Ar at (a-b) 174 mJ/pulse, (c-d) 224 mJ/pulse, and (e-f) 282 mJ/pulse at 2.8 μ s delay.	61
21. Ti (filled markers) and Al (unfilled markers) plume trajectories reflecting the 240 mJ laser pulse temporal distribution (-) at (●) vacuum, (■) 50 mTorr, (★) 250 mTorr, (▲) 500 mTorr, and (◀) 1000 mTorr Ar.....	63
22. (a)Trajectory of Al plume from 240 mJ/pulse ablation in 500 mTorr Ar. Region I is the trajectory in which free expansion occurs and the shock wave is forming. Region II is the trajectory in which the shock wave is fully formed and Sedov-Taylor theory is applicable. Region III is the trajectory in which the contact front slows and the shock wave moves ahead of the contact front, (b) Ti blast model (--) and drag model (-) fits to broadband signal as a function of background pressure at (●) vacuum, (□) 50 mTorr, (◆) 250 mTorr, (△) 500 mTorr, and (★) 1000 mTorr and a laser energy of 240 mJ/pulse. A linear, free expansion model (-) fit to the vacuum data is provided for reference and residuals for the 1000 mTorr Sedov-Taylor and drag model fits are provided in the bottom window, and (c) dependence of plume trajectory on laser pulse energy for (■) Al 174 mJ/pulse, (★) Al 282 mJ/pulse, (□) Ti 174 mJ/pulse, and (★) Ti 282 mJ/pulse at a background pressure of 500 mTorr.....	65
23. Dependence of stopping distance, z_f , for (●) Ti and (■) Al and dependence of initial velocity, $v_{o,D}$, for (○) Ti and (□) Al on (a) background pressure, P_b , at 240 mJ/pulse and (b) laser energy, Q_t , at 500 mTorr.	67

24. Dependence of plume dimensionality, n , for (●) Ti and (■) Al and dependence of plume front energy, E_{ST} , for (○) Ti and (□) Al on (a) background pressure, P_b , at 240 mJ/pulse and (b) laser energy, Q_l , at 500 mTorr. E_{ST} was determined using $n=3$ 70

25. Ti trajectory data for (□) 50 mTorr, (★) 250 mTorr, (△) 500 mTorr, and (★) 1000 mTorr and a laser energy of 240 mJ/pulse scaled using (a) the lower limit of Eq. 24, and (b) using the upper limit of Eq. 24. 71

26. Ti ablation dependence of shock pressure, p_l , for (●) 500 and (■) 1000 mTorr and temperature, T_l , for (○) 500 and (□) 1000 mTorr..... 72

27. (a) 240 mJ Ti ablation into vacuum intensity contours for time delay of 1630 ns where z_d is the “detector” pixel location at 0.49 cm, (b) the corresponding time distribution formed by recording the intensity at a particular z for a series of spectra or times, and (c) the corresponding velocity distribution. 82

28. Broadband Ti velocity distribution from 240 mJ ablation in vacuum at various distances, z , from the target..... 83

29. Velocity distribution of 224 mJ Ti ablation in vacuum at a distance, z , of 0.38 cm from the target (a) showing the (●) broadband signal comprised of the Ti I (--) and Ti II (.) data and (b) the Ti I signal defining the multimode distributions for reference. 84

30. Dependence of Ti I distribution 1 (■) average RMSE x10 and (□) flow speed, u , and Ti II (●) average RMSE x11 and (○) flow speed, u , on SMB exponent n 87

31. 224 mJ Ti ablation in vacuum showing SMB (a) A vs distance, (b) flow speed vs distance, and (c) temperature vs distance for $n=0$ (○) Ti II and (★) Ti distribution 3 and $n=3$ for (■) distribution 1 and (▲) distribution 2. Error bounds are 2σ 88

32. Ti I TOF data and combined SMB distribution fits for distance $z =$ (●) 0.41 cm, (■) 0.61 cm, (★) 0.82 cm, and (▲) 1.02 cm. All three SMB fits utilized $n=3$ and (a) $u=1 \times 10^3$ m/s and (b) $u=0$ m/s. 90

33. Broadband velocity distributions at different z locations from 240 mJ Ti ablation in (a) 1000 mTorr Ar and (b) 1000 mTorr He. 91

34. Broadband Ti velocity distribution leading-edge velocity for (●) 250 mTorr Ar, (■) 500 mTorr Ar, (▲) 1000 mTorr Ar, (○) 250 mTorr He, (□) 500 mTorr He, and (△) 1000 mTorr He. 94

35. SMB fit and residuals to Ti II velocity distribution for 240 mJ in 1000 mTorr Ar at $z=0.89$ cm (fit parameters $T=33821 \pm 7534$ K, $u=7985 \pm 248$ cm/ μ s, $n=0$.) 96

36. Ti plume trajectories for 240 mJ irradiation expansion into (○) vacuum, (★) 250 mTorr, (△) 500 mTorr, and (■) 1000 mTorr He. 98

37. Velocity distribution differences between Ti expansion into (●) vacuum and 250 mTorr (a) (□) He at 0.5 cm and (b) (△) Ar at 0.12 cm. 99

List of Tables

Table	Page
1. Al, Ti, and Graphite thermal property compare at 1 atm pressure [41], [50]	7
2. Comparison of cw graphite irradiation with oxyacetylene torch.	30
3. Average emissivity, ϵ , at $\lambda=3.9 \mu\text{m}$	32
4. Ti and Al Material Properties [41], [47]	48
5. Mass removal parameters.....	53
6. Molecular constants for C ₂ Swan system ($d^3\Pi_g$) (cm^{-1}) [80]	109
7. Vibrational constants for C ₂ Swan system ($d^3\Pi_g$) and CN Red system ($A^2\Pi$) (cm^{-1}) [80], [83]	109
8. Molecular constants for CN Red system ($A^2\Pi$) (cm^{-1}) [83]	110

LASER HEATING OF GRAPHITE AND PULSED LASER ABLATION OF TITANIUM AND ALUMINUM

I. Introduction

Since the first laser system was created in 1960, the US DoD has been interested in high power laser systems for defense related applications [1]. Laser weapon systems such as the USAF Airborne Laser have traditionally been developed for strategic, long-range missions. These missions require atmospheric beam propagation over long distances, something most suitable for a continuous wave laser due to its relatively low irradiance, 1-10 kW/cm² [1], [2]. Recently, interest in tactical mission uses for laser weapons has risen, with systems like the USAF Advanced Tactical Laser (ATL), the US Navy's Laser Weapon System (LAWS), the US Marine Corps Ground Based Air Defense System (GBAD), and the US Army's High-Energy Laser Mobile Systems being developed [3]–[5]. Instead of targeting strategic defense targets such as intercontinental ballistic missiles, tactical laser weapon systems might be utilized to engage closer targets such as a remotely piloted aircraft (RPA) or for force protection missions such as counter-rocket or counter-mortar [3]. Furthermore, pulsed lasers may be employed for counter sensor, lidar, beacon, and illuminator missions [1], [6]–[8].

Materials with high strength to weight ratios such as Al and Ti are traditionally utilized as aircraft components. Understanding laser effects on these metals is of interest for defense related applications [9]. Carbon composite materials offer superior weight advantages, superior formability to complex shapes, and the ability to tailor the stiffness of

the material [10]. With these advantages, the development of carbon composite materials has led to large carbon composite material percentages of military aircraft (~40% of the F-22) [11] and commercial aircraft (~50% of the Boeing 787 Dreamliner) [12]. The current study explores continuous wave (cw) laser irradiated carbon and pulsed ablation of metal targets.

Prior study of laser interaction with carbon composite is rather limited. The complexity of the heating of the many components and layers of carbon composites makes the study of even thermal conduction challenging [13]. Graphite is studied here as a surrogate material for the effects of laser heating on the carbon in carbon composite materials without the added complications of the polymer matrix. Pulsed laser ablation of graphite has been studied extensively for the purposes of making carbon-containing thin films, carbon nanotubes, or basic combustion research [14]–[22]. Comparatively little research on cw irradiation of graphite has been conducted [23], with the majority objectives to find basic thermodynamic properties of carbon such as the sublimation temperature and the triple point.

While pulsed laser systems are not traditionally desirable for long range weapons missions, they may be more suited to tactical missions in certain environments. Pulsed laser systems are utilized in many non-military applications, to include production of thin films [15], material manufacturing [24], and scientific investigation using laser induced breakdown spectroscopy (LIBS) [25]. An extensive body of literature exists on laser heating and ablation of Al to include sources with pulse durations of > 1 ns [26]–[30], laser ablation with Nd:YAG laser systems at $1.06 \mu\text{m}$ [31]–[34], and sources with < 1 ns pulse duration [35], but the study of UV ablation of Al is rather underdeveloped. Comparatively,

less investigation into Ti ablation has been conducted, with studies mainly limited to determining electron density [36], [37], electronic temperatures [38], and TOF distributions [39], [40] in air and vacuum but providing little insight into the evolving plume dynamics at different ambient conditions.

The expansion of laser ablated plumes is a complex process that must account for laser plume interaction, intraplume constituent interactions, plume background interactions, plasma recombination, and excited species radiation [15], [41], [42]. Currently, there is no model that can account for all of the processes that occur from beginning when the initial photon interacts with the surface to the end of the plume expansion resulting in thermalization of the plume constituents. Experimental knowledge of the plume expansion physics will aid in development of models to predict laser-target effects by informing the physics and serving as model verification benchmarks.

Chapter III of this work studies the thermal effects of laser heating of porous graphite with a cw Yb 1.07 μm fiber laser depositing up to 1 MJ of energy on target. Temporally resolved visible emission spectroscopy is used to monitor gas temperatures and column densities of molecular products C_2 and CN and compared to temporally resolved surface temperature measurements under various laser fluence conditions. C_2 and CN spectra are compared for buoyant and stagnation flow conditions. This work was published in *Optical Engineering* in 2016 [43].

Chapter IV of this study characterizes the plume dynamics of Al and Ti from KrF laser (248 nm, 25 ns pulse duration) pulsed laser ablation through analysis of expanding plume shock fronts and plume emissive constituents. This study examines the influence of low pressure (≤ 1 Torr) Ar environment on plume slowing, and compares the

dependence of mass removal on laser fluence and background pressure with the plume energy. Some of the preliminary conclusions from this chapter were published in the *SPIE Conference Proceedings* in 2016 [44] and the whole is being submitted for journal publication.

Chapter V of this work analyzes the velocity distribution dynamics of a common aircraft component metal – Ti – from KrF ablation in various ambient conditions. Plume constituent distributions are traditionally modeled as shifted Maxwell Boltzmann (SMB) distributions. However, empirical application of SMB distribution to data reveals non-physical parameters such as negative flow speeds [45] and spatially defined (transverse and longitudinal) plume temperatures [46]. Time-of-flight data obtained from gated emissions imaging of Ti ablation in vacuum, Ar, and He environment is compared to discuss the appropriateness of the use of a SMB distribution for laser ablated plumes under various conditions. This work is being prepared for journal submission.

This work was accomplished in partial collaboration with the Laser Hardened Materials Evaluation Laboratory (AFRL/RXAP) and the Air Force Research Laboratory (AFRL) Aerospace Systems Directorate (AFRL/RQQM) at Wright-Patterson Air Force Base (WPAFB), OH. The RXAP HEL facility provided and operated the cw laser beam for the laser heating of graphite experiments. The Aerospace Systems Directorate AFRL provided the KrF ablation system to include laser, chamber and pumps, optics, and consumable gases for pulsed experiments on Ti and Al and personnel support for experimental setup.

II. Background

Laser heating and pulsed laser ablation (PLA) of materials is an active area of science that incorporates many disciplines to include statistical mechanics, gas dynamics/kinetics, plasma physics, solid state theory, atomic and molecular spectroscopy, fluid dynamics, and shock theory. This section will attempt to summarize some of the knowledge required to better understand the problem that exists and the solutions proposed in this work. Additional chapter-specific background information is included in Chapters 3, 4, and 5.

2.1 Laser Material (Solid) Interactions

Light absorption in a material is governed by the Beer-Lambert law (assuming monochromatic light, an isotropic medium, and a plane wave)

$$I(z) = (1 - R)I_0 e^{-\alpha z} \quad (1)$$

where I_0 is the laser intensity incident on the target surface, z is the distance into the material traveled by the photon, and R is the reflectivity of the material [41]. The target reflectivity is directly dependent on the incoming laser irradiation wavelength and angle of incidence [47] and a function of material temperature that can change drastically during laser irradiation [48]. The absorption coefficient α is defined by

$$\alpha = \frac{4\pi\kappa_0}{\lambda_0} \quad (2)$$

where, κ_0 is the wavelength dependent material specific attenuation coefficient and λ_0 is the vacuum wavelength [41]. Inversion of the absorption coefficient results in the optical penetration depth,

$$l_{\alpha} = \alpha^{-1} = \frac{\lambda_o}{4\pi\kappa_o}. \quad (3)$$

The optical penetration depth is the depth into a material in which a photon of a particular wavelength will extend before being absorbed [41].

As light is absorbed into a material for \geq ns pulse durations, the absorbed energy is transferred to the phonons of the material, increasing the lattice vibrations resulting in a heating of the material. The heat diffusion length or the characteristic length associated with the transfer of heat to the material is defined by

$$l_T \approx \sqrt{D\tau_l} \quad (4)$$

where D is the material heat diffusivity and τ_l is the laser pulse duration [41]. If the heating of the vibrational lattice becomes large enough to begin to break bonds (i.e., reaches the enthalpy of melting, ΔH_m), the material will reach a transition phase where all of the incoming energy is devoted to converting the solid material into the liquid material. After the material has completely changed to the new liquid phase, it begins to increase in temperature again with the incoming energy. Again, the atoms reach a point where they have so much energy that they break the liquid bonds (the energy has reached the enthalpy of vaporization, ΔH_v , for the material) and the material strongly transitions into a vapor phase. In addition to melting and vaporization, a material may sublime or transition directly from a solid to a vapor without transitioning to the liquid phase. For the materials of interest under the ablation conditions in this study, sublimation due to laser heating is only applicable to graphite while melting and vaporization are the thermal phase changes applicable to Al and Ti.

Al and Ti thermal properties are well known [47], however those of graphite are active areas of research as is reflected by the large error bars in Table 1 [23]. Commercially produced graphite has varying degrees of porosity dependent on the heating and extrusion processes utilized in production. Porous graphite is comprised of binder material, complicating knowledge of “graphite” thermal properties [49].

Table 1. Al, Ti, and Graphite thermal property compare at 1 atm pressure [41], [50]

	Al	Ti	Graphite (single crystal)
Melting Temperature, T_m (K)	933	1,943	--
Vaporization Temperature, T_v (K)	2,792	3,560	--
Sublimation Temperature, T_s (K)	--	--	3957.5 (62.5)

*Error bars are in parenthesis (error bars < 1 K are not displayed)

For high irradiance lasers, laser interaction with the surface can create free electrons either due to photoionization, multi-photon ionization or thermionic emission. The two-photon ionization rate is proportional to the square of the intensity, making higher intensity lasers more effective at multi-photon ionization [51]. According to the Richardson-Dushman equation, the current density emitted from a metal is proportional to the negative of the exponential of the work function divided by the thermal energy [52]

$$j \propto T^2 e^{-\frac{\Phi}{k_B T}} \quad (5)$$

where Φ is the work function of the metal. Therefore, higher temperatures in the metal lead exponentially to an increased thermal emission of electrons.

The laser-material interaction described above is the traditional picture of laser solid interaction via thermal mechanism and is applicable for pulse durations greater than

picoseconds. Evidence exists in the literature of nonequilibrium thermal processes in which much larger ablation yields are achieved than can be explained through simple thermal considerations as discussed above. This phenomena has been called phase explosion and is theorized to occur when the temperature of the material nears the critical temperature, thereby creating a gas-liquid metaphase that is ejected resulting in larger ablation yields [53]. Phase explosion threshold for Ni and Al in air has been measured to be $\sim 5 \text{ J/cm}^2$ [54], [55]. The phase explosion phenomena exists for relatively long pulse durations ($\geq \text{ns}$); below the nanosecond time scales, where l_T becomes smaller than l_α [41], the pulse duration can become shorter than the thermal relaxation time of the material (for metals, this is on the order of 10s of picoseconds [56]), requiring other ablation mechanism explanations such as electronic (coulombic) ablation [15].

2.2 Laser Plume Interactions (Pulsed)

Once the material is vaporized from the surface and while the laser is still on, the vaporized plume can be further excited through interactions of the laser with free and bound electrons [57]. Free electron-free electron interactions known as inverse Bremsstrahlung (IB) are described by the acceleration of free electrons by the incoming laser radiation in the presence of ions or neutrals. These accelerated electrons then collide with atoms either ionizing them and/or exciting them in processes called electron impact ionization. Bound electron-free electron interactions commonly known as photoionization involve direct photon absorption by a neutral (or ion), thereby exciting an electron to potentially above the ionization threshold for the species. In addition to laser-electron interaction, UV laser irradiation of metals has shown a dependence of laser transmission on vaporized plume

cluster characteristics [58], interpreted as condensed cluster laser light interaction theories such as Rayleigh Scatter [58] or Mie Scatter [59].

Laser-plume interaction studies have shown that the IB absorption mechanism typically dominates at IR wavelengths due to the λ^3 dependence of its absorption coefficient but that PI and Mie theory tend to dominate more at UV wavelengths [60], [61]. Additionally, Mie scattering was shown to be a less important (but not-negligible) mechanism than Mie absorption [59]. Increased laser absorption by the plume results in increased plume speeds [60]. Comparatively, laser scattering processes would either more slowly increase the laser energy in the plume or not contribute to the energy of the plume at all (depending on the nature of the scattered light). Both mechanisms would shield the target surface from the incoming laser radiation.

Absorption of the laser energy leads to the formation of a highly ionized plasma through processes like electron-impact ionization or photoionization. Nanosecond pulsed laser ablation of Al, Ti, and graphite in Ar background gas for many different laser wavelengths and conditions have shown the following atomic species to be present in ablation: Al I, Al II, Ti I, Ti II, C I, C II, Ar I, and Ar II [17], [62]–[65]. Emission spectroscopy can be used to determine the electron density and excitation temperature of the plume [66], [67]. De Giacomo irradiated Ti with a KrF laser (248 nm) in vacuum and used Ti I and Ti II emissions to determine an electron density $n_e > 9 \times 10^{17} \text{ cm}^{-3}$ in vacuum and Ti temperatures of up to 11,800 K [36]. Nd:YAG ablation of Al with the third harmonic wavelength (355 nm) utilized Al I and Al II emissions to determine $n_e = 2.75 \times 10^{18} \text{ cm}^{-3}$ and Al temperatures of $\sim 8750 \text{ K}$ [63]. Pulsed laser ablation of graphite with an

Nd:YAG laser (1064 nm) in vacuum, He, Ar, and air backgrounds has yielded electron densities of $4 \times 10^{17} \text{ cm}^{-3}$ in vacuum and $1.4 \times 10^{17} \text{ cm}^{-3}$ for other background gases and electron temperatures of $\sim 41,000 \text{ K}$ in vacuum, $\sim 27,000 \text{ K}$ in 2.25 mTorr of He, $30,000 \text{ K}$ in 2.25 mTorr of Ar, and $26,000 \text{ K}$ in 0.75 mTorr of air [17], [64]. After the laser is turned off, ionization may still occur due to electron impact ionization, but photoionization will not occur [68].

As is noted in the title, this section is mostly applicable to pulsed lasers and not continuous wave (cw) lasers due to the high irradiances achieved by pulsed lasers that can create free electrons ($>100 \text{ kW/cm}^2$) [69]. In this work the maximum cw irradiance achieved is 3.5 kW/cm^2 , orders of magnitude below what is theoretically necessary to create a plasma.

2.3 Pulsed laser ablation plume expansion

After the initial laser ablation and laser interaction with the ablated material in the plume, the laser turns off and the plume expands into the ambient environment. Fast emissions imaging and TOF measurements have shown plume expansion speeds of on order $1 \text{ cm}/\mu\text{s}$ for vacuum conditions [15]. Comparatively, Phelps et al showed $\text{YBa}_2\text{Cu}_3\text{O}_{7-x}$ plume expansion into various O_2 background pressures is slowed dramatically due to collisions with the background gas, showing decreasing plume speeds recorded for corresponding increasing background pressure resulting in stopping distances ranging from $\sim 86 \text{ mm}$ in 50 mTorr O_2 to $\sim 55 \text{ mm}$ in 1 Torr O_2 [70]. Collisions between the expanding plume and background gas cause excitation and emission radiation for both the vapor species and the background gas along the contact front [71]. Intraplume

collisions between the plume constituents can also lead to enhanced excitation within the plume. The kinetic energy of the plume at the contact front has been recorded up to 50 eV/atom, easily sufficient to ionize and excite the plume constituents and/or the background gas [45]. The ionization potentials for Al, Ti, Ar, and He are 6.0, 6.8, 15.8, and 24.6 eV, respectively [72].

Laser induced plume velocity distributions have been described by Maxwell-Boltzmann distributions superimposed on flow speeds u according to

$$f(v) = Av^3 e^{-\frac{m(v-u)^2}{2kT}} \quad (6)$$

where T is a temperature parameter describing the range of velocities and A is a collection of constants [15], [45]. Various theories have been developed to describe the form of the distribution. Zheng et al theorized that laser induced plumes could be described by the theory of isentropic supersonic expansion (which leads to emitted particles with velocities of the form of Eq. 6 [73], [74]) and successfully applied this theory to describing the plume expansion of superconductors [75], [76]. Others have theorized that the initial vapor plume distributions are altered due to the presence of a Knudsen layer - a solid vapor interface only a few mean free paths wide in which intraplume collisions convert the initial vapor distribution to a shifted Maxwell Boltzmann distribution of the form of Eq. 6 [77], [78].

2.4 C₂ and CN Spectroscopy

The oxidation of graphite is rapid beginning at surface temperature of $\sim 1800\text{K}$, and has recently been studied under cw fiber laser irradiation at $1\text{-}4\text{ kW/cm}^2$ [49], [79]. When heated to high temperatures, graphite creates molecular species C₂ and CN (CN is only

produced if in nitrogen environment while C₂ is readily produced in numerous ambient environments) [14]-[18]. C₂ has many transitions that populate the electromagnetic spectrum in the ultraviolet (UV), visible (VIS) and near infrared (NIR); however, the only transitions that are generally observed in PLA of graphite are those of the Swan bands. These bands have an upper electronic state, d³Π_g, that is 19,306 cm⁻¹ above the lower electronic a³Π_u energy level [80]–[82]. CN also produces many transitions in the UV-VIS-NIR. The strongest of these are: CN violet (B²Σ⁺-X²Σ⁺), with the upper electronic energy level 25,753 cm⁻¹ above the X²Σ⁺ ground state and CN red (A²Π-X²Σ⁺) with the upper electronic state 9243 cm⁻¹ above the ground state [83]–[85]. This work will concentrate primarily on the C₂ and CN red transitions.

The observed visible emissions for C₂ Swan and CN red originate and end on energy levels that are comprised of rotational energy, vibrational energy, and electronic energy according to

$$E = T_k + G(v) + F(J) \quad (7)$$

where T_k is the electronic energy, $G(v)$ is the vibrational energy, and $F(J)$ is the rotational energy. The electronic energy is a value that describes the lowest level of that particular electronic state. The vibrational energy is dependent on a particular vibrational level, v according to

$$G(v) = \omega_e \left(v + \frac{1}{2} \right) - \omega_e \chi_e \left(v + \frac{1}{2} \right)^2 + \omega_e \gamma_e \left(v + \frac{1}{2} \right)^3 \quad (8)$$

where ω_e , $\omega_e \chi_e$, and $\omega_e \gamma_e$ are constants specific to a particular molecule and electronic state [81]. The rotational energy for states that contain electronic angular momentum

(applicable to C_2 and CN) is complex and the next few sections will detail calculation of the rotational energy levels.

Figure 1 shows the potential energy surfaces for C_2 Swan and CN red. Vibrational levels for the $C_2(d)$ (upper) state have been identified for $v=0-10$ and CN(A) vibrational levels for $v=0-22$ [80], [83]. Consideration of various coupling schemes between the electronic and nuclear angular momentum results in nine different rotational transitions for the $^3\Pi-^3\Pi$ energy levels ($Q_1, Q_2, Q_3, R_1, R_2, R_3, P_1, P_2, P_3$) and 12 different rotational transition for the $^2\Pi-^2\Sigma$ energy levels ($Q_1, Q_2, R_1, R_2, P_1, P_2, {}^RQ_{21}, {}^PQ_{12}, {}^QP_{21}, {}^QR_{12}, {}^OP_{12}, {}^SR_{21}$) [81].

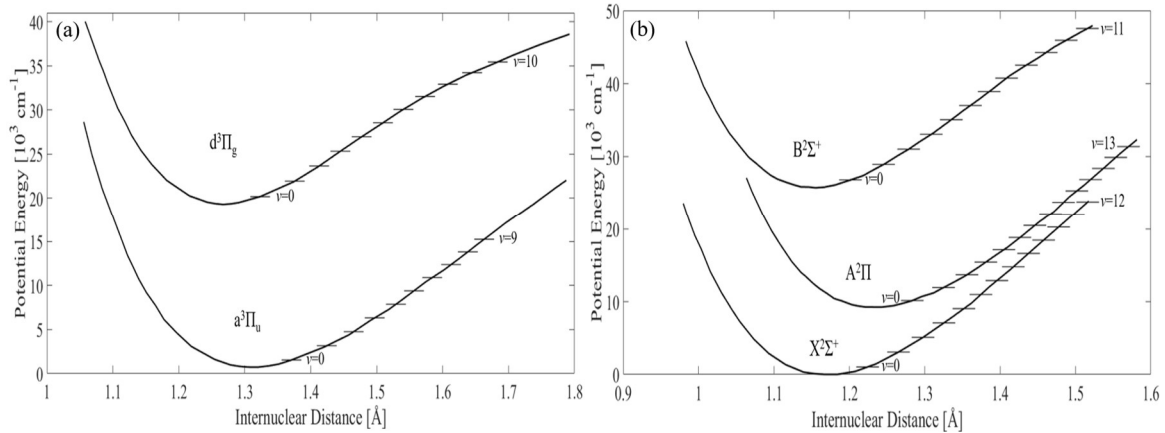


Figure 1. (a) C_2 Swan band potential energy curves (recreated from [80]) and (b) CN potential energy curves (recreated from [86]).

Common spectroscopic notation F_x describes energy levels based on the total angular momentum, J , and an angular momentum, N , that accounts for coupling between the nuclear angular momentum and the orbital angular momentum [86], [81]. For the C_2 Swan $^3\Pi$ states, F_1, F_2 , and F_3 represent levels with $J=N+1, J=N$, and $J=N-1$, respectively. The rotational energy levels for C_2 $^3\Pi$ can be calculated according to [81]

$$F_1(J) = B_v[J(J+1) - \sqrt{Z_1} - 2Z_2] - D_v\left(J - \frac{1}{2}\right)^4 \quad (9)$$

$$F_2(J) = B_v[J(J+1) + 4Z_2] - D_v\left(J + \frac{1}{2}\right)^4 \quad (10)$$

$$F_3(J) = B_v[J(J+1) + \sqrt{Z_1} - 2Z_2] - D_v\left(J + \frac{3}{2}\right)^4 \quad (11)$$

$$Z_1 = A^2Y(Y-4) + \frac{4}{3} + 4J(J+1) \quad (12)$$

$$Z_2 = \frac{1}{3Z_1}[A^2Y(Y-1) - \frac{4}{9} - 2J(J+1)] \quad (13)$$

$$Y = \frac{A}{B_v} \quad (14)$$

where A is the spin-orbit coupling constant, and B_v and D_v are first and second order centrifugal motion correction constants. Similarly to above, the rotational levels F_1 and F_2 for the CN $^2\Pi$ and $^2\Sigma$ states represent levels with $J=N+1/2$ and $J=N-1/2$, respectively, and can be calculated according to [81]

$$F_1(J) = B_vN(N+1) - D_vN^2(N+1)^2 + H_vN^3(N+1)^3 + \frac{1}{2}\gamma N \quad (15)$$

$$F_2(J) = B_vN(N+1) - D_vN^2(N+1)^2 + H_vN^3(N+1)^3 - \frac{1}{2}\gamma(N+1) \quad (16)$$

where H_v is the third order centrifugal motion correction constants and γ is the spin rotation angular momentum coupling constant. The spectroscopy of the C₂ Swan bands and CN red bands has been covered extensively and the corresponding spectroscopic constants

have been published in the literature (see Appendix A. Molecular Spectroscopy Constants) [80], [83], [84], [87].

Spectral simulations can be accomplished using the energy level equations above with appropriate spectroscopic constants and the following equation

$$I_{\lambda} = \frac{hcA_{ij}n_i l}{\lambda_{ij}^3} = n_i l = \frac{hcA_{ij}n' l}{\lambda_{ij}^3} \frac{(2J' + 1) e^{-\frac{F(J')}{k_b T_r}} e^{-\frac{G(v')}{k_b T_v}}}{\sum_{v'} \sum_{J'} (2J' + 1) e^{-\frac{F(J')}{k_b T_r}} e^{-\frac{G(v')}{k_b T_v}}} \quad (17)$$

where A_{ij} is the Einstein A coefficient (s^{-1}), n_i is the concentration of the species of interest in the upper state i , l is the optical path length (cm), λ_{ij} is the wavelength of a species transition from upper state i to lower state j , T_v is the vibrational temperature (K), and T_r the rotational temperature (K). Eq. 17 assumes an optically thin plume [86].

Figure 2 shows a simulation of the C_2 Swan $\Delta v=0$ sequence and the CN red $\Delta v=-3$ sequence. The line shapes are assumed to be Gaussian and a spectral resolution of $\Delta\lambda=0.75$ nm has been selected. The selected resolution here is too large to resolve the individual C_2 Swan band rotational transitions but the vibrational sequence heads at 516.5 nm ($v'=0$ to $v''=0$), 512.9 nm ($v'=1$ to $v''=1$), 509.8 nm ($v'=2$ to $v''=2$), and 507.1 nm ($v'=3$ to $v''=3$) are readily observed. More transitions are observed for CN red; the sequence heads can be found at 691.4 nm ($v'=3$ to $v''=0$), 707.6 nm ($v'=4$ to $v''=1$), 724.7 nm ($v'=5$ to $v''=2$), 742.4 nm ($v'=6$ to $v''=3$) and 761.1 nm ($v'=7$ to $v''=4$). Gas parameters of $T_r=4,800$ K and $T_v = 4,800$ K were selected arbitrarily for the displayed fits. Changes in T_v significantly affect the relative amplitudes of the observed vibrational sequence heads while changes in T_r would significantly affect the intensity location in between the sequence heads.

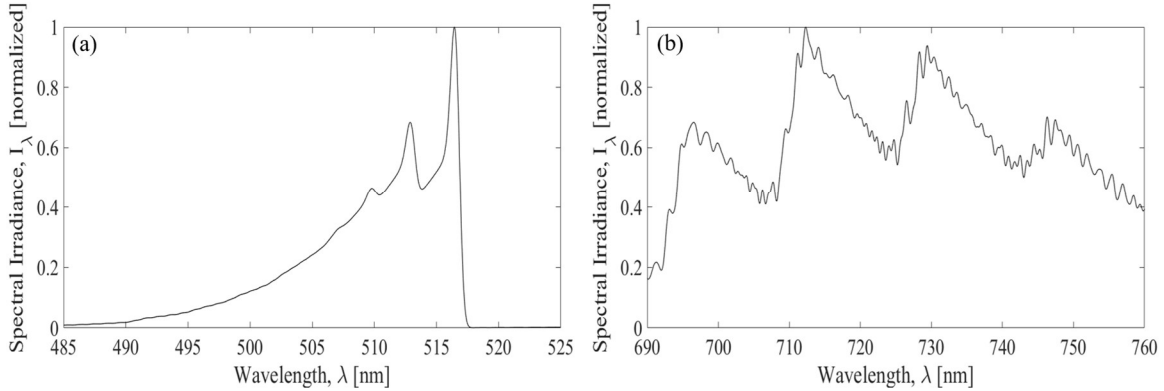


Figure 2. (a) C₂ Swan $\Delta v=0$ simulation and (b) CN red $\Delta v=-3$ simulation for $T_r=4800$, $T_v=4800$, and $\Delta\lambda=0.75$ nm.

2.5 Laser Heating of Graphite

Extensive research has been conducted on pulsed laser ablation of graphite for purposes of making carbon-containing thin films, carbon nanotubes, and basic research. [14]–[22], [88]. In these experiments, high gas temperatures (20,000K) and dense plasmas form (1×10^{17} cm⁻³ electron density) resulting in fast shock fronts [17], [18], [88]. Emissions from neutral and singly ionize C, C₂ Swan bands, and CN violet are observed [19]. The triple point of graphite has been investigated under pulsed laser conditions and was found to range from 4050-4950 K at 110 to 2500 atm [23], [89], [90].

Comparatively little research has been accomplished for cw laser heating of graphite [23]. Typical dwell times of 1-100 s results in more energy transferred to the target relative to pulsed irradiation of graphite but significantly lower irradiance does not result in a plasma. The graphite sublimation temperature and triple point have been studied utilizing cw laser heating at pressures ranging up to 1000 atm resulting in recorded surface temperatures from 3130 to 6940 K [91]–[94]. The triple point of graphite was determined to be 4130 ± 30 K at 120 ± 10 atm [92].

Spectral emissions from laser heating of graphite reveal details about the chemical kinetics occurring at the surface. Acosta et al analyzed combustion from graphite laser irradiation and determined that column densities for CO and CO₂ are on the order of 10¹⁷ molecules/cm₂ for 777 W/cm² irradiation and that the density ratios show discrepancies from expected equilibrium ratios [79]. Limited analysis of C₂ and CN spectral emissions from cw laser graphite heating products have been conducted [91], [95]. Analysis of C₂ and CN emissions is complimentary to that of the combustion emissions. Furthermore, the coupling of time-resolved C₂ and CN emissions data with time-resolved surface temperatures could lead to refined thermodynamic constants.

III. Visible emission from C₂ and CN during cw laser-irradiated graphite

Porous graphite samples were irradiated with up to 3.5 kW/cm² and 1 MJ deposited energy from a continuous wave (cw) ytterbium 1.07 μm fiber laser. Visible emission spectroscopy reveals C₂ Swan (d³Π_g - a³Π_u) Δv=±2, ±1, and 0 sequences, CN red (A²Π - X²Σ⁺) Δv=-4, -3 sequences, CN violet (B²Σ⁺ - X²Σ⁺) Δv=+1, 0 sequences and Li, Na, and K ²P_{3/2,1/2} - ²S_{1/2} doublets. Surface temperatures increased from ~2,500 K at 0.7 kW/cm² to ~4,000 K at 3.5 kW/cm². Spectral emissivity at 3.9 μm ranging from 0.74-0.93 increases by ~8% after laser irradiation. Spectral simulations demonstrate that the ratio of C₂(d) and CN(A) column densities are independent of sample porosity. Column densities increase from 0.00093 to 1.6x10¹² molecules/cm² for CN(A) and 0.00014 to 1.4x10⁹ molecules/cm² for C₂(d) as laser intensities increases from 1.4 to 3.5 kW/cm². Surface temperatures increase by 134 K and CN(A) and C₂(d) emission increase by 100% and 4,200%, respectively, in stagnation air flow of 5 m/s.

3.1 Introduction

The effects of high power, cw laser irradiation on carbon composite materials is critical to the performance of emerging laser weapon systems, particularly for tactical missions [1], [96]. Oxidation and sublimation of graphite surfaces are a key step in characterizing the degradation of carbon fibers. Mass loss, combustion, thermal response, and material properties of laser irradiated graphite have been investigated as part of a larger study of laser effects on carbon fiber reinforced polymers [49], [79]. In this study, the visible spectra from these plumes are examined.

A significant study has been conducted regarding the pulsed laser ablation of graphite for the purposes of making carbon nanotubes, carbon-containing thin films, or basic combustion research of carbon [14]–[22], [88]. In these experiments, very high gas temperatures are achieved (20,000 K) and dense plasmas are formed (electron density of $1 \times 10^{17} \text{ cm}^{-3}$ and electron temperature of 30,000 K) in fast shock fronts [17], [18], [88]. Excited species observed spectroscopically include neutral and singly ionized C, C₂ Swan bands ($d^3\Pi_g - a^3\Pi_u$) and CN violet ($B^2\Sigma^+ - X^2\Sigma^+$) when N₂ gas is present. Most spectroscopic data show a maximum in C₂ intensity very close to the surface and then a quick decrease in C₂ Swan bands intensity away from the laser-irradiated surface [19]. Under the same conditions (10 J/cm², 30 ns XeCl irradiation of graphite at 100 Pa), the intensity of CN violet emission increases from the surface to a distance of ~6 mm before rapidly decreasing [19]. Many mechanisms of formation have been described in the literature for both C₂ and CN to include formation of C₂ by dissociation of ejected large C_n clusters and atomic neutral and ionic C recombination, [18], [20]–[22], [97] and formation of CN through both atomic and molecular nitrogen reactions with atomic or diatomic carbon, [18], [21], [22], [88], [97], [98] or through direct surface nitridation reaction [21]. The reaction pathways appear to be dependent on laser fluence, with relatively higher laser fluence favoring C₂ production via recombination over dissociation [20] and relatively higher fluence favoring CN production via atomic carbon reaction versus C₂ gas-phase reaction [21]. All of the studies mentioned earlier were conducted in the absence of oxygen, thereby ignoring combustion reactions. Finally, the triple point of graphite has been investigated under pulsed laser conditions and has been found to range from 4050 to 4950 K at pressure of ~110 to 2500 atm [23], [89], [90].

Compared to pulsed laser ablation of graphite, little research has been conducted with cw irradiation of graphite [23]. The cw laser irradiance is significantly lower (kW/cm^2) and no plasma is formed. However, the amount of energy transferred to the target material is higher with typical dwell times of 1 to 100 s. The sublimation temperature and triple point of graphite were studied by cw laser irradiation at pressures from 0.003 to 1000 atm, laser intensities of 10 to 50 kW/cm^2 , and dwell times of ~ 2 to 5 s, revealing surface temperatures ranging from 3130 to 6940 K [91]–[94]. Whittaker et al. irradiated various porosity graphite samples with a CO_2 laser at 50 kW/cm^2 and 0.003 to 1 atm of either Ar or Ar + O_2 mixture; analysis of optical pyrometry surface temperature measurements led to a conclusion that the triple point of graphite is ~ 3800 K at ~ 0.2 atm, which does not seem to be consistent with other findings [23], [91]–[94]. Visible emission spectroscopy of the C_2 Swan bands revealed gas temperatures from 3050 to 4120 K [91]. Gokcen et al. heated graphite utilizing an HF laser at ~ 50 kW/cm^2 in 120 to 215 atm of various background gases (Ar, Ne, and/or Kr) [92]. Optical pyrometry with constant emissivity provided surface temperatures while monitoring the vessel pressure. Post-test, microscopy was used to determine the presence of liquid graphite. The triple point of graphite was determined at 4130 ± 30 K and 120 ± 10 atm [92]. No visible emissions spectroscopy was performed in this study. Kirillin et al. performed more recent experiments, irradiating graphite with an Nd:YAG laser in Ar, Ne, and He at pressures up to 1000 atm [93], [94]. Visible emission spectroscopy confirmed the presence of C_2 but no further analysis was completed. Optical pyrometry predicts the triple point to be 5000 ± 200 K at 100 atm when undergoing cw irradiation [93], [94]. Gosse et al. irradiated graphite using a fiber laser at irradiances of 1 to 4 kW/cm^2 under a 204 m/s shear flow to

investigate equilibrium and kinetic rates of sublimation of graphite [95]. Surface temperatures of up to ~ 4000 K were observed with optical pyrometry at 1 atm. Visible emission spectroscopy of the plume was performed and CN violet bands were identified. Detailed spectroscopic analysis was hindered due to large black body emissions generated by the surface of the graphite.

The spectroscopy of the major molecular products created during laser irradiation of graphite – C_2 and CN – has been extensively studied in pulsed laser ablation experiments, stellar spectroscopy, and flames from hydrocarbons [80], [14], [18], [81]–[85], [87], [99]–[104]. Extensive line lists with accompanying Einstein-A coefficients are available [80], [83]–[85], [87], [99], [100]. The upper triplet state of the C_2 Swan bands ($d^3\Pi_g$) sits $19,306\text{ cm}^{-1}$ above the lower $a^3\Pi_u$ state with electronic energy $\sim 720\text{ cm}^{-1}$ above the ground state [80]–[82]. The strongest transitions for C_2 Swan bands are the $\Delta v=0$ sequence at 490 to 516.5 nm. CN has two main electronic bands: CN violet ($B^2\Sigma^+-X^2\Sigma^+$) and CN red ($A^2\Pi-X^2\Sigma^+$). The upper state of the CN violet transition, $B^2\Sigma^+$, is $25,753\text{ cm}^{-1}$ above the ground $X^2\Sigma^+$ state, and its strongest transitions are the $\Delta v=0$ bands in the near UV (378 to 390 nm) [83], [85]. The CN red bands have an upper state $9,243\text{ cm}^{-1}$ above CN $X^2\Sigma^+$ and their strongest transition is in the near-infrared (1087 to 1350 nm) [83], [84].

Finally, ablation of graphite and carbon-based materials from shock front turbulence and plasma flow conditions has been investigated for research into hypersonic flight [105], [106]. In studies conducted by Lewis et al., the shock from an 8.6 km/s flight-speed equivalent airflow ablated a preheated graphite sample [105]. Surface temperatures of ~ 2000 K were recorded by optical pyrometry and CN violet spectral radiances of up to

$750 \frac{W}{cm^2 \mu m sr}$ are reported from visible emission spectroscopy. Asma et al. investigated ablation of carbon resin composite and cork utilizing an inductively coupled plasma wind tunnel capable of creating plasma flow with up to 10 MW/m^2 heat fluxes in pure nitrogen and air environments [106]. Surface temperatures of up to $\sim 2700 \text{ K}$ were recorded with optical pyrometry. Visible emission spectroscopy of the ablated plumes identified CN violet, CN red, C₂ Swan, Na, Li, K, O, and N species. No detailed spectroscopic analysis was conducted in either study.

A detailed study of the spectroscopy of cw graphite irradiation products is complimentary to prior spectroscopic studies of hypersonic and pulsed graphite ablation studies. In this study, a detailed visible emission spectroscopic analysis is used to monitor C₂ Swan and CN red column densities and plume temperatures arising from irradiation of different porosities of graphite with a cw Yb 1.07 μm fiber laser with deposited energies as high as 1 MJ. Spatially resolved surface temperatures are monitored using observed emissivity from post-irradiated samples. The spectra for buoyant and stagnation flow conditions are compared. This study is a part of a larger program to determine the chemical kinetics during laser irradiation of graphite at deposited energies as high as 1 MJ.

3.2 Experiment

A schematic of the experimental apparatus is shown in Figure 3. This study is part of a larger program and further details of experimental setup have been provided previously [49]. Briefly, graphite samples of differing porosity (coarse, medium, fine, and isomolded, purchased at the Graphitestore.com) were irradiated with an IPG Photonics YLS series 10 kW ytterbium 1.07 μm fiber laser with irradiances ranging up to 3.5 kW/cm^2 for typical

durations of 120 s. The laser beam had a flat-top profile with 86% of the power in a 2.5 cm² spot. Stagnation flow conditions were varied by forcing air on the sample through a nozzle located perpendicular to the laser-irradiated surface. The laser traveled through the center of the hollow nozzle and onto the target. However, the majority of irradiations was performed under buoyant (no flow) conditions.

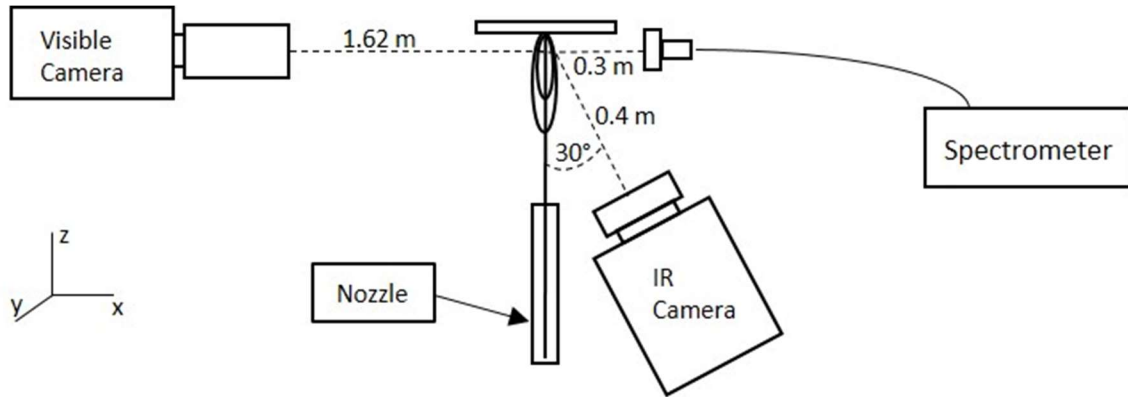


Figure 3. Experiment Apparatus.

Visible emissions were collected at an angle parallel to the graphite sample surface using a fiber optic equipped HR4000 Ocean Optics visible spectrometer. The spectrometer had a spectral resolution of 0.75 nm, 18 mm diameter field of view, and frame rate of up to 14 Hz. A collimating lens on the front of the fiber optic was located 0.3 m from the sample and centered on a spot 1.75 cm above the center of the laser spot. A shortpass filter ($\lambda = 400\text{-}775$ nm) was utilized to ensure that scattered laser radiation was not allowed into the detector and various optical density filters were utilized to eliminate detector saturation. Spectral calibrations were conducted daily utilizing an Hg lamp and absolute radiometric calibrations were accomplished posttest using an NIST- certified tungsten filament. At the peak wavelength of detector detectivity ($\lambda = 625.71$ nm), the absolute radiometric

calibration factor for the smallest integration time utilized (1 ms) was 2.153×10^{-4} $\frac{\mu W}{cm^2 nm} / count$.

Fast visible imagery was captured with a Phantom V12 camera with an 800×1280 pixel complementary metal oxide semiconductor focal plane array. The visible camera was positioned at a horizontal distance of 1.62 m from the laser spot center, aligned parallel to the target surface. A lens with a variable focus $f = 50\text{-}150$ mm was utilized to view an area as small as 35×80 mm. Various combinations of neutral density filters, and integration times were utilized to reduce detector saturation. The imagery was recorded at 1300 frames/s with a 208×480 window size.

Surface temperatures were monitored with an FLIR SC6000 InSb mid-infrared ($\lambda = 3\text{-}5 \mu m$) camera positioned 40 cm from the laser irradiation point at an angle 30 deg from the sample surface normal. The 640×512 pixel FPA was equipped with a 25-mm focal length lens yielding spatial a resolution of $513 \times 703 \mu m$ per pixel. A framing rate of up to 350 Hz was achieved by narrowing the field of view to 320×256 pixels. Four integration times ranging from 0.03 to 1.5 ms were utilized to extend the temperature dynamic range. The FLIR was calibrated pretest for absolute irradiance and detector linearity using a blackbody at temperatures of 323 - 873 K and longer integration times. In between laser irradiations, calibration for minor offset/gain corrections was accomplished using a cavity blackbody. A $3.9 \pm 0.1\text{-}\mu m$ filter was placed in front of the camera to limit the wavelength of the incoming emissions and an OD 2.0 neutral density filter was used to limit detector saturation.

Hemispherical reflectance measurements were conducted on a Surface Optics Corp. 100 Hemispherical Directional Reflectometer using a 30-deg angle of reflection and radiation from a 500°C blackbody to determine the emissivity of the irradiated samples, thereby allowing for calculation of the surface temperatures. A polarization filter was inserted into the path of the reflected emissions before entering the spectrometer to create either plane polarized or perpendicular polarized radiation. Un-irradiated samples cut into 1" x 1" x 0.25" squares of each porosity type were analyzed under 30°C, 250°C, and 500°C conditions. Post-experiment irradiated samples were cut to similar specifications from locations slightly below the laser spot to obtain reflectance (emissivity) data from as close to hottest laser spot as possible without having to account for the emissivity of redeposited material above the laser spot. Emissivities are reported as averages of perpendicular and plane polarized emissivity.

3.3 Results and discussion

3.3.1 Plume Visible Spectra.

Figure 4 shows a typical visible emission spectrum. Molecular emission is dominated by the C₂ Swan ($d^3\Pi_g - a^3\Pi_u$) $\Delta v = \pm 2, \pm 1, \text{ and } 0$ sequences, CN red ($A^2\Pi - X^2\Sigma^+$) $\Delta v = -4, -3$ sequences, and the CN violet ($B^2\Sigma^+ - X^2\Sigma^+$) $\Delta v = +1, 0$ sequences. Atomic emissions from Li, Na, and K $^2P_{3/2} - ^2S_{1/2}$ doublets were observed for nearly all samples. The atomic emission is strongly optically trapped, as evidenced by the intensities ratios for the doublet emission.

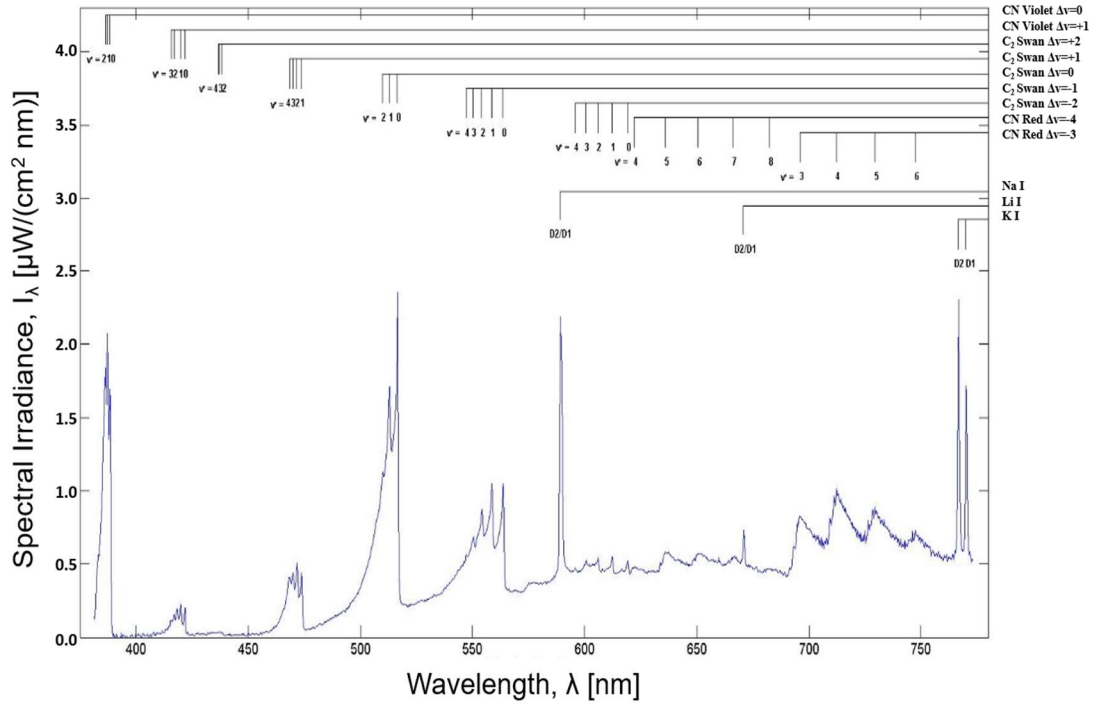


Figure 4. Typical spectrum observed for 1.9 kW/cm² irradiation of coarse graphite.

Spectral simulations of C₂ Swan Δv=0 sequence and the CN red band Δv=-3 sequence were created to extract ro-vibrational plume temperatures and molecular column densities utilizing the optically thin approximation:

$$I_\nu d\nu = h\nu_{ij}A_{ij}n_i l d\nu = I_\lambda d\lambda = \frac{hcA_{ij}n_i l}{\lambda_{ij}^3} d\lambda \quad (18)$$

where A_{ij} is the Einstein A coefficient (s⁻¹), n_i is the concentration of the species of interest in the upper state i , l is the optical path length (cm), and ν_{ij} , λ_{ij} is the frequency or wavelength of a species transition from upper state i to lower state j . In this paper, we focus on the column densities ($n_i l$) and vibrational and rotational temperatures (T_v and T_r ,

respectively) of the excited states. The density in a specific $n_i l$, is related to the total density in the excited electronic state, $n' l$, by the rotational vibrational partition functions

$$n_i l = n' l \frac{(2J' + 1) e^{-\frac{F(J')}{k_b T_r}} e^{-\frac{G(v')}{k_b T_v}}}{\sum_{v'} \sum_{J'} (2J' + 1) e^{-\frac{F(J')}{k_b T_r}} e^{-\frac{G(v')}{k_b T_v}}} \quad (19)$$

where J' is the upper state total angular momentum quantum number, v' is the upper state vibrational quantum number, $G(v')$ is the upper state vibrational energy, $F(J')$ is the upper state rotational energy, l is the plume width. The concentration of all ro-vibrational levels in the upper electronic state, n' , is related to the total species concentration,

$$n' l = n l \frac{(2S + 1)(2 - \delta_{\Lambda,0}) e^{-\frac{T_k}{k_b T_e}}}{\sum_k (2S_k + 1)(2 - \delta_{\Lambda_k,0}) e^{-\frac{T_k}{k_b T_e}}} \quad (20)$$

where S is the state spin quantum number, Λ is the projection of the orbital angular momentum onto the body axis, T_k is the electronic energy of the upper electronic state k , and T_e is the electronic temperature. We also use the notation, $n' = [\text{C}_2(\text{d})]$ or $[\text{CN}(\text{A})]$ to represent the concentrations of the excited electronic states and $n = [\text{C}_2]$ or $[\text{CN}]$ to represent the total concentration of the respective species. Electronic temperatures, T_k , might be estimated from the atomic lines in Figure 4. However, the alkali atomic lines are optically trapped and thus, do not linearly reflect the population ratios.

Rotational energy levels $F(J)$ were calculated in the manner of Herzberg [81] for the C_2 Swan bands and the CN red bands for the intermediate between (a) Hund's case and (b) Hund's case. Spectroscopic constants and Einstein A-coefficients were obtained from

the recent works of Brooke et al [80], [83]. Simulations were benchmarked against the commercial code SPECAIR with residuals of less than 2.7% on average.

Figure 5 and Figure 6 show typical fits for visible emission spectra. The quality of the spectral fits is acceptable, with typical residuals of less than 2.6% on average. Noticeable differences are observed in fitting the C₂ Swan $\nu'=1 \nu''=1$ band, particularly at higher laser irradiance. It is possible that some minor spectral emission is not accounted for near 513 nm. The current spectral resolution is insufficient to further evaluate the spectral residuals. Because of this, the C₂ Swan vibrational temperatures were considered less reliable. The CN violet bands were observed for some conditions. However, detector sensitivity in this region did not permit quantitative analysis of CN violet bands.

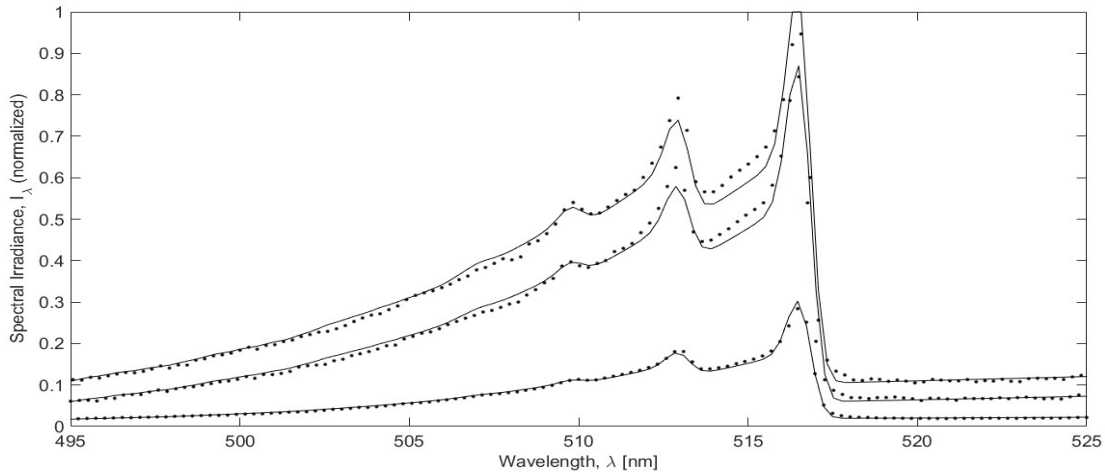


Figure 5. Typical fit of C₂ d³Π_g-a³Π_u Δν=0 sequence for: (top) 3.5 kW/cm² and medium porosity with rotational temperature $T_r=4885 \pm 320$ K, vibrational temperature $T_v = 4787 \pm 852$ K, and column density $n'l = 8.1 \pm 0.8 \times 10^8$ molecules/cm², (middle) 3 kW/cm² and medium porosity with $T_r=4679 \pm 372$ K, $T_v= 3811 \pm 742$ K, and $n'l = 5.8 \pm 0.6 \times 10^8$ molecules/cm², and (bottom) 1.4 kW/cm² and course porosity with $T_r=3568 \pm 161$ K, $T_v=3276 \pm 345$ K, and $n'l = 4.9 \pm 0.2 \times 10^6$ molecules/cm². The intensity for the bottom spectrum is scaled by a factor of 30, reflecting the low column density.

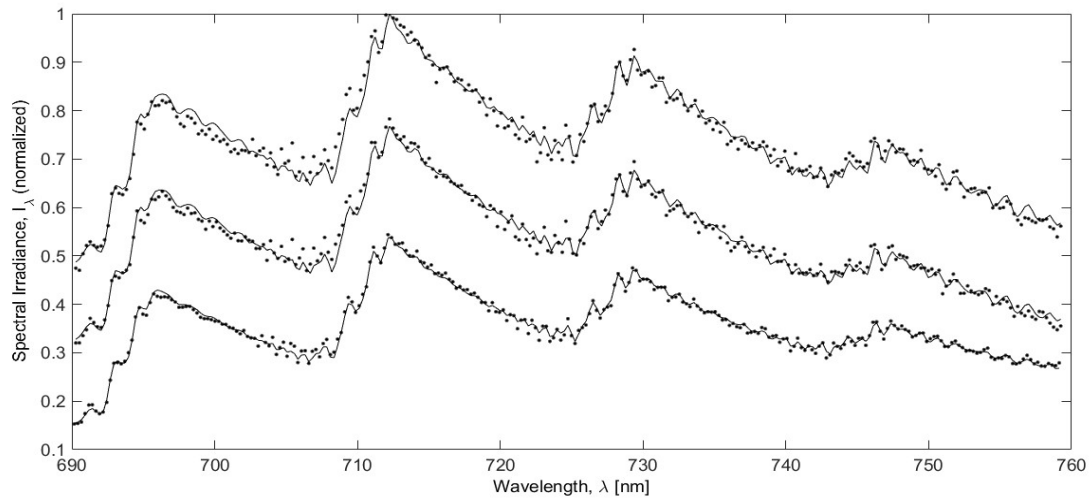


Figure 6. Typical fit of CN $A^2\Pi-X^2\Sigma^+$ $\Delta v=-3$ sequence for: (top) 3.5 kW/cm^2 and medium porosity with $T_r=4300 \pm 295 \text{ K}$, $T_v= 3989 \pm 170 \text{ K}$, and $n'l= 1.2 \pm 0.1 \times 10^{12} \text{ molecules/cm}^2$, (middle) 3kW/cm^2 and medium porosity with $T_r=4150 \pm 249 \text{ K}$, $T_v= 3799 \pm 142 \text{ K}$, and $n'l = 1.1 \pm 0.09 \times 10^{12} \text{ molecules/cm}^2$, and (bottom) 1.4 kW/cm^2 and course porosity with $T_r=3217 \pm 92 \text{ K}$, $T_v=3661 \pm 73 \text{ K}$, and $n'l = 2.7 \pm 0.1 \times 10^{10} \text{ molecules/cm}^2$. The intensity for the bottom spectrum is scaled by a factor of 30, reflecting the low column density.

The column densities (for both $[C_2(d)]$ and $[CN(A)]$) and plume temperatures, T_r and T_v , increase with irradiance. Minimal visible emission is observed for laser irradiances less than 1.4 kW/cm^2 . The $CN(A)$ column densities are 1.5 to 5.5×10^3 times higher than the $C_2(d)$ densities, reflecting the lower electronic energy for $CN(A)$. Optical depths $\sigma_{ji}n_jl$, where σ_{ji} is the absorption transition cross section, were on the order of 10^{-8} for $C_2(a)$ and 10^{-7} for $CN(X)$, justifying the optically thin approximation of Eq. 18. Column densities in an oxyacetylene torch are shown in Table 1 against typical measurements obtained in this study [107]. Total CN and C_2 column densities from this study in Table 2 were determined by assuming that the electronic plume temperature is equal to the $CN(A)$ rotational plume temperature. At high irradiances, similar (order of magnitude) C_2 and CN column densities are recorded. However, contrary to the results from the oxyacetylene torch, for irradiated

graphite, the column density of CN is always higher than that of C₂. Recall, CN violet emission has been observed when ablating graphite in a supersonic air flow with a spectral radiance of a maximum of $750 \frac{W}{cm^2 \mu m sr}$ [105]. When converted to irradiance, this yields $\sim 2 \frac{\mu W}{cm^2 nm}$, very similar to the current results of Figure 4.

Table 2. Comparison of cw graphite irradiation with oxyacetylene torch.

	$[CN(A)]$ * l (cm ⁻²)	$[C_2(d)]$ * l (cm ⁻²)	$[CN]$ * l (cm ⁻²)	$[C_2]$ * l (cm ⁻²)
This study (1.4 kW/cm ² , coarse porosity)	2.7×10^{10}	4.9×10^6	6.0×10^{11}	6.3×10^9
This study (3.0 kW/cm ² , medium porosity)	1.1×10^{12}	5.8×10^8	2.0×10^{13}	2.9×10^{11}
This study (3.5 kW/cm ² , medium porosity)	1.2×10^{12}	8.1×10^8	3.7×10^{13}	1.1×10^{12}
Oxyacetylene Torch [107]	--	--	10^{12}	10^{13}

Spectral simulations for the C₂ Swan and CN red bands became difficult when ejected material had re-solidified on the surface of the sample directly in viewing volume of the spectrometers. As material was removed from the laser-irradiated area, a crater was formed. Nearly all of the test results discussed in this paper were conducted under buoyant conditions, resulting in ejected material lofted vertically up and then redeposited on the top of the crater. Figure 7 shows the formation of ejected material on the graphite surface for a typical 3 kW/cm² medium porosity irradiation. Figure 7(a) shows ejected material rising due to buoyant flow conditions 9 s after the start of laser irradiation. Figure 7(b) shows the beginning of re-solidification of material onto the top part of the crater after only 10 s. Figure 7(c) shows the re-solidified material nearly fully formed at 40 s after laser

irradiation began. This ejected material was observed only for irradiances of 1.4 to 3.5 kW/cm² for all porosities. In addition to the ejected material, the intensity observed by the spectrometer decreased due to the reaction occurring inside the sample as a crater is formed. Figure 7(c) shows the decrease in observed intensity as the reaction is occurring further inside the sample. The decrease in intensity as the chemical reactions began occurring spatially inside the sample made it difficult to spectroscopically observe C₂ Swan and CN red at long irradiation times.

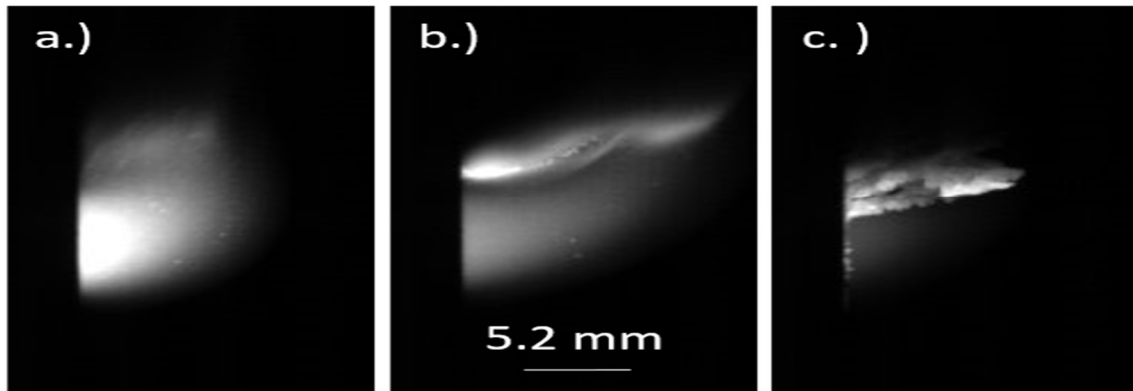


Figure 7. Re-solidification of ejected material from a medium porosity sample irradiated at 3 kW/cm² after (a) 9 s, (b) 10 s, and (c) 40 s.

3.3.2 Surface Temperatures.

Evolving maps of the surface temperature were monitored with the FLIR camera and 3.9 μm band pass filter. Extraction of surface temperature requires knowledge of the sample emissivity, which may be evolving with temperature and surface condition. The spectral emissivity was characterized for both preirradiated and post-irradiated samples as described in the experimental section, and the results are summarized in Table 3. The posttest sample spectral emissivity is most indicative of the thermal steady-state spectral emissivity achieved for the sample. Each measurement included 12 perpendicular

polarized and 12 parallel polarized measurements and averaged to form one emissivity measurement. At least three average emissivity measurements were combined to obtain a final average emissivity. The resulting statistical error was 3.9% for isomolded and less than 2.5% for all other porosities. The largest variation seen between the plane and perpendicular polarized irradiated spectral emissivities was 4.3% observed for coarse porosity graphite; irradiated emissivity variations for all other graphite porosities were less than 1.6%. Using a 3.9% error in the emissivity and assuming a temperature of 3500 K, the standard deviation in the temperature due to emissivity is $\sim \pm 90$ K. The error in the FLIR temperatures under uniform illumination without emissivity error is < 1 K [104], resulting in the obvious conclusion that the largest source of error in the temperature measurements is in the emissivity measurements not the detector.

Table 3. Average emissivity, ϵ , at $\lambda=3.9 \mu\text{m}$.

	Coarse Porosity	Medium Porosity	Fine Porosity	Isomolded Porosity
Un-irradiated	0.735 ± 0.004	0.818 ± 0.007	0.871 ± 0.006	0.852 ± 0.007
Irradiated	0.809 ± 0.020	0.899 ± 0.017	0.925 ± 0.012	0.899 ± 0.035

Figure 8 shows the emissivity-corrected temperature at the center of the laser irradiated spot as a function of time for a medium porosity sample at four irradiance levels. The initial heating rates increase from ~ 200 to ~ 1000 K/s as the laser irradiance increases from 1.4 to 3.5 kW/cm². Steady-state conditions are achieved after 84 s at $T_s = 3500$ K and 13 s at $T_s = 3800$ K for 1.4 and 3.5 kW/cm² laser irradiances, respectively. The sublimation temperature of graphite at low pressure is still controversial, but Abrahamson provides 3895 to 4020 K at 1 atm [50]. The increase in surface temperatures with irradiance plateaus

at $T_s \sim 3800$ K, at the lower range of Abrahamson's measured the sublimation temperature. Figure 8 also shows the ratio of the $[C_2(d)]$ and $[CN(A)]$ column densities. The $C_2(d)$ emission intensity increases more rapidly than $CN(A)$ as temperature increases. The visible emission is very weak for surface temperatures below 3500 K for all cases except for 3.5 kW/cm^2 laser irradiance, where visible emissions are recorded for surface temperatures as low as 2600 K. For the lower irradiances, most of the spectra are recorded near the steady-state conditions. Only for the 3.5 kW/cm^2 case, the surface temperature evolving strongly when visible spectra are observed.

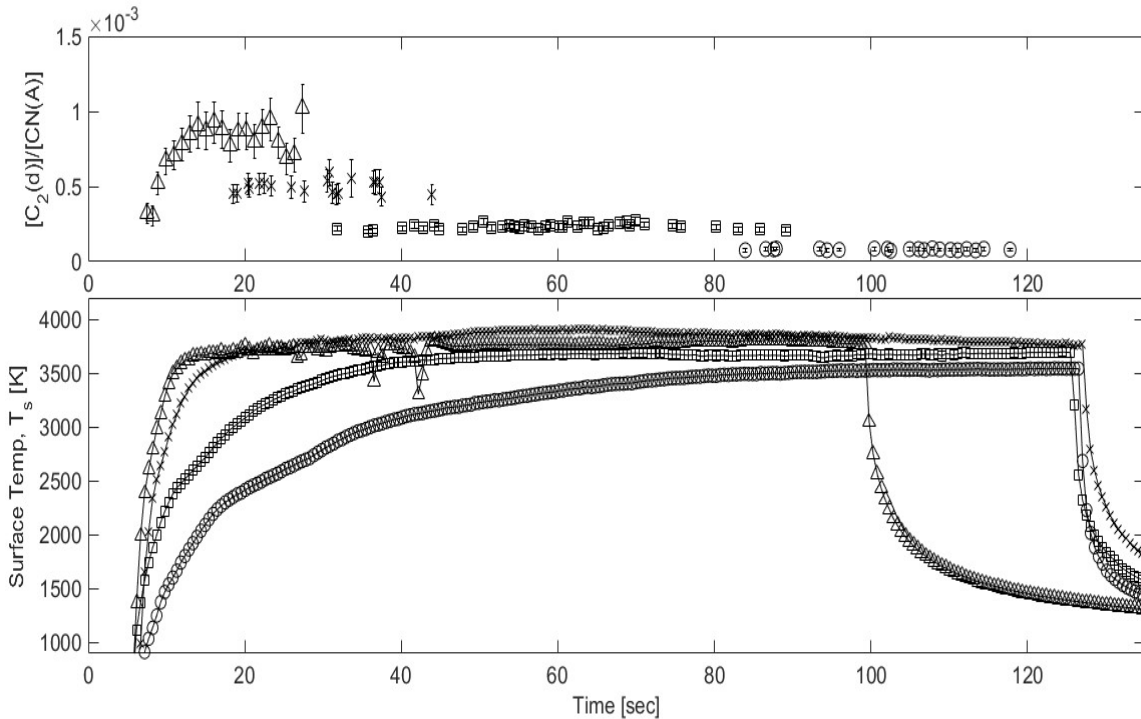


Figure 8. Evolving ratio for C_2 Swan and CN red column densities at (○) 1.4 kW/cm^2 , (□) 1.9 kW/cm^2 , (x) 3 kW/cm^2 and (Δ) 3.5 kW/cm^2 for medium porosity graphite. The corresponding temporally evolving surface temperature (T_s) is shown in the bottom plot.

Figure 9 shows the dependence of the sample surface temperature and the column densities of C₂ Swan and CN red on laser irradiance. Both the surface temperature and the C₂ Swan and CN red column densities generally increase with increasing irradiance. However, the steady-state temperature for laser irradiances of 3 and 3.5 kW/cm² are similar. Phillips et al. showed that sample mass loss continues to increase with increasing energy [49], even though the surface temperature has stopped increasing. Comparing thermal losses due to radiation between a 3 kW/cm² at 4000 K and a 3.5 kW/cm² at 4000 K for an irradiated medium sample with spectral emissivity of 0.90 reveals that the fraction of energy radiated versus absorbed for the 3.5 kW/cm² case is 37% while the fraction of energy radiated versus absorbed for the 3 kW/cm² case is 44%. Presumably the extra energy is consumed in sublimation and mass removal. The steady-state temperature for the 3 and 3.5 kW/cm² irradiances appear to agree well with the sublimation temperature given by Abrahamson [50].

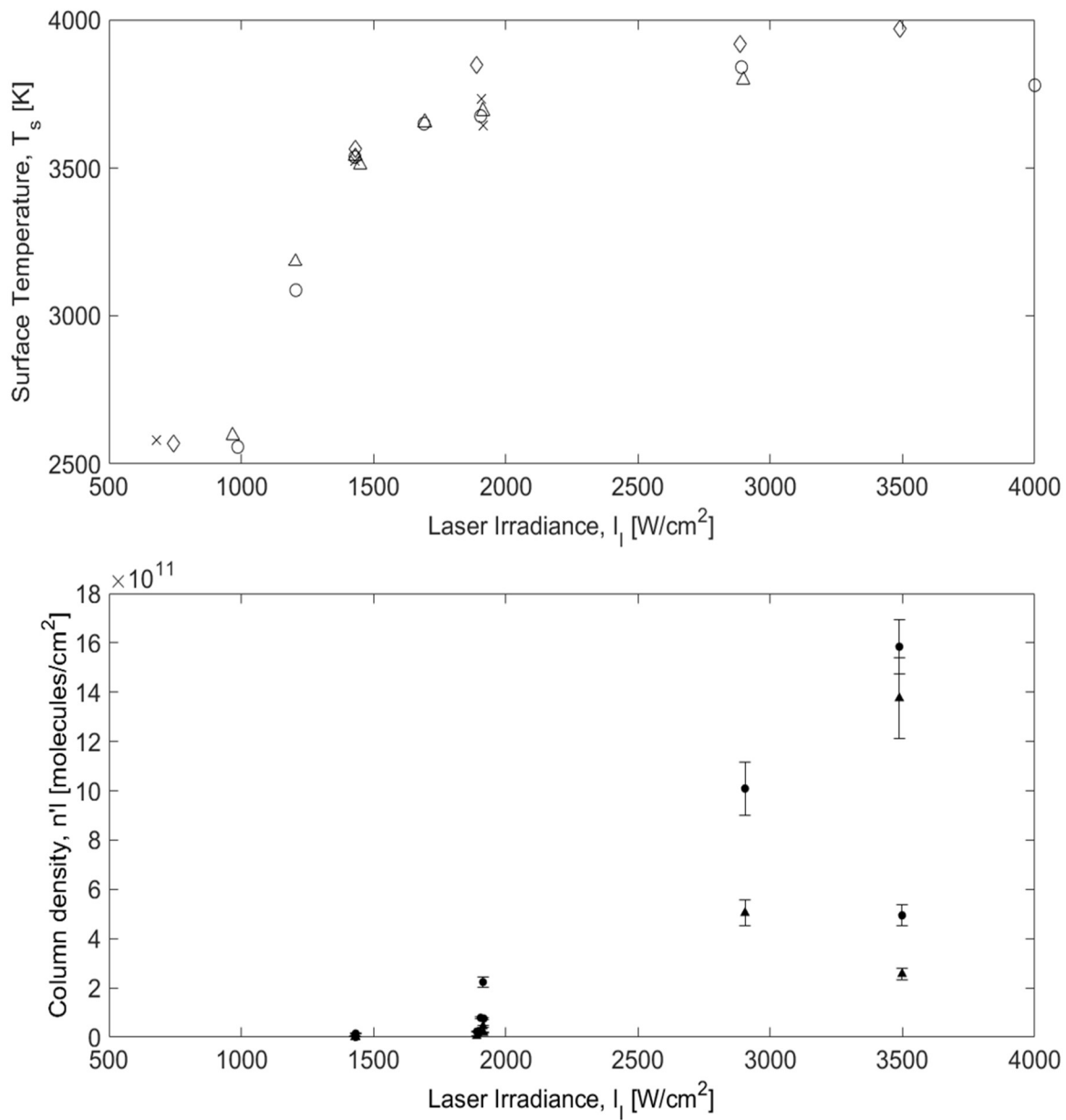


Figure 9. (a) Dependence of surface temperature on laser irradiance for: (○) medium, (◇) coarse, (x) fine, and (Δ) isomolded graphite and (b) Dependence of column density on laser irradiance for (●) C₂ Swan and (▲) CN red. The C₂ Swan densities are increased by a factor of 10³ to share a common axis.

3.3.3 Plume Temperatures

Figure 10 shows the gas plume temperatures derived from the spectral simulation fits and the corresponding graphite surface temperatures. The 2σ statistical error bounds are on average ± 240 K for the rotational temperature of CN red, ± 300 K for the rotational temperature of C₂ Swan bands, and ± 150 K for the vibrational temperature of CN red. A reference line for equal surface and gas temperatures are also shown in Figure 10. Gas temperatures range from ~ 2400 to ~ 5100 K with an average of 3834 ± 224 K. While the scatter is large, the CN rotational temperatures are generally lower than CN vibrational temperatures by 343 ± 55 K. The accuracy of the data does not support any conclusion regarding nonequilibrium conditions.

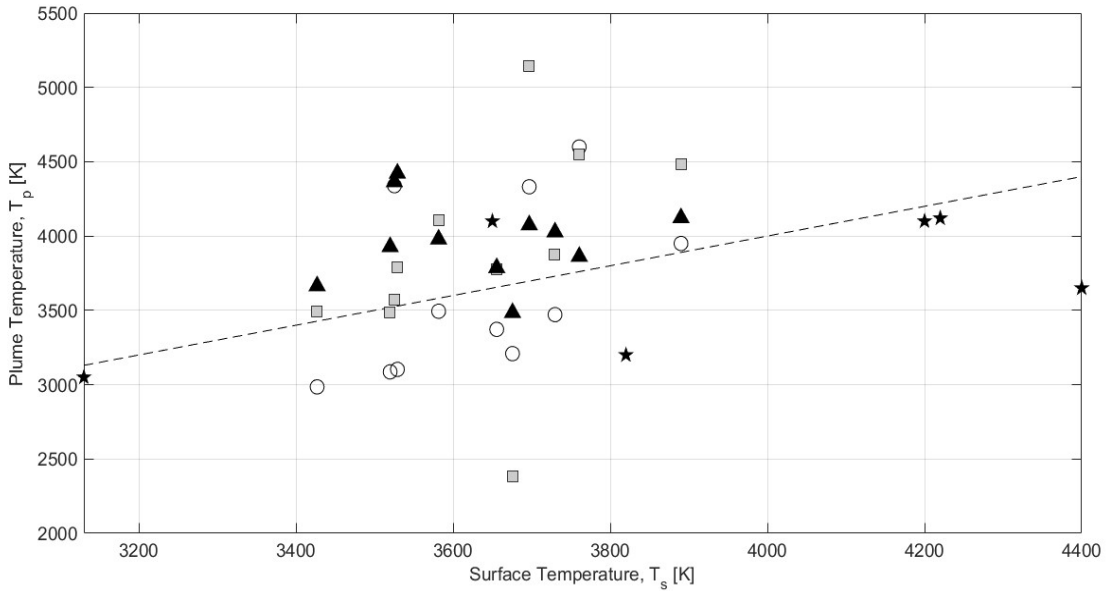


Figure 10. Surface temperatures, T_s and plume temperatures: (\circ) T_r from CN red, (\square) T_r from C₂ Swan, (\blacktriangle) T_v from CN red, for all graphite porosities and laser irradiances. Prior results for T_r from C₂ Swan bands reported in [20] (\star). A reference line for equal surface and plume temperatures is also provided (--).

Temperatures from the Whittaker et al. CO₂ laser study [91] are also compared with the present results in Figure 10. No error bounds were given with the Whittaker et al. data, but the results also appear to track the surface temperature fairly well [91]. The rotational temperatures derived by Whittaker et al. also use the C₂ Swan $\Delta v=0$ bands. Nearly all of the C₂ rotational temperatures in the present study are higher than the corresponding surface temperatures while nearly all Whittaker et al. rotational temperatures are lower than the corresponding surface temperatures. The majority of the Whittaker et al. study was conducted in Ar background whereas all of the experiments in this paper were conducted in air. Indeed, Whittaker et al. noted that their rotational temperature is higher than the surface temperature only for conditions in which 20% O₂ was added into the vacuum chamber. Whittaker et al. attributed the increased observed gas temperature to oxidation reactions.

3.3.4 Column Density

The temperature dependence of the relative excited column density, $[C_2(d)]/[CN(A)]$, for all graphite samples and laser irradiances is shown in Figure 11(a). At all but the highest irradiance, the only spectra observed are for steady-state surface temperatures (as seen in Figure 8) and each data point in Figure 11(a) represents a different test. The C₂(d) Swan band column density increases more rapidly with surface temperature than the CN(A) red band column density (see Figure 9(b)). However, the C₂(d) column density is much lower than for CN(A). The C₂ d³Π_g state lies well above the ground state with an electronic energy of 20,026 cm⁻¹, whereas the CN A²Π state has an electronic

energy of 9243 cm^{-1} . At surface temperatures of 3400 to 3900 K (or corresponding energies of 2350 to 2700 cm^{-1}), the lower lying CN(A) state is more accessible.

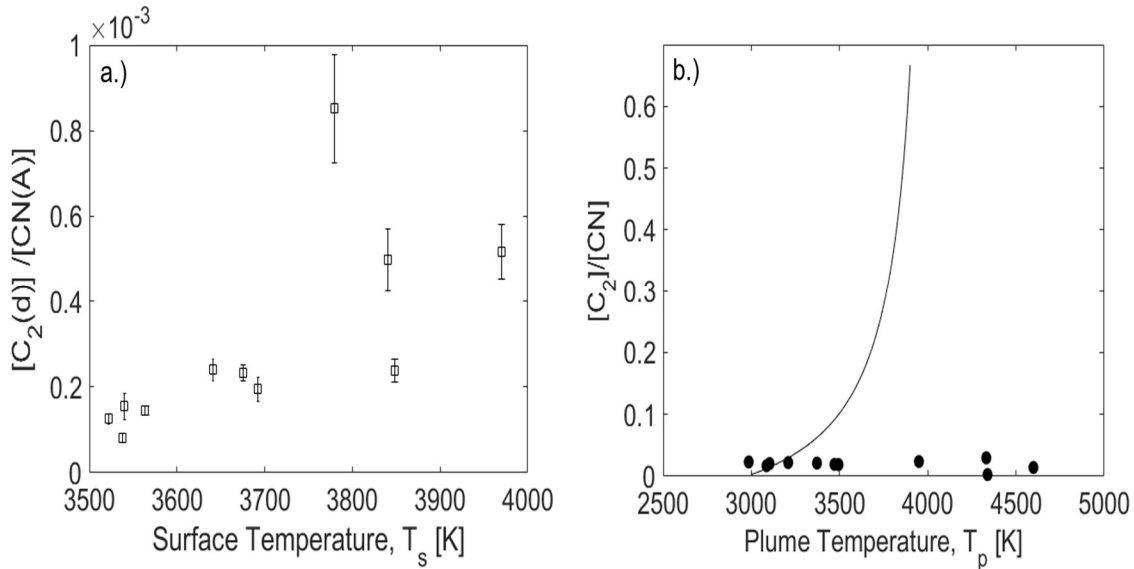


Figure 11. (a) $[C_2(d)]/[CN(A)]$ density ratio vs surface temperature and (b) $[C_2]/[CN]$ density ratio vs plume temperature compared with (—) analysis from NASA's Chemical Equilibrium Analysis (CEA) code. The C_2 and CN densities were calculated with an electronic temperature equal to the CN(A) rotational temperature and the error bounds for $[C_2]/[CN]$ values in (b) were on average 13%.

As a basis for comparison with the observed reaction dynamics, an equilibrium analysis was performed using NASA's Chemical Equilibrium Analysis (CEA) code, analyzing for N_2 , O_2 , NO , N , O , CO , CO_2 , NO_2 , CN , C , C_2 , C_3 , C_4 , and C_5 for temperatures ranging from 100 to 8000 K at 1 atm pressure. In this analysis, the total C_2 and CN mass fractions are computed assuming equilibrium conditions; the results are reported as a ratio in Figure 11(b). The CEA results reveal for temperatures greater than 3000 K, that an increase in the C_2 mass fraction is accompanied by a corresponding smaller increase in the CN mass fraction, resulting in the upward curvature in the $[C_2]/[CN]$ ratio. To compare, the column densities for C_2 Swan and CN red bands observed from the laser irradiation

experiments described in this paper were converted to total column densities for C₂ and CN by assuming an electronic state Boltzmann distribution defined by an electronic temperature equal to the CN(A) rotational temperature (see Eq. 20). A partition function was then calculated for all of the lowest levels from the ground state to electronic states of ~25,000 cm⁻¹ and applied to the ground states to determine the total C₂ and CN column densities. In Figure 11(b), the total [C₂]/[CN] ratio is dramatically less than the CEA prediction. To achieve [C₂]/[CN] similar to what is calculated by CEA, electronic temperatures of on average 2500 K were required for experimental laser irradiances from 1.4 to 3.5 kW/cm², which is in general ~1300K lower than what is observed for the gas temperatures.

There is considerable error introduced in extrapolating to total C₂ and CN concentrations from the observed excited state column densities, even though the 2σ statistical error bounds for [C₂(d)] and [CN(A)] are in general less than 10%. The correlation of column density with temperature is minimal, as the concentrations reflect the area under the spectral features, whereas the shape of the band defines rotational temperatures. Therefore, large variation in rotational and vibrational temperatures does not significantly affect fit values for [C₂] and [CN]. However, the large variance in plume temperatures reported in Figure 10 and the lack of experimental evidence for the electronic temperature limits our ability to predict total concentrations.

Acosta et al. performed similar graphite laser irradiation experiments with the goal of analyzing graphite oxidation and combustion [79]. Their results show column densities for carbon oxidation products CO and CO₂ on the order of 10¹⁷ molecules/cm² for laser

irradiation of similar graphite samples at 777 W/cm^2 . As was mentioned previously, C_2 and CN were not observed for irradiances less than 1.4 kW/cm^2 in this paper. At 1.4 kW/cm^2 , average column densities were on the order of 10^9 and 10^{11} molecules/ cm^2 and at 3.5 kW/cm^2 on the order of 10^{12} and 10^{13} molecules/ cm^2 for C_2 and CN and, respectively, assuming an electronic temperature equal to the CN(A) rotational plume temperature. The results given by Acosta et al. are at least six orders of magnitude higher than observed column densities for CN and C_2 for laser irradiation of graphite at 1.4 kW/cm^2 , indicating that oxidation is a more important process in reactions of graphite due to laser heating than nitridation, especially at lower irradiances.

Acosta et al. also compared the experimentally determined CO and CO_2 column density ratios to those from an equilibrium analysis and showed discrepancies [79]. Acosta et al. theorized that oxygen in the reaction boundary layer might be depleted and that the deviation from equilibrium would be from diffusion-limited oxygen. While the production mechanisms of C_2 and CN from cw laser irradiation are not known, the fact that the graphite oxidation kinetics is not consistent with an equilibrium analysis would indicate that C_2 and CN would likely not be consistent with an equilibrium analysis either, confirming the discrepancy between the CEA analysis and experimental data observed in this study. Further detailed study needs to be accomplished to determine just how influential the oxidation kinetics are on the C_2 and CN production from cw laser irradiation of graphite.

3.3.5 Buoyant Versus Stagnant Flow

A comparison between a sample irradiated at 1.4 kW/cm^2 under buoyant and stagnating flow (5 m/s air flow) conditions revealed that the buoyant sample results in a

~21 times lower $[C_2(d)]/[CN(A)]$ ratio than the sample under flowing air conditions due to a factor of ~43 decrease in $[C_2(d)]$. The vibrational temperature of CN is the same for the test shots under buoyant flow and with 5 m/s flow, which is higher than the rotational CN temperature in both cases. The C_2 rotational temperature is higher, and the CN red rotational temperature is lower for the sample irradiated under flow conditions. The surface temperature of the sample under stagnating flow conditions showed 134 K higher surface temperature than the sample under buoyant conditions. Phillips et al. recorded a significantly larger mass loss with increased flow conditions, in particular an $\sim 2\times$ mass loss increase with increasing deposited energy for a 5 m/s flow for fine porosity graphite [49]. There is a direct correlation between an increased amount of C_2 present and an increase in mass loss for a sample irradiated under stagnating flow.

3.4 Conclusion

Graphite laser heating under high irradiance, cw conditions with deposited energies as high as 1 MJ has been analyzed utilizing visible emission spectroscopy, surface temperature measurements, and fast visible photography. C_2 Swan and CN red bands have been analyzed to determine gas temperatures ranging up to 5140 ± 380 K and column densities ranging up to $1.6 \pm 0.1 \times 10^{12}$ molecules/cm² for CN(A) and $1.4 \pm 0.2 \times 10^9$ molecules/cm² for $C_2(d)$ at the highest laser irradiances of 3.5 kW/cm². No $C_2(d)$ or CN(A) is observed at irradiances less than 1.4 kW/cm². The ratio of molecular products C_2 Swan and CN red is insensitive to porosity of graphite but increases with laser irradiance and surface temperature. Thermal steady-state conditions in the samples are reached at less than 20 s for high irradiance cases (3 to 3.5 kW/cm²), at which point $[C_2(d)]/[CN(A)]$ is

constant. Increased air flow on the sample leads to 21 times higher $[C_2(d)]/[CN(A)]$ concentration ratio despite surface temperatures that remain within 3.8% of buoyant flow surface temperatures. Low column densities relative to oxidation products CO and CO₂ (10^6 times less) suggest that C₂ and CN forming reactions are relatively insignificant. The ratio of C₂ and CN total column densities extrapolated from the observed excited states is less than an equilibrium analysis predicts using the surface or plume temperatures. A detailed computational study of the kinetics and diffusion during irradiation is required to further interpret the experimental findings. The impact of carbon nitridation (CN(A) production) on laser penetration of graphite appears minimal.

IV. Comparison of plume dynamics for laser ablated metals: Al and Ti

Emissive plumes from pulsed laser ablation of bulk Ti and Al from KrF laser irradiation at laser fluence up to 3.5 J/cm^2 and argon background pressures of 0-1 Torr have been observed using gated ICCD imagery. Mass loss for Ti increases from 0.1–0.8 $\mu\text{g/pulse}$ as pulse energy increases from 174–282 mJ/pulse (35-170 photons/atom) and decreases by ~30 % as pressure increases from vacuum to 1 Torr. Early plume energies are described by free expansion velocities of 1.57 ± 0.02 and of $1.81 \pm 0.07 \text{ cm}/\mu\text{s}$ for Ti and Al, respectively and up to 90% of the incoming laser energy can be attributed to the Al shock front in the mid-field. The ablation thresholds of $90 \pm 27 \text{ mJ}$ ($1.12 \pm 0.34 \text{ J/cm}^2$) for Ti and $126 \pm 13 \text{ mJ}$ ($1.58 \pm 0.16 \text{ J/cm}^2$) for Al also represent 30–70 % of the incident laser energy. The decrease in mass loss at higher pressures is attributed to plasma shielding of the target surface.

4.1 Introduction

The laser ablation and emissions plume creation process is complex, encompassing melting and vaporization of the target surface, generation of a plasma from the established vapor plume, laser absorption of the incoming laser radiation by the plume, and expansion of the plume away from the target surface [15], [41]. These laser induced plasmas are highly ionized [68], expand into the background gas with shock speeds of $> 1 \text{ cm}/\mu\text{s}$ [108], [109], and exhibit hydrodynamic phenomena such as plume splitting and Rayleigh-Taylor instabilities [40], [70], [110]–[113].

Knowledge of the plume dynamics is essential to the pulsed laser deposition (PLD) of thin films where a substrate is typically placed 1-20 cm from the target in a background

pressure of 0.1-1.0 Torr [15]. Pulsed laser deposition of titanium is increasingly utilized to create nitinol coatings for orthopedic implants [110], nitrogen doped titanium oxide for photocatalysts [111], and TiN layers for diffusion barriers in microelectronics and tribological coatings for high speed tools [112]. The production of molecular constituents and nanoparticles [40], [70], [113]–[115] usually requires slowing the plume by incorporating rare gas, nitrogen or oxygen background gases, with plume stopping distances located near the substrate. Laser induced breakdown spectroscopy (LIBS) produces similar plumes, but propagate shorter distances and evolve more rapidly, due to the higher, atmospheric pressure conditions [25]. In the present study we compare the plume dynamics for pulsed laser ablation of two common aerospace metals, Al and Ti [1], [24]. Laser cutting, welding and additive manufacturing using Al or Ti depend on understanding the laser material interaction, typically at lower irradiance [24]. The response of these metals to high power laser radiation is also important to the effectiveness of emerging laser weapon systems [1].

Experimental characterization of laser ablated plumes and corresponding shockwaves have been conducted using shadowgraphy [31], [116], optical emission spectroscopy [36], [63], [117], charge collection devices [39], [108], [118], [119], and laser induced fluorescence [109], [120]. These techniques offer insights into the plume expansion process and its constituents but provide limited information regarding structure of the emissive plume. Fast visible emissions imaging through the use of ICCD arrays has been extensively utilized to image laser ablation plumes [15], [33], [71], [121], [122]. ICCD imaging offers the advantage of being able to record the structure of the emissive plumes in a 2D image with ~ 1 ns temporal resolution and ~ 100 μm spatial resolution.

The pulsed ablation of aluminum has been studied in some detail, including Nd:YAG sources at 1.06 μm [31], [33], [34], [121], sources with greater than 1 ns duration at shorter wavelengths [27]–[30], [115], and short pulse (fs) sources [35]. Background gases of air, rare gases, and nitrogen at pressures up to atmosphere have been examined, with plume stopping distance reported for low pressure nitrogen backgrounds [33], and expansion dynamics characterized at atmospheric pressures [31], [32], [121]. The scaling of Al plume dynamics and mass loss for UV laser sources is largely unstudied. Pulse laser ablation of titanium has received considerably less attention, with the studies limited to short pulse effects in vacuum [112], deposition of nitinol films in vacuum [110], and LIBS at 532 nm [123]. In the present study, we seek to compare the plume dynamics for Al and Ti targets irradiated at 248 nm to examine the influence of atomic momentum on plume thickness and plume slowing, and resolve plume structure for low argon background pressures. In addition, we compare the dependence of mass removal on laser fluence and background pressure with the plume energy driving shock formation. This systematic study of ablated mass and plume dynamics will be used to better understand the implications of background pressure scaling relationships. By defining the background pressure conditions for well-formed plume fronts, future studies of evolving velocity distributions, shock front instabilities, and translational-to-electronic excitation rates is enabled.

4.2 Experiment

A schematic of the experimental apparatus is presented in Figure 12; further details of the experiment have been reported previously [44]. Briefly, a Lambda Physik LPX 305 KrF laser at $\lambda=248$ nm delivered up to 282 mJ/pulse on the target in an 8 x 1 mm rectangular

spot with a repetition rate of 1 Hz. The plume propagates normal to the target in the z -direction and the gated camera observes the plume from above, integrating along the y -direction. The pulse exhibits a FWHM of 25 ns and a rise time of 5 ns, yielding an intensity of 141 MW/cm^2 . The damaged area as observed by optical microscopy is similar to the laser footprint, as seen in Figure 13. The laser beam is focused onto the target inside the 10" vacuum chamber through a 300 mm focal length plano-convex fused silica 2" lens at an angle of incidence of ~ 45 degrees to the target normal. The chamber was evacuated to a base pressure of 10^{-6} Torr with a turbomolecular pump before being backfilled with the desired pressure of 99.999% Ar (50, 250, 500, and 1000 mTorr). Pressures were monitored by an MKS capacitance manometer with a 1-1000 mTorr range ($\pm 0.5\%$ of reading) and an ionization gauge for near vacuum conditions.

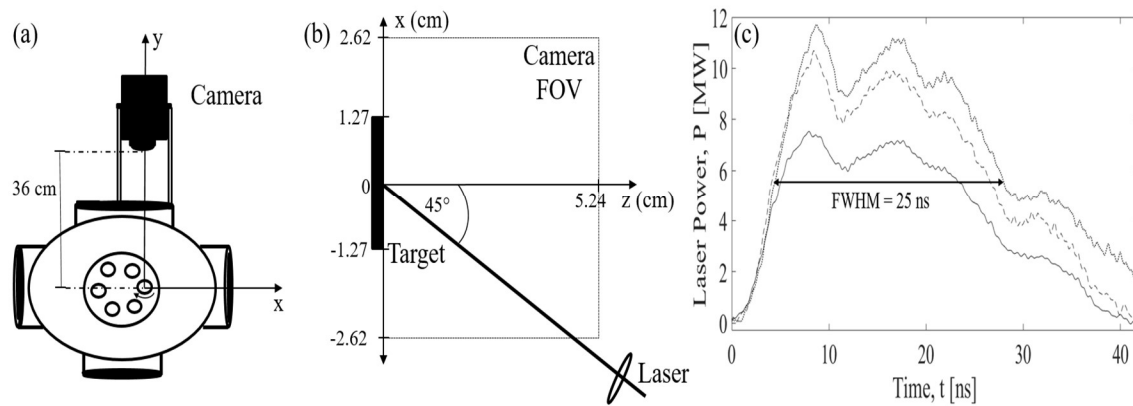


Figure 12. Experiment apparatus in (a) x - y plane (b) and x - z plane (dimensions specific to 50 mm lens imaging system) and (c) laser pulse shape for (.) 282 mJ/pulse, (--) 240 mJ/pulse, and (-) 174 mJ/pulse.

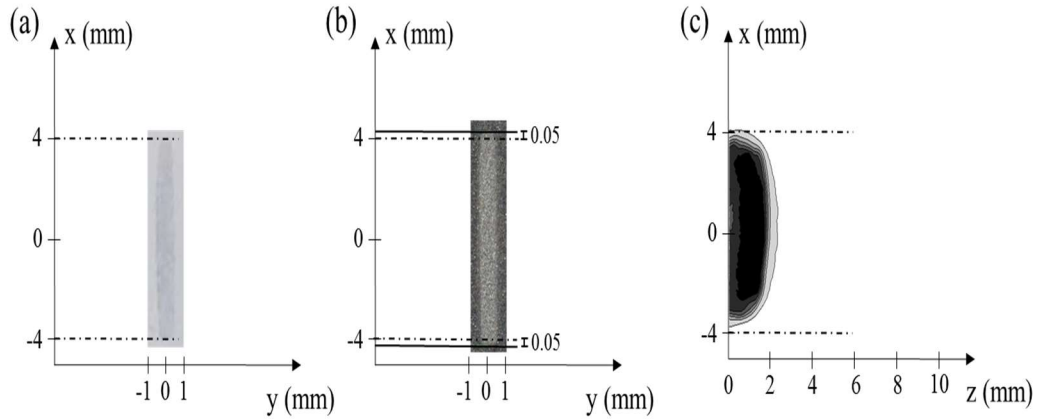


Figure 13. (a) Laser spot at target from thermal paper burn pattern, (b) optical microscope image of Ti damage, and (c) Ti 224 mJ/pulse ablation plume in 500 mTorr Ar at 141 ns delay.

The targets were Kurt Lesker 1” diameter by 0.25” thick sputtering targets typically of either 99.99% Al or 99.7% Ti. Targets were mounted onto a carousel allowing up to 6 targets into the chamber at one time. Each of the targets is rotated at 10 rpm about the z-axis during laser irradiation to reduce surface cratering. Laser energy delivered to the target was measured by utilizing a Coherent LMP10I detector calibrated to a wavelength of 248 nm positioned inside the target chamber. Images suffer from <5% pulse-to-pulse laser flicker and ≤ 10 ns pulse-to-pulse laser timing jitter. Typical thermal and optical properties of Al and Ti are provided in Table 4.

Table 4. Ti and Al Material Properties [41], [47]

	Al	Ti
Molar Mass, M (g/mol)	26.98	47.87
Density, ρ (g/cm ³)	2.7	4.506
Melting Temperature, T_m (K)	933	1,943
Vaporization Temperature, T_v (K)	2,792	3,560
Enthalpy of Melting, ΔH_m (J/g)	397	295.6
Enthalpy of Vaporization, ΔH_v (J/g)	10,896	8,800
Spectral Reflectance, R ($\lambda=248$ nm, $\phi_i=0^\circ$)	0.9244	0.236
Heat Capacity, C_p (J/g*K) (T=300K)	0.9	0.52
Thermal Diffusivity, D (cm ² /s) (T=300K)	0.98	0.093
Absorption Coefficient, α (cm ⁻¹) ($\lambda=248$ nm)	1.49×10^6	6.13×10^5
Ionization Potential, I (eV)	5.99	6.83

ϕ_i is the angle of incidence.

Fast visible emissions images were captured utilizing a Princeton Instruments PIMAX I intensified charged-coupled device (ICCD). The 512 x 512 array PIMAX I was equipped to image early delays and short plume distance emissions with a Nikon AF Nikkor 60 mm micro f/2.8 lens that provided a field of view (FOV) of 5.24 x 5.24 cm (0.102 mm per pixel) or to image longer time/farther spatial distance plume details when equipped with a Nikon AF Nikkor 50 mm f/1.4 lens that provided a FOV of 8.28 x 8.28 cm (0.162 mm per pixel). The point spread function has been characterized and is somewhat larger, 0.5 mm for the 60 mm imaging system and 1.1 mm for the 50 mm imaging system [44]. The camera was gated with integration times ranging from 2-150 ns and delays of up to ~12 μ s after the onset of irradiation. Both the widths and delays were varied nonlinearly over 100 shots and the laser electronics were utilized to trigger the camera. For the initial plume speeds of ~2 cm/ μ s presented below, the 2 ns integration

time implies a 40 μm or 0.39 pixel motion during image capture. The plume slows and decreases in intensity at later times, allowing for the longer integration times to improve the signal to noise ratio, with < 4 pixel motion during the image capture. The 16 bit camera saturates at 65,536 counts with a dark signal of 68 counts. The PIMAX camera quantum efficiency is above 20% from 410-890 nm, with a maximum quantum efficiency of $\sim 40\%$ at approximately 700 nm. Band pass filters were employed to isolate the emission from neutral and ion atomic species [44]. The broadband emissions include ≤ 10 lines for Ti and two lines for Al, with the dominant lines exhibiting radiative rates of $\geq 7 \times 10^7 \text{ s}^{-1}$ [72]. Plume motion during a radiative lifetime for the faster emitters is $\leq 0.3 \text{ mm}$, resulting in the conclusion that emission is produced locally (within 3 pixels).

An example plume image shortly after the laser pulse is provided in Figure 13(c). The plume lateral extent at the target matches the laser footprint. The plume has expanded to $z = 2.4 \text{ mm}$ in 141 ns, yielding an initial velocity of $\sim 1.7 \text{ cm}/\mu\text{s}$. At the end of the laser pulse, $t = 25 \text{ ns}$, the plume volume is $\sim 3.4 \text{ mm}^3$.

Mass loss experiments were performed with a Mettler Toledo XP26 microbalance (minimum resolution of 0.001 mg) as functions of pressure and laser energy. The $\sim 14.5 \text{ g}$ Ti and $\sim 8.8 \text{ g}$ Al samples were received from the vendor sealed in Ar. They were opened under atmospheric conditions and allowed to oxidize and hydrolyze until stable ($\sim 30 \text{ min}$) with mass increases of 44 μg and 56 μg for Ti and Al, respectively. Samples were weighed on the XP26 before being placed into the chamber for irradiation. The chamber was evacuated to base pressure for at least 12 hours before being backfilled with the desired amount of Ar. Samples were irradiated for 600 shots at 1 Hz with the sample rotating about

the z -axis before being removed and then re-weighed on the XP-26. Samples were measured a minimum of 5 times on the XP-26 before and after irradiation with a variance of $< 1\%$. All results were averaged equally over the 600 shots to determine the amount of mass loss per pulse.

4.3 Results and discussion

4.3.1 Mass Loss

The amount of material ablated per pulse as a function of laser energy and background pressure for both Al and Ti targets is summarized in Figure 14 and Table 5. Generally, more material was ablated from both targets with increasing laser energy. The maximum Ti mass removed of $0.80 \mu\text{g/pulse}$ ($\sim 482 \mu\text{g}$ in 600 pulses) occurs at the greatest delivered energy of 282 mJ, corresponding to 35 laser photons (175 eV) per ablated atom. The amount of mass ablated from a typical Ti target was on average 49% higher than the amount ablated for Al. However, due to its higher molar mass, 26% fewer Ti atoms are produced than Al, consistent with the lower melting and vaporization temperatures of Al.

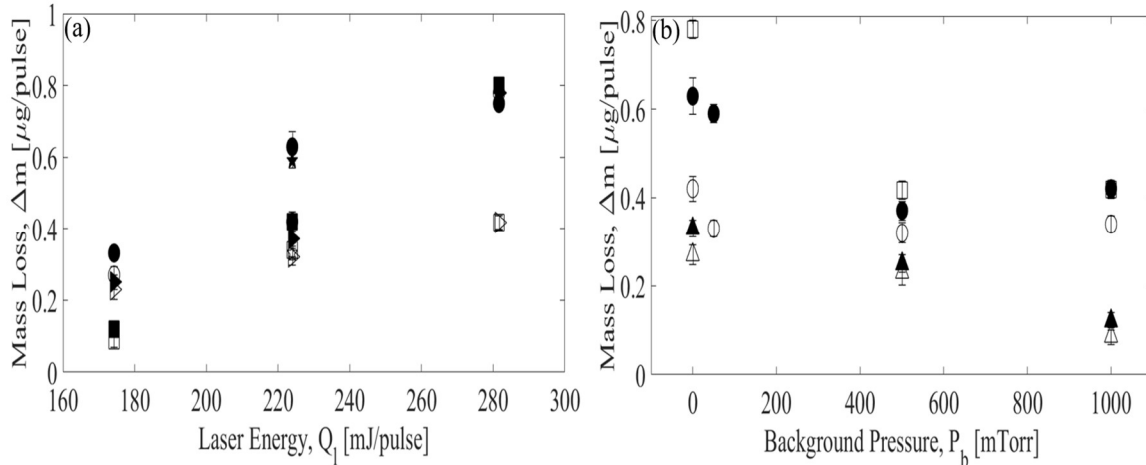


Figure 14. (a) Dependence of mass loss on laser energy (●) Ti vacuum, (★) Ti 50 mTorr, (▶) Ti 500 mTorr, (■) Ti 1000 mTorr, (○) Al vacuum, (☆) Al 50 mTorr, (▷) Al 500 mTorr, (□) Al 1000 mTorr, and (b) dependence of mass loss on background pressure (▲) Ti 174 mJ/pulse, (●) Ti 224 mJ/pulse, (△) Al 174 mJ/pulse, (○) Al 224 mJ/pulse, and (□) Al 282 mJ/pulse.

The mass removal reported in Figure 14 is similar to previous results, although the exact conditions of the experiments in this study are not replicated elsewhere. Sdorra et al reported Al mass loss of $0.5 \mu\text{g}$ per pulse from the 4th harmonic of an Nd:YAG laser ($\lambda=266 \text{ nm}$) at $3.2 \text{ GW}/\text{cm}^2$ for an Al target in 100 Torr of Ar using optical microscopy [124]. Iida reported Al mass loss of $0.33 \mu\text{g}$ per pulse from the 1st harmonic of an Nd:YAG laser ($\lambda=1064 \text{ nm}$) at $9.5 \text{ GW}/\text{cm}^2$ in 0.1 Torr Ar using a microbalance [125]. Torrisi et al ablated Al with the second harmonic of an Nd:YAG laser ($\lambda=532 \text{ nm}$) in vacuum and recorded results of $0.28 \mu\text{g}$ at 170 mJ/pulse laser energy [126]. Timm et al reported mass loss for the closest conditions to those of this work. KrF ablation of Al and Ti at $0.12\text{-}1.6 \text{ GW}/\text{cm}^2$ at vacuum pressure was performed and mass losses of $\sim 0.02 \mu\text{g}$ of Al and $\sim 0.1 \mu\text{g}$ of Ti at $0.19 \text{ GW}/\text{cm}^2$ were recorded using a gravimetric balance and averaging over multiple shots [127]. Their results appear to be lower than those recorded in this study and the results of the other two studies.

Figure 14(b) generally illustrates less mass ablated at higher background pressure. This observation is further supported through a determination of Ti mass removal rates using linear fits of mass removed as a function of laser energy for varying background pressures (Table 5). The average increase in Ti mass removal with laser fluence is $5.3 \pm 0.67 \mu\text{g/J}$, with pressure specific results provided. Error bounds in Table 5 and the remainder of this paper reflect the statistical 1σ error in the fit parameter. While the mass loss results in Figure 14(b) generally decreased with increasing background pressure, one exception to this trend is the Ti ablation mass loss results at 282 mJ/pulse, which is not displayed. In this case, a mass loss of $0.78 \pm 0.03 \mu\text{g}$ is observed, independent of background pressure.

Extrapolations of the linear response of ablated mass with laser energy to zero mass reveal ablation thresholds of $\Phi_{\text{th}}=1\text{-}2 \text{ J/cm}^2$. Ablation thresholds are often calculated using the energy required to bring a volume of target material to a specified temperature [41], [128], [129]

$$E_{th} = \frac{A\rho(\Delta H)(\alpha^{-1} + \sqrt{D\tau_{laser}})}{(1 - R)} \quad (21)$$

where the material properties are defined in Table I and the enthalpy change may include heat capacity and latent heats for melting and vaporization. The details for the evolving reflectivity at elevated temperatures and the temporal evolution of the ablated mass are not addressed in Eq. 21, but the result is an adequate approximation that correlated the thresholds for many metals [130]. Using the heat of vaporization only and excluding reflection yields thresholds of 1.98 and 4.7 J/cm² for Ti and Al, respectively. Observed

thresholds for ns ablation sources at various wavelengths range from 2 to 2.4 J/cm² for Ti [40], [127], and 2.3 to 3.6 J/cm² for Al [30], [127], [130].

Table 5. Mass removal parameters.

Metal	Ar Pressure (Torr)	$\Delta E / \Delta m$ (mJ/ μ g)	E_{th} (mJ)	Φ_{th} (J/cm ²)
Ti	0	239 \pm 44	90 \pm 27	1.12 \pm 0.34
Ti	0.5	190 \pm 32	138 \pm 17	1.73 \pm 0.21
Ti	1.0	158 \pm 3.1	156 \pm 1.6	1.95 \pm 0.20
Al	0	204 \pm 25	126 \pm 13	1.58 \pm 0.16
Al	1.0	292 \pm 68	144 \pm 21	1.80 \pm 0.26

As the Ti background pressure increases from vacuum to 1 Torr, the apparent fluence threshold increases by 66 mJ. Prior studies attributed a significant decrease in mass loss at higher background pressure to plume confinement and increased laser shielding of the target [125], [131]. Assuming negligible particle re-deposition (see discussion below), the 66 \pm 27 mJ increase in the apparent fluence threshold represents a 28 \pm 11% increase in shielding of the target surface.

It has been observed that particle re-deposition increases with increasing background pressure during UV metal laser ablation, offering a second explanation of the results of Figure 14(b) [132]. Visible inspection of post-irradiated samples show that samples irradiated in vacuum exhibit deeper looking ablated laser spots than do samples at higher pressure, indicating a higher rate of ablation at lower pressure. Optical microscopy of the post-irradiated samples do not exhibit obvious re-deposited material. Furthermore, the samples were swabbed to determine qualitatively if re-deposition was present. Very

faint amounts of debris were observed on some Ti and Al sample swabs, with no apparent trend due to pressure or laser energy. Finally, the analysis of the plume dynamics from the imaging discussed in Section 4.3.3 below provides additional insights into this topic. It will be observed that the plume accelerates during the laser pulse, the initial plume kinetic energy declines at higher background pressures, and the shock front expansion does not properly scale with a constant plume mass. Eventually it will be concluded that plume shielding rather is more significant than mass re-deposition.

4.3.2 Plume Imagery

Gated imagery reveals key information regarding the shock development, plume kinetic energy and evolution of velocity distributions. The qualitative features of the plume imagery are now examined. Typical fast visible imaging contour plots of KrF ablation of Ti at 1000 mTorr are presented in Figure 15. The intensities in each frame are normalized to the maximum observed for that individual gate to highlight the relative features. The initial plume size matches the laser spot and damage area. The Ti emissions expand into the Ar background at an initial velocity of ~ 1.6 cm/ μ s. At ~ 10 μ s, the plume has reached its stopping distance of 2.8 cm.

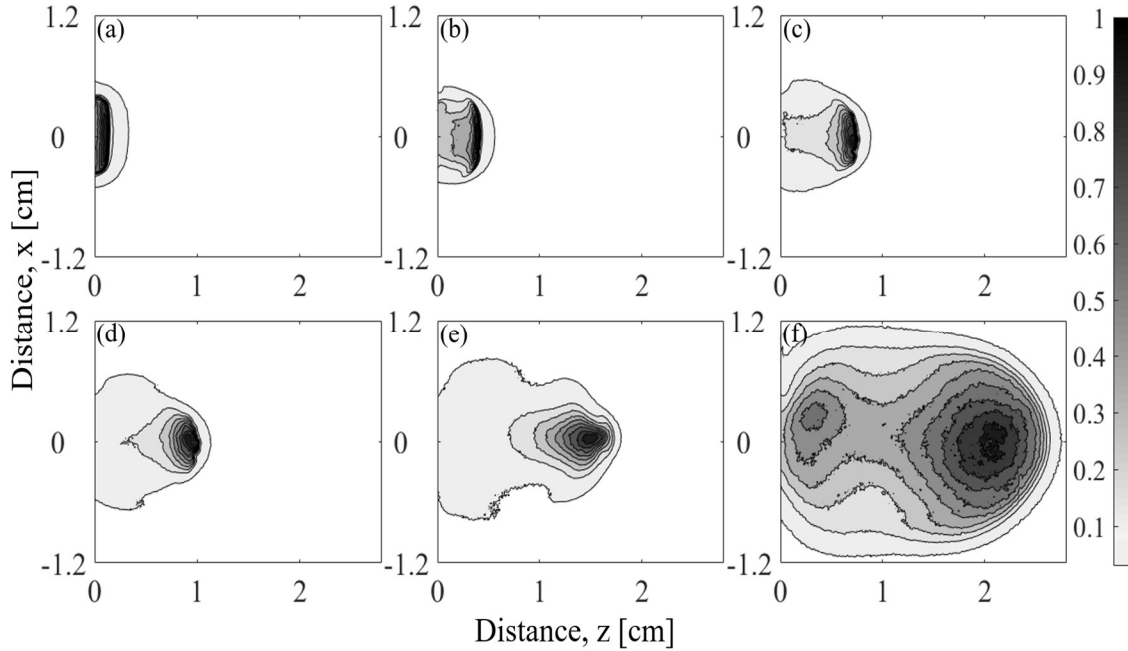


Figure 15. Intensity contour images of Ti ablation at 224 mJ 1000 mTorr Ar at (a) 97 ns, (b) 295 ns, (c) 684 ns, (d) 1.13 μ s, (e) 2.8 μ s, and (f) 9.85 μ s delay times.

The Al ablation plume follows the same general plume dynamics as Ti. However, Al slows more rapidly because it loses relatively more momentum per collision due to its lower molar mass (assuming both Al and Ti plumes expand at comparable speeds). In Figure 16, the plume comes to shorter stopping distance, 2.1 cm, at earlier time despite the lower pressure. Hydrodynamic vortices are readily observed as the plume slows due to collisions with the background gas and circles around towards the lower pressure edges of the plume. The rotational rate was estimated to be 8.3×10^5 rad/s at a radius of approximately 1.7 cm measured from the target surface.

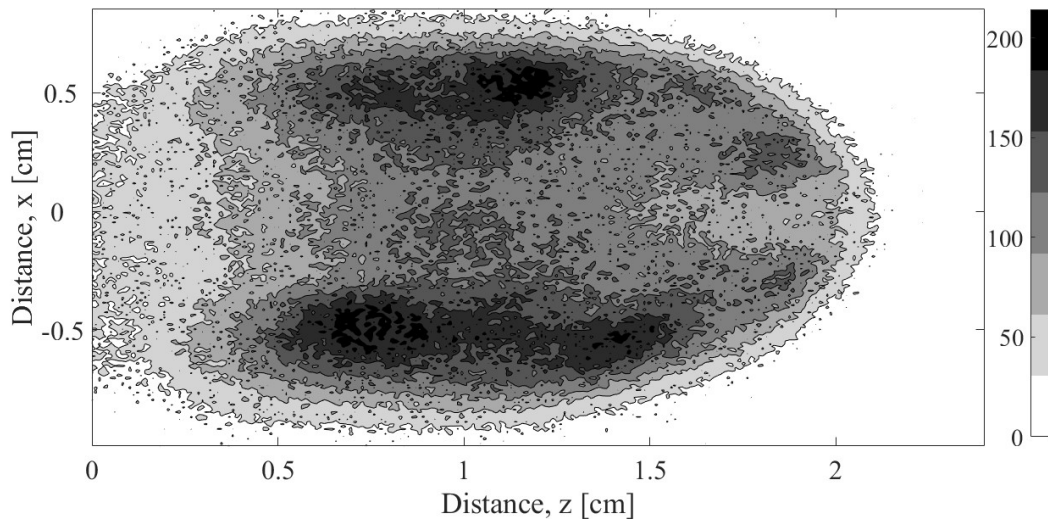


Figure 16. Intensity contours of 224 mJ Al ablation in 500 mTorr Ar at 6.1 μ s delay showing vortices as plume slows.

Filtered ICCD images allow for capturing spectrally resolved images and monitoring the evolution of selected emitters [45], [70]. Spectral data from 300-800 nm was previously recorded using the present apparatus, identifying neutral and singly ionized species [44]. Narrow band pass filters (≤ 10 nm bandwidth) with center wavelengths of 500 nm, 375 nm, 394 nm, and 560 nm were utilized to isolated emission from neutral and singly ionized Ti and Al [44]. Figure 17 illustrates intensities along the centerline of the plume for both Ti and Al ablation detailing the location of the neutral and ionized species. Also shown are the unfiltered, broadband intensities, which decrease for longer delays. The filtered data intensity is lower than the broadband signal, reflecting the narrow spectral bandwidth and the low detector sensitivity at wavelengths below 400 nm. Data in each figure were scaled to the broadband signal with average scaling factors provided in each figure.

At early times, the ion and neutral distributions evolve quite differently. Most striking is the earliest time distributions for Ti in Figure 17(a) where the broadband emission extends much farther from the target than both the neutral and ion images. Because the filters cover a small fraction of the emission particularly for the dense Ti visible spectrum, it is possible that this intensity is due to other excited electronic states [44]. Additionally, a broad-spectrum continuum emission – Bremsstrahlung radiation – is produced via free-free transitions in the plasma and exists for the first 1-2 mm of expansion [15], [57], [62]. At 350 ns (Figure 17(b)), the broadband and Ti I species share a common contact front, but the neutral emission is highest near the target. At times $> 0.5 \mu\text{s}$ (Figure 17(c),(f)), the neutral, ion, and broadband profiles for both Ti and Al share a common spatial distribution. The Al intensity sequence (Figure 17 (d)-(f)) also shows the neutral species (Al I) dwelling at the surface while the ionized species (Al II) peaks at the broadband contact front at earlier delays. At times $> 240 \text{ ns}$, the Al I species appears to have reached the contact front and joined the Al II signal.

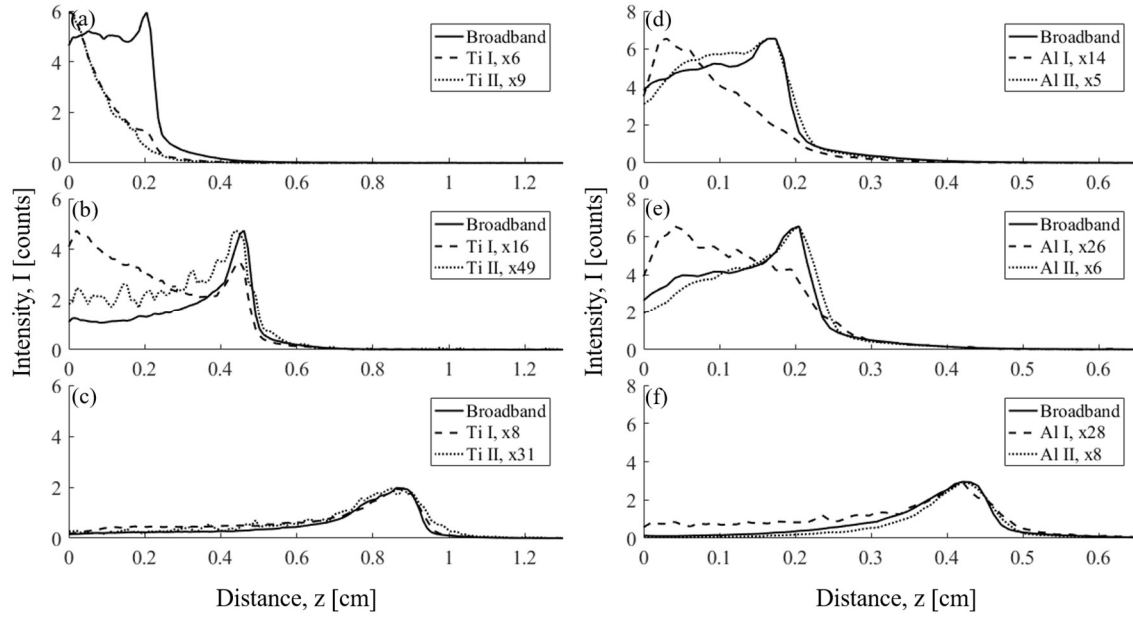


Figure 17. Centerline intensity for 224 mJ 1000 mTorr Ti ablation at (a) 145 ns, (b) 350 ns, and (c) 940 ns and for 224 mJ 1000 mTorr Al ablation at delays of (d) 135 ns, (e) 160 ns, and (f) 390 ns. Solid lines represent broadband signals, dashed lines represent the excited neutral species (Ti I or Al I), and dotted lines represent the excited ionized species (Ti II or Al II).

Filtered imaging intensity data reveal that the ion signal persists longer in ambient pressure than in vacuum. Figure 18 shows that the Ti II signal lasted for $\sim 1 \mu\text{s}$ under expansion into vacuum where no shock front is established. Conversely, the Ti II signal lasted for $>5 \mu\text{s}$ during expansion into 500 mTorr and 1000 mTorr of Ar. The Al II signal showed the same trend but at different delays. There is sufficient kinetic energy in the shock front ($> 100 \text{ eV}$, see discussion below) to produce ionization. The ionization potential for Ti is higher than for Al, possibly explaining the higher Al II signal far from the target at short delays [47]. Optical emission and ion probe studies have observed that ions generally precede the neutral species in the emissive plume [133].

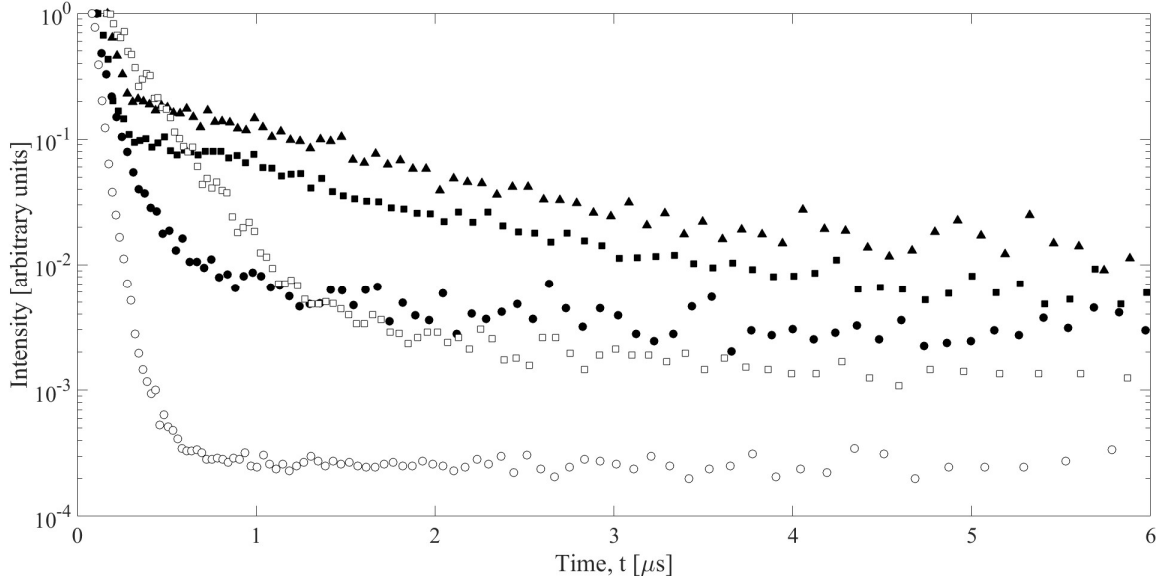


Figure 18. Filtered imaging intensity dependence on time for Ti II in (●) vacuum, (▲) 500 mTorr, and (■) 1000 mTorr and for Al II in (○) vacuum and (□) 1000 mTorr.

The ablated plume shapes are significantly affected by background pressure. Figure 19 shows images of Ti ablation plumes under varying background pressures at 1.1 μs delay. The corresponding intensity profiles along the centerline of the plume in the z -direction are also provided. At vacuum background pressure, a well-established contact front is not observed for either Ti or Al ablation due to the lack of background gas atoms to excite and slow the leading edge of the plume. Strong shock fronts are clearly observed in the higher background pressure cases. Since the radiative rates are rapid, 10^7 - 10^8 s^{-1} , the emission largely occurs in the same pixel that the excitation originated. That is, excited states are not propagated in the z -direction and the emission is produced locally. As pressure increases, more background gas is displaced, a stronger contact front develops and the plume slows.

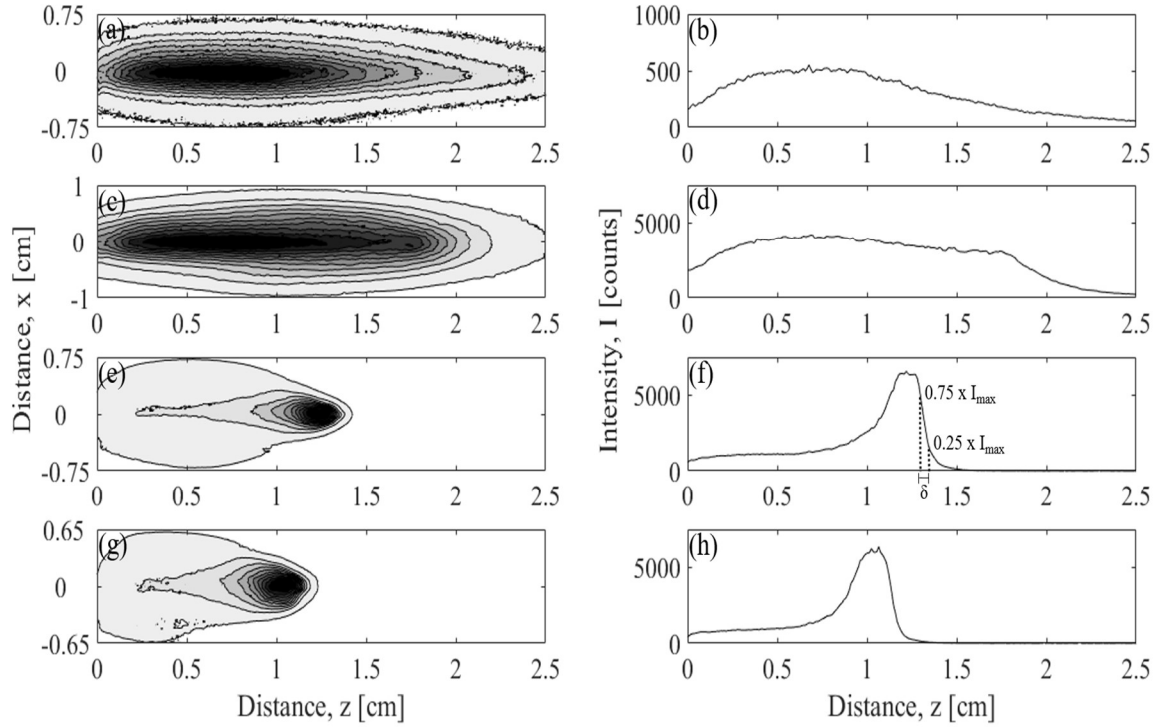


Figure 19. Ti ablation intensity contour images and intensity along the centerline of the plume at 240 mJ/pulse laser energy and Ar pressures of (a-b) vacuum, (c-d) 50 mTorr, (e-f) 500 mTorr, and (g-h) 1 Torr at 1.2 μ s delay. Contact front thickness (δ) is defined as the distance between the 25% and 75% of maximum intensity (I_{\max}) at the plume leading edge.

At 500 mTorr, the thickness of the contact front is $\delta=0.4$ mm, nearly the same as the mean free path. The speed of sound in Ar, v_{Ar} , at 294 K is 319 m/s. The corresponding contact front location, $z=1.3$ cm, for the 1.2 μ s delay established a velocity of 1.08 cm/ μ s or a local Mach number of $M=34$. Figure 19(g)-(h) reveal that the contact front in 1 Torr has slowed to 0.95 cm/ μ s, while the front thickness is approximately the same as 500 mTorr ($\delta=0.5$ mm). At these higher pressure conditions, the plume has suffered sufficient collisions to begin to dissipate the over-pressure and the plume is quickly slowing.

Figure 20 shows the Ti emissive plume dependence on laser energy. The leading edge distance traveled by the plume increases with increasing laser energy. The intensity

of the plume increases by >400% when increasing laser energy by 108 mJ/pulse. The shape of the plume appears to be approximately equivalent.

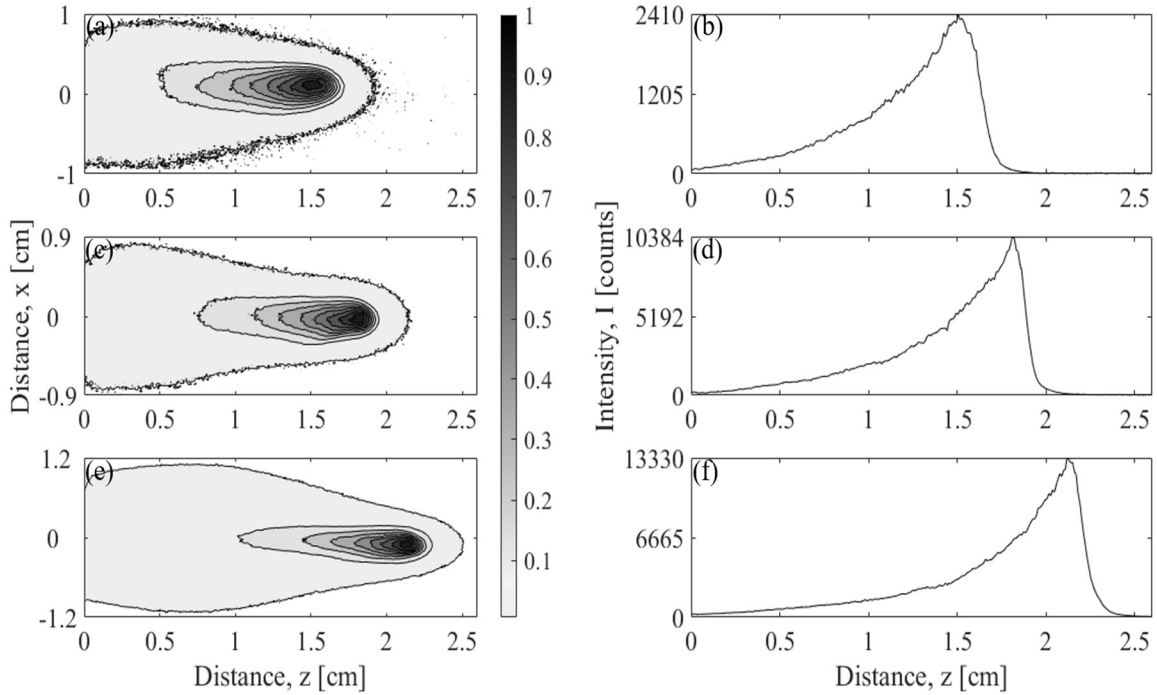


Figure 20. Ti ablation intensity contour images and intensity along the centerline of the plume at 500 mTorr Ar at (a-b) 174 mJ/pulse, (c-d) 224 mJ/pulse, and (e-f) 282 mJ/pulse at 2.8 μ s delay.

4.3.3 Dependence of plume dynamics on pressure and laser energy

The kinetic energy of the expanding plume depends on metal surface, laser energy and background pressure, and can be characterized from the plume imagery. The trajectory of the shock front, $z(t)$, defined by the location of the emissive front at 10% of the maximum intensity, is illustrated during the time when the laser pulse is on in Figure 21 and for a few cases after the laser pulse in Figure 22.

The plume expansion during the laser excitation shown in Figure 21 clearly indicates interaction of the plume with the laser radiation. The plume initially expands in a

manner consistent with the ~ 40 ns temporal energy distribution of the laser pulse. A fit of the linear portion of the trajectory from 10 ns to 30 ns results in a velocity of $5.8 \text{ cm}/\mu\text{s}$. When coupled with the mass loss results from Section 4.3.1, kinetic energies ranging from 0.6-1 J are calculated, 3-4 times the incoming laser energy. Clearly the mass involved in the earliest expansion of the plume, during the laser pulse, is significantly less than the total mass given in Figure 14. That is, the mass ejection rate is highest late in the ablation process and these atoms receive less kinetic energy. Indeed, the free expansion velocity for the full plume is much lower, $\sim 1.6 \text{ cm}/\mu\text{s}$, as discussed below. Laser-plume coupling mechanisms such as inverse-Bremsstrahlung and photoionization are well established in literature [41], [57]. Furthermore, early plume expansion mechanisms have been postulated describing the rapid acceleration of ions due to a coulombic attractive force from electrons that have been accelerated away from the plume [129], [133], [134]. A thorough determination of a laser plume coupling mechanism responsible for the observed laser-plume expansion is beyond the scope of this work, and the experimental findings are simply noted here.

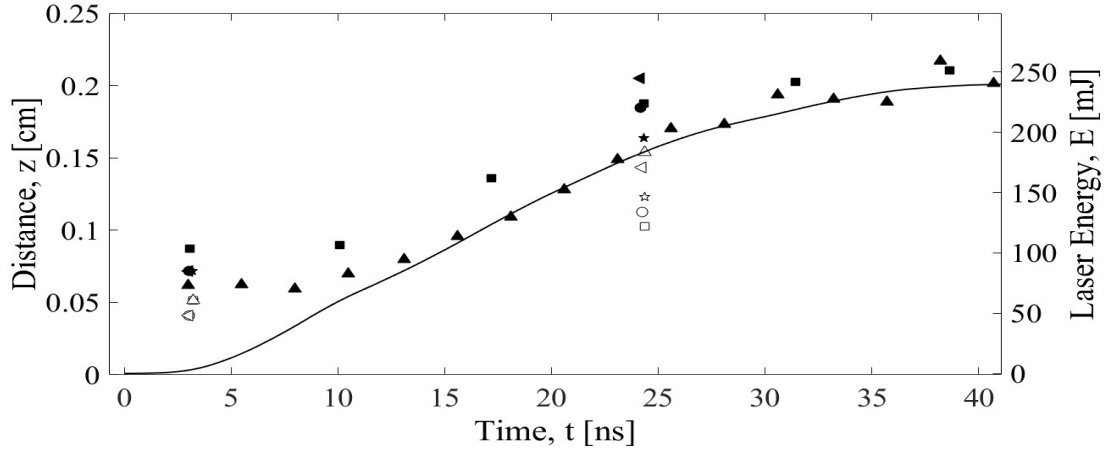


Figure 21. Ti (filled markers) and Al (unfilled markers) plume trajectories reflecting the 240 mJ laser pulse temporal distribution (-) at (●) vacuum, (■) 50 mTorr, (★) 250 mTorr, (▲) 500 mTorr, and (◄) 1000 mTorr Ar.

At the conclusion of the laser pulse, the front expands freely with a velocity, v_o , defined by a linear trajectory (see Region I of Figure 22(a)). The plume begins to slow as the highest velocity components contact the background gas. Under vacuum conditions, the plume intensity is relatively weak, lacks a well-defined contact front, and the front continues to propagate as a free expansion with constant velocity. The mean free path between collisions is 0.2 – 4 mm for pressures of 50 – 1000 mTorr and this contact front between the expanding plume and the background gas quickly becomes apparent. The expanding plume acts as a mechanical piston, compressing the background gas resulting in the formation of a shock front towards the end of this region. Region II marks the trajectory of a well-developed shock front. The shock dynamics can be described by the Sedov Taylor theory [57] during this period when the shock is strong. At longer times (Region III), the emissive plume approaches a stopping distance of 3 cm and separates from the weakened shock which approaches $M=1$. Three approaches to defining the plume energy dynamics are now pursued using free expansion, blast theory, and a drag model.

A free expansion model is adequate for characterizing the ablation data in vacuum throughout the entire expansion (Figure 22(b)). At higher background pressures, a linear trajectory is observed for only the first ~ 200 ns after which collisions begin to slow the plume. The free expansion velocity for Al in Figure 22(a) is $1.81 \pm .07$ cm/ μ s and for Ti in Figure 22(b) of $1.57 \pm .02$ cm/ μ s. These initial free expansion velocities are independent of pressure, varying by $\pm 3\%$ and exhibiting no systematic trends. The free expansion velocities correspond to 61.1 eV per Ti atom and 45.8 eV per Al atom. Considering the mass results from section 4.3.1, the plume kinetic energies range from 46-78 mJ for Ti ablation and 51-69 mJ for Al ablation for Ar pressures ranging from 1-0 Torr. The result that the pressure dependence for total kinetic energy scales directly with the ablated mass, leads to a primary conclusion: the fraction of the incident laser energy coupled to both the target and plume decreases at higher background pressures.

If it is assumed that the available energy above the threshold energy and not observed as kinetic energy is portioned to internal energy, maximum temperatures of ~ 41 eV/atom for Ti and ~ 31 eV/atom for Al can be extracted. The internal energy (electronic excitation) is certainly less, due to incomplete coupling of the laser energy to both the target and plume.

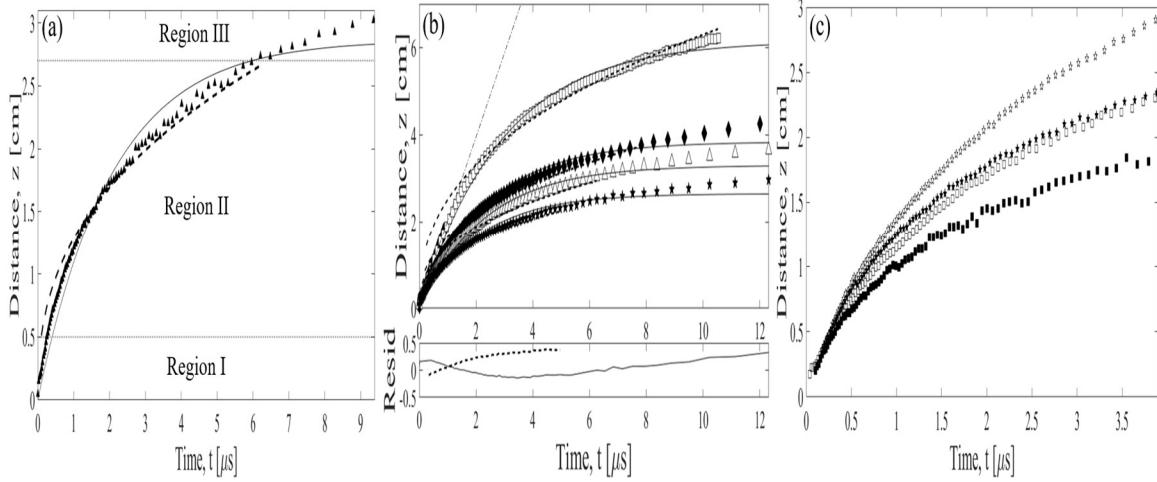


Figure 22. (a) Trajectory of Al plume from 240 mJ/pulse ablation in 500 mTorr Ar. Region I is the trajectory in which free expansion occurs and the shock wave is forming. Region II is the trajectory in which the shock wave is fully formed and Sedov-Taylor theory is applicable. Region III is the trajectory in which the contact front slows and the shock wave moves ahead of the contact front, (b) Ti blast model (--) and drag model (-) fits to broadband signal as a function of background pressure at (●) vacuum, (□) 50 mTorr, (◆) 250 mTorr, (△) 500 mTorr, and (★) 1000 mTorr and a laser energy of 240 mJ/pulse. A linear, free expansion model (-.) fit to the vacuum data is provided for reference and residuals for the 1000 mTorr Sedov-Taylor and drag model fits are provided in the bottom window, and (c) dependence of plume trajectory on laser pulse energy for (■) Al 174 mJ/pulse, (★) Al 282 mJ/pulse, (□) Ti 174 mJ/pulse, and (☆) Ti 282 mJ/pulse at a background pressure of 500 mTorr.

Figure 22(c) indicates that the Al and Ti plumes for 500 mTorr argon background travel nearly the same distances for the first 800 ns for 282 mJ/pulse and for the first 400 ns for 174 mJ/pulse. The plume velocity of both species increases with laser energy. The free expansion velocity increases by 14% for both species as the laser energy increases from 174 to 282 mJ/pulse.

A model based on a classical linear drag force is often used to determine the contact front location at which the expanding plume stops, z_f [15]:

$$z = z_f(1 - e^{-kt}) \quad (22)$$

where the deceleration is characterized with a drag decay constant, k . The drag model also provides another estimate of the initial velocity, $v_{0,D} = kz_f$. A fit of Eq. 22 to the data in Figure 22(a) yields a stopping distance of $z_f = 2.86 \pm 0.04$ cm for Al in 500 mTorr of argon. The dependence of the drag parameters on background pressure and laser energy is further detailed in Figure 23. The initial velocity of the plume increases with increasing laser energy, reflecting the fact that more energy is available to the expanding plume. The initial velocity at the lowest pressure (50 mTorr) for Ti is 2.12 ± 0.04 cm/ μ s, greater than that of the Ti free expansion value in Figure 22. Contrary to the initial velocity dependence determined using the free-expansion model, as the pressure is increased, the velocities of Ti and Al decrease from 1.6 cm/ μ s at 250 mTorr to 1.3 cm/ μ s at 1000 mTorr. One might not expect the initial drag velocity to depend on the background pressure, but instead to be equivalent to the free-expansion values reported earlier. Drag model fitting to emission images is common [15], [71], [121] and in the case of $\text{YBa}_2\text{Cu}_3\text{O}_{7-x}$, also show a decrease in drag fitted initial velocity with increasing background pressure [70]. Based on the experimental trajectory evidence, we prefer the early free expansion fits for estimating the plume initial velocity. Constraining the fit of Eq. 22 using the measured free expansion velocity produces unacceptably large residuals. The drag model fits are heavily weighted for longer times where significant collisions occur and is best suited for estimating stopping distances. The stopping distances, z_f , are larger for Ti on average by 0.5 cm, consistent with the greater Ti momentum. Stopping distance are shorter at higher pressure due to the increase collision frequency. The stopping distances also generally increase with higher laser energy due to the higher initial velocity. An evaluation of the shock energy in Region II of Figure 22(a) using the blast model is now accomplished.

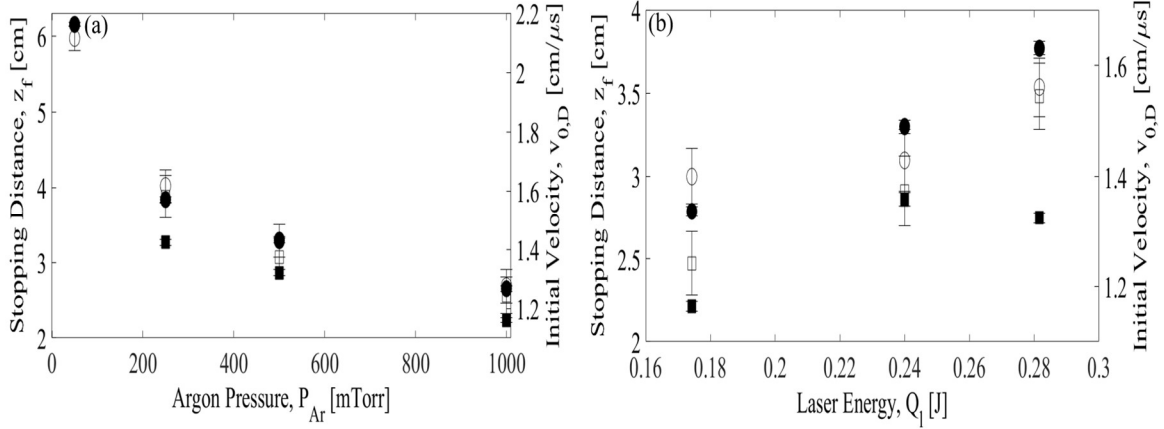


Figure 23. Dependence of stopping distance, z_f , for (●) Ti and (■) Al and dependence of initial velocity, $v_{o,D}$, for (○) Ti and (□) Al on (a) background pressure, P_b , at 240 mJ/pulse and (b) laser energy, Q_l , at 500 mTorr.

The emissive plume front trajectories may be further interpreted through the use of a Sedov-Taylor point blast model. The Sedov-Taylor model (Eq. 23) describes a shock wave produced after an instantaneous point detonation, relating the shock energy, E_{ST} , the background gas density, ρ , the plume dimensionality, n ($n=1$ for planar expansion, $n=2$ for cylindrical, and $n=3$ for spherical), a constant factor dependent on the ratio of specific heats ($\xi = 1.49$ ($n = 1$), $\xi = 1.77$ ($n = 2$), and $\xi = 1.15$ ($n = 3$)), and time, t , to the shock front location at a distance from the target z [57], [135]:

$$z = \xi \left(\frac{E_{ST}}{\rho} \right)^{\frac{1}{n+2}} t^{\frac{2}{n+2}}. \quad (23)$$

This model is relevant when the amount of mass displaced by the expanding shock front is larger than the amount of mass in the expanding shockwave and when the pressure behind the shock front is larger than the pressure of the background gas [57], [136]:

$$z_L = \left(\frac{3m_a}{2\pi\rho}\right)^{\frac{1}{3}} \ll z \ll \left(\frac{2E_a}{P_b}\right)^{\frac{1}{3}} = z_H \quad (24)$$

where m_a is the amount of mass ablated from the surface, ρ is the background gas density, E_a is the initial ablation energy (laser energy), and P_b is the background gas pressure. The lower bound limit is estimated from the ablated mass reported in Section 4.3.1 and is typically 0.3 – 1.4 cm. For the Al 500 mTorr example in Figure 22(a), this limit is achieved for $t > 0.255 \mu\text{s}$. At earlier times, the blast theory unrealistically predicts velocities that exceed the free expansion and become very large at $t=0$. Fits of the blast model are illustrated in Figure 22(b), and do not include data below the lower bounds of 1.4 cm for 50 mTorr, 0.76 cm for 250 mTorr, and 0.5 cm for 500 and 1000 mTorr.

The high limit of Eq. 24 ranges from 14-44 cm, well beyond the observed stopping distances. Apparently, the emissive plume detaches from the shock front propagating in the background gas well before the upper bound. The ICCD images observe the visible emissions only from excited constituents and any non-excited constituents cannot be observed. At atmospheric pressures, the emissive plume exhibits a stopping distance, where shadowgraphy indicates the non-emissive shock front separates from the emissive plume and continues to propagate in accordance with the blast model [31], [116]. Because the location of the shock front as it breaks away from the emissive plume is not observed in this study, the upper bound described in Eq. 24 must be further limited. Harilal et al determined a breakaway time of ~ 400 ns from ablation of Al in argon at atmospheric pressure [31]. This breakaway time is converted to a non-dimensional time according to

$\tau = v_{Ar} \left(\frac{2E_a}{P_b}\right)^{\frac{1}{3}} t$, and used to determine the corresponding limiting times and locations for

the studied laser energy and background pressure conditions. Breakaway locations, z_B , of 6.20, 3.76, 2.99, and 2.30 cm for Ti ablation in 50, 250, 500, and 1000 mTorr argon, respectively, and of 3.03, 2.40, and 1.80 cm for Al ablation in 250, 500, and 1000 mTorr argon, respectively, were determined using this scaling. These calculated values for z_B served as the upper bound for fitting Eq. 23 to the emissive plume trajectories.

Typical fits to the blast and drag models are compared in Figure 22(b). In general, the drag model fits are marginally superior to the blast model for Ti while the blast model fits are superior for Al trajectories. The largest residual root mean square error (RMSE) of 0.185 cm was calculated for 50 mTorr Ti ablation fit with the blast model while the largest RMSE for Al was 0.152 cm for 250 mTorr fit to the drag model. As others have observed, the drag model fit residuals show smaller residuals for lower background pressure [15]. Structure above the noise in the data is present for both the blast and drag fits, indicating systematic problems with both models.

A comparison of the blast fit parameters as functions of laser energy and pressure is observed in Figure 24. Analysis of the optimal plume dimensionality reveals the Ti and Al plume dimensionalities are less than spherical for all pressures, ranging from 1.7 ± 0.1 to 2.9 ± 0.1 . Furthermore, plume dimensionality changes very little with changing fluence, with the Al plume dimensionality higher on average ($n=2.3 \pm 0.1$) than the Ti average plume dimensionality ($n=1.9 \pm 0.1$). Deviations from spherical expansion are likely due in part to the absence of a point source.

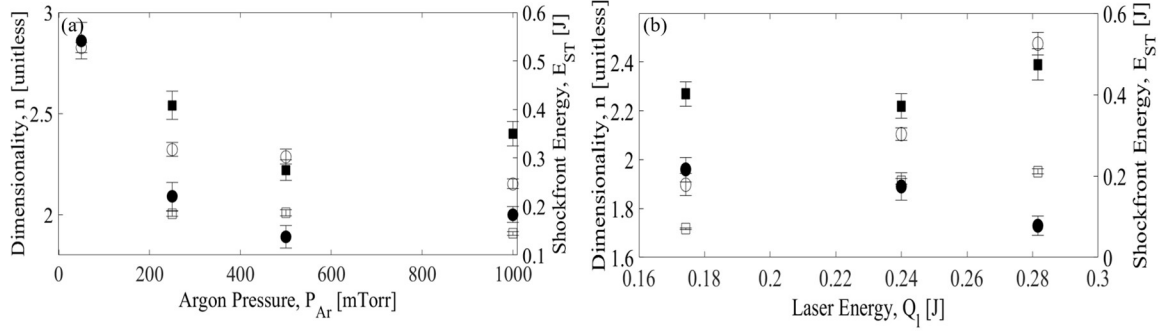


Figure 24. Dependence of plume dimensionality, n , for (●) Ti and (■) Al and dependence of plume front energy, E_{ST} , for (○) Ti and (□) Al on (a) background pressure, P_b , at 240 mJ/pulse and (b) laser energy, Q_l , at 500 mTorr. E_{ST} was determined using $n=3$.

The fits for the shock front energy, E_{ST} , using $n=3$, for Ti at 240 mJ/pulse decrease from 528 ± 10 mJ at 50 mTorr to 247 ± 10 mJ at 1 Torr. Due to the target plane, the laser plume is only a hemispherical expansion whereas the blast theory assumes expansion in both $\pm z$ directions. Therefore the blast theory fit parameter for energy are reduced by a factor of two to characterize the shock energy [137]. The resulting Ti energies from the blast model, $E_{ST}/2$, are 51-100% of the incident laser energy. For aluminum the shock front coupling is somewhat less, 27–38%. If we account for the threshold energies listed in Table 5, the Sedov-Taylor model overestimates the Ti energy in the plume, predicting 120% of the available energy in the shock front for 500 mTorr Ar ablation while Sedov-Taylor estimates $\sim 90\%$ of the available energy in the Al shock front for 1000 mTorr Ar ablation. Conservation of energy does not allow the Sedov-Taylor energy to be above 100% of the available energy.

A powerful concept of self-similarity that comprises the Sedov-Taylor model enables the trajectories to be scaled for comparison between various energies and background pressures using the Sedov-Taylor limits from Eq. 24. Figure 25 shows the

trajectory data from Figure 22(b) scaled using these limits. The similarity between various background pressures is only modest and a single trajectory for all conditions is not achieved. This scaling assumes a constant $n=3$ spherical expansion, but the fits of Figure 24 yield $n < 3$ with a significant dependence on pressure. The different degree of curvature in the trajectories at various pressures reflects this change in expansion dimensionality. Furthermore, the variation in E_{ST} with pressure conflicts with the pressure similarity. The decrease in initial ablation energy released at higher pressure is consistent with the decrease in plume kinetic energy derived from the free expansion velocity and mass measurements and supports the conclusion that laser coupling to both the target and plume decreases at higher pressure.

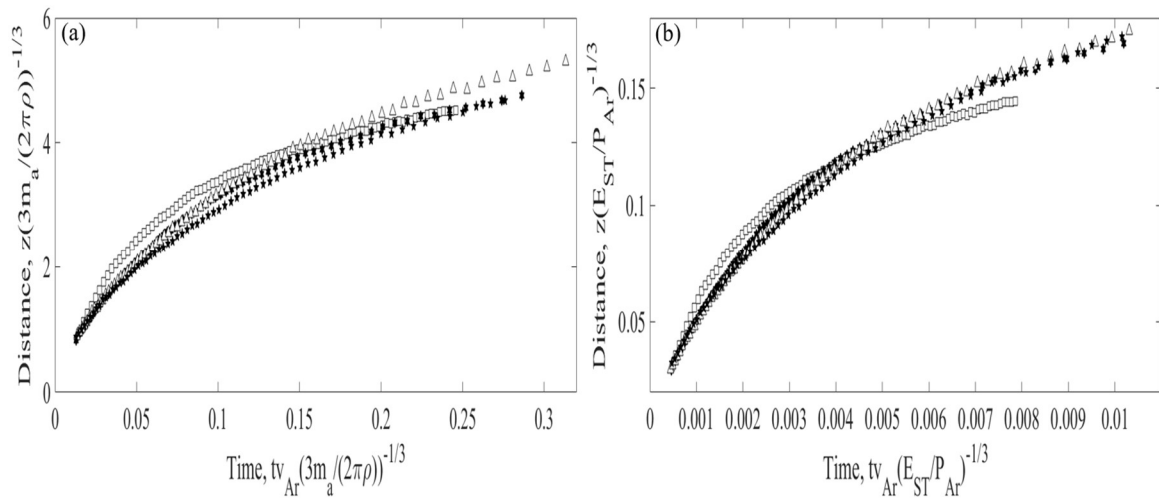


Figure 25. Ti trajectory data for (\square) 50 mTorr, (\star) 250 mTorr, (\triangle) 500 mTorr, and (\bullet) 1000 mTorr and a laser energy of 240 mJ/pulse scaled using (a) the lower limit of Eq. 24, and (b) using the upper limit of Eq. 24.

The overpressure and temperature behind the shock front at a particular plume distance z can be calculated utilizing the results from the Sedov-Taylor model assuming a

spherical expansion ($n=3$) and a constant ratio of specific heats ($\gamma=5/3$ for monoatomic gas), according to

$$p_1 = \frac{2}{\gamma + 1} \xi^5 \left(\frac{2}{5}\right)^2 \frac{E_{ST}}{z^3} \quad (25)$$

$$T_1 = \frac{T_0 \gamma - 1}{p_0 \gamma + 1} \frac{2}{\gamma + 1} \xi^5 \left(\frac{2}{5}\right)^2 \frac{E_{ST}}{z^3} \quad (26)$$

where p_1 is the pressure behind the shock front, p_0 is the ambient pressure, T_1 is the temperature behind the shock front, and T_0 is the ambient temperature. Figure 26 shows that the pressure and temperature are highest at the shortest z distance for which the shock wave has developed and then decrease with increasing z . The highest T_1 and p_1 are shown to correspond to the lowest displayed argon pressure p_0 ($T_1=26$ eV and $p_0=2 \times 10^6$ mTorr) and decrease with increasing background pressure. The temperatures displayed in Figure 26 are less than the internal energy temperatures calculated in Region I.

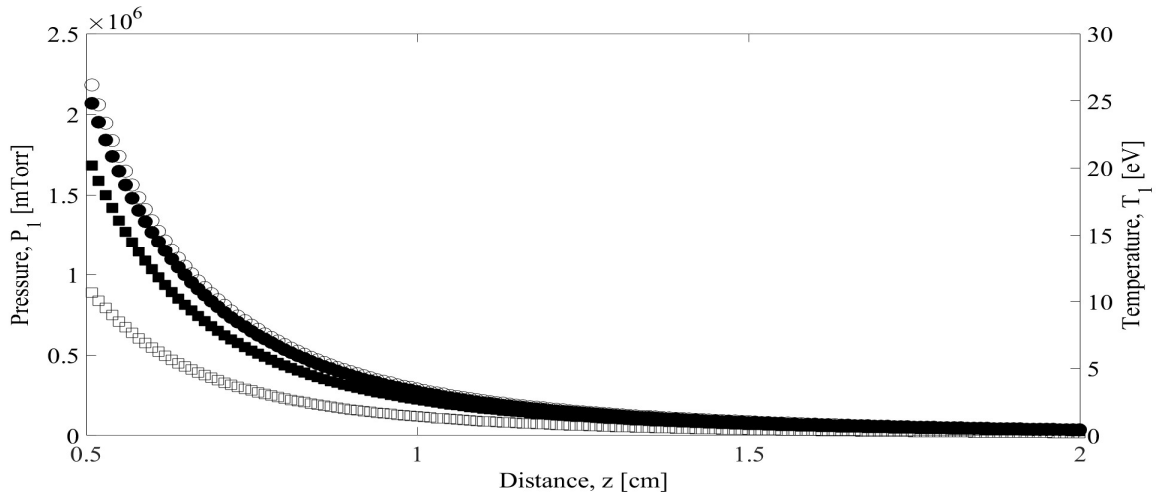


Figure 26. Ti ablation dependence of shock pressure, p_1 , for (●) 500 and (■) 1000 mTorr and temperature, T_1 , for (○) 500 and (□) 1000 mTorr.

The plume expansion energy partitioning may be best summarized by a discussion of the regions labeled in Figure 22(a). Threshold energies determined in Section 4.3.1 reveal that $\leq 48\%$ and $\leq 63\%$ of the original 240 mJ are available to produce and drive the observed Al and Ti ablated plumes, respectively. In Region I after termination of the laser pulse, free expansion velocities yield vacuum kinetic energies of $61 \pm 11\%$ and $52 \pm 12\%$ of the available Al and Ti energy (for the remainder of this discussion, “available energy” will refer to energy above the threshold values given in Section 4.3.1, respectively, with the remaining energy going into the internal energy of the plume. With increasing background pressure, the laser is partially shielded from the target and the plume interacts with the ambient gas through collisions slowing the expansion of the plume and transferring kinetic energy into internal energy, with only $61 \pm 3\%$ and $58 \pm 17\%$ of the available energy going into kinetic energy in 1 Torr of argon for Ti and Al, respectively. As the plume continues to expand, it piles up at the contact front and compresses the background gas further, forming a strong shock wave as Region I transitions to Region II. Application of the Sedov-Taylor blast model to the trajectory in Region II reveals that up to 90% of the available energy goes into the Al shock front. With more accurate locations of the contact front – shock front breakaway, it is likely that nearly all of the available energy is located in the Ti shock front as well. Transition from Region II to Region III is described by a decrease in velocity of the emissive plume due to further collisions with the background gas while the shockwave breaks away and propagates at a higher velocity. We can only observe the emissive plume in this region and so no quantitative measure of the available energy can be made.

4.4 Conclusion

The plume dynamics of Al and Ti under UV, 25 ns ablation at up to 3.5 J/cm^2 have been compared by measuring the mass ablated and imaging the plume dynamics. Mass loss results are consistent with modest ablation thresholds of 90 and 126 mJ/pulse for Ti and Al, respectively. The highly ionized plume partially shields the surface, allowing additional atoms to be ablated at higher laser fluence but shielding the surface more at higher background pressure. The plume kinetic energy is very high, 45-61 eV/atom, corresponding to 10 - 13 laser photons per ablated atom. The Sedov-Taylor point blast model shows laser-shock wave coupling of up to 40% of the incoming energy for Al ablation. The lighter mass aluminum exhibits a slightly higher expansion velocity than Ti but approximately the same initial kinetic energy. The Al plumes also decelerate more quickly due to the lower momentum. Further experimental studies need to be performed to better determine the location of contact front shock front breakaway and to better determine the actual amount of re-deposited material back onto the surface for the conditions present in this paper. The present survey of plume dynamics is necessary for a detailed study of shock strength and shock front instabilities, and for characterizing the evolution of forward directed speed distributions.

V. Laser ablated Ti velocity distribution dynamics

Emissive plumes resulting from pulsed ablation of titanium targets have been observed using a gated ICCD camera to characterize the evolution of velocity distributions as the plume expands into vacuum, Ar and He backgrounds. Shifted Maxwell Boltzmann distributions with flow speeds of $u > 0.1$ cm/ μ s are adequate only for neutral Ti expansion into vacuum. Ionized Ti velocity distribution shows deviation from a conventional shifted Maxwell-Boltzmann distribution. Near the target, the time of flight data clearly indicates several distinct distributions for the neutral Ti, with faster component consistent with the ionized Ti velocity distribution. Expansion into He and Ar are clearly non-Maxwellian, with the highest velocity groups suffering collisions in the shock front. Leading edge velocities decrease more rapidly for Ar, consistent with momentum conservation. Expansion into He maintains the appearance of the vacuum distribution at low velocities but shows a decrease in the leading-edge velocity and an enhancement of the intensity of the highest-velocity groups at farther target distances. Determination of velocity distributions from time of flight data is complicated by translation-to-electronic excitation rates, intraplume collisional dynamics, and non-hydrodynamic conditions.

5.1 Introduction

Pulsed laser deposition is a common method for creating thin films using pulsed UV wavelength lasers in background pressures of 0.1-1.0 Torr [15]. Placement of the substrate in reference to the ablated target is crucial to achieving homogenous films requiring characterization of the evolution of the ablated plume. The plume dynamics of Ti and Al under KrF irradiation in vacuum and Ar background have recently been studied

experimentally, detailing plume trajectories, stopping distances and kinetic energies and applying simple models to determine the energy, pressure, and temperature in the shock front [44], [138]. This discussion is continued by focusing on the velocity distribution of Ti in Ar and He background environments.

Fast emissions imaging has been extensively utilized in the literature to determine the location of the contact and shock front and view hydrodynamic phenomena in the plume expansion such as plume sharpening, plume splitting, and Rayleigh Taylor Instability [31], [71], [119], [121]. Velocity distributions and time-of flight spectra during pulsed ablation are typically observed using electrostatic analyzer [27], [139]–[141], emission sensors [121], [141]–[143], and fast imagery [70], [144]. Fast plume imagery using gated intensified charged coupled devices (ICCD) offer time of flight spectra recorded simultaneously at many target distances with excellent spatial, spectral, and temporal resolution [45]. Velocity distributions from laser induced plumes are typically described by modified Maxwell Boltzmann distributions with a forward directed flow speed, here defined as shifted Maxwell Boltzmann (SMB) distributions [15], [45]. Isentropic supersonic expansion or evolution of Maxwell Boltzmann distribution into a SMB due to Knudsen layer effects have been described to explain these distributions [74], [75], [78]. However, application of SMB distributions to expanding plumes of $\text{YBa}_2\text{Cu}_3\text{O}_{7-x}$ have revealed non-physical parameters such as negative flow speeds [45]. Others have noticed that application of SMB distribution to Cu time-of-flight (TOF) data revealed angle dependent fit parameters, requiring further modification of the SMB distribution to include transverse and longitudinal temperatures [46]. Zhiglei et al used molecular dynamics simulations to determine that the physical depth of the particle from

within the target surface directly influenced the distribution observed and they proposed an analytical modified Maxwell-Boltzmann distribution that accounted for a range of flow speeds [145]. Their distribution showed good results with their simulated data but expansion into a background gas would likely change the distribution. Pulsed ablation of Ti targets is less studied [120], [138], with velocity distributions in vacuum examined by electrostatic analyzer [39], [146] and optical emission spectroscopy [36], [109]. In the present work, the gated ICCD technique is applied to experimentally investigate the spatially evolving plume velocity distribution function of Ti in vacuum and various Ar and He pressures.

5.2 Experiment

Details of the experiment have been reported previously [44]. Briefly, a Lambda Physik LPX 305 KrF laser at $\lambda=248$ nm delivered up to 282 mJ/pulse on the target in an 8 x 1 mm rectangular spot with a repetition rate of 1 Hz. The plume propagates normal to the target in the z -direction and the gated camera observes the plume from above, integrating along the y -direction. The pulse exhibits a FWHM of 25 ns and a rise time of 5 ns, yielding a maximum intensity of 141 MW/cm². The laser beam is focused onto the target inside the 10" vacuum chamber through a 300 mm focal length plano-convex fused silica 2" lens at an angle of incidence of ~ 45 degrees to the target normal. The chamber was evacuated to a base pressure of 10^{-6} Torr before being filled with the desired pressure of 99.999% Ar or 99.999% He (250, 500, and 1000 mTorr). The Kurt Lesker $\sim 99.7\%$ Ti 1" diameter by 0.25" thick sputtering targets were mounted onto a 10 rpm rotating carousel

during laser irradiation to reduce significant surface etching. Images contain <5% pulse-to-pulse laser flicker and ≤ 10 ns pulse-to-pulse laser timing jitter.

Fast visible emissions images were captured utilizing a Princeton Instruments PIMAX I intensified charged-coupled device (ICCD). The 512 x 512 array PIMAX I was equipped to image early delays and short plume distance emissions with a Nikon AF Nikkor 60 mm micro f/2.8 lens that provided a field of view (FOV) of 5.24 x 5.24 cm (0.102 mm per pixel). The point spread function is 0.5 mm. The camera was gated with integration times ranging from 2-100 ns and delays of up to ~ 12 μ s after the onset of irradiation. Both the widths and delays were varied nonlinearly over 100 shots and the laser electronics were utilized to trigger the camera. For the initial plume speeds of ~ 2 cm/ μ s presented below, the 2 ns integration time implies a 40 μ m or 0.39 pixel motion during image capture. The PIMAX camera quantum efficiency is above 20% from 410-890 nm, with a maximum quantum efficiency of $\sim 40\%$ at approximately 700 nm. Narrow band pass filters ($\Delta\lambda \leq 11$ nm) centered at 502 nm and 376 nm were employed to isolate the emission from neutral and singly ionized Ti. Optical emission spectroscopy performed on expanding Ti plumes verified that the 376 nm filter isolated the Ti II z^2F^0 - a^2F transitions (375.9 and 376.1 nm) and the y^2D^0 - b^2D^2 transition (374.2 nm), and the 502 nm filter isolated the following Ti I emissions: y^5G^0 - a^5F (498.2, 499.1, 499.95, 501.4, 501.6 nm), z^3d^0 - a^3F (500.96 and 506.5 nm), and w^3G^0 - b^3F (503.6, 503.8, and 507.1 nm) [44], [72]. The broadband emissions include many transitions, with the dominant lines exhibiting radiative rates of $\geq 7 \times 10^7$ s⁻¹. Plume motion during a radiative lifetime for the faster emitters is ≤ 0.3 mm, resulting in the conclusion that emission is produced locally (within 3 pixels).

Ti ablation for typical thin film deposition conditions has recently been described in detail [138]. Ti ablation threshold of $1.12 \pm 0.34 \text{ J/cm}^2$ at laser wavelength 248 nm was determined. The mass removed is $< 8 \text{ } \mu\text{g/pulse}$ corresponding to $\sim 35\text{-}100$ laser photons per ablated atom. Plume kinetic energies as high as 175 eV are observed with stopping distances of 2-6 cm at Ar background pressure of up to 1 Torr.

5.3 Results and Discussion

5.3.1 Velocity Distributions from Emission Images

The intensity observed from excited state emissions is proportional to the number of emitters:

$$I = D(\nu_{ij})h\nu_{ij}A_{ij}n_i l \left(\frac{\Omega}{4\pi} \right) \quad (27)$$

where A_{ij} is the Einstein A coefficient (s^{-1}), n_i is the concentration of the species of interest in the upper state i , l is the optical path length (cm), and ν_{ij} is the frequency of a species transition from upper state i to lower state j . The solid angle viewed by the detection system, Ω , and the spectral detectivity, D , yield intensity on the ICCD camera. The intensity is temporally averaged over a short integration time, $< 100 \text{ ns}$, and may be spectrally filtered to limit emission to specific excited state. Eq. 27 assumes an optically thin plume. Electronically excited Ti states are produced by collisional excitation (translation-to-electronic (T-E) energy transfer) both in the shock front upon collision with the background gas and interior to the plume by collision with other ablated material. At these modest pressures, the decay is dominated by radiative processes:

$$\frac{dn_i}{dt} = k_{ji}n_jm - \sum_k A_{ik}n_i = 0 \quad (28)$$

where n_j and m are the densities of the species of interest in the pre-collision energy state and the colliding partner, respectively. The reaction rate coefficient k_{ji} is equal to the product of the velocity dependent collision cross-section and the relative velocity of the collision partners, $\sigma_{ji}(v_r)v_r$. Here we assume steady state as the Ti major emitters have radiative rates of $\geq 1 \times 10^7 \text{ s}^{-1}$ and most emission is produced locally [72]. Combining Eqs. (27) and (28) shows that the intensity is proportional to the velocity distribution:

$$I(v) = C \sigma_{ji}(v_r)v_r n_{j,0} f(v_j) m \quad (29)$$

where C represents the constants, $f(v_j)$ is the velocity distribution function, and $n_{j,0}$ is the total Ti ground state density.

The T-E cross section, $\sigma_{ji}(v_r)$, has a threshold energy equivalent to that of the electronic excitation of the Ti species $\sim 2 \text{ eV}$ [44]. Above threshold, the cross-section likely decreases proportionally to v_r^{-q} , where q is unknown. The velocity distribution for the background gas is narrow and slow, so that the relative velocity for colliding particles from the expanding plume and the background gas are nearly those of the expanding plume particles ($\sim 10^0 \text{ cm}/\mu\text{s}$ [138]). Excitation in the contact front occurs when the highest velocity group in the plume encounters the background gas. When the shock front is well developed, its thickness is reduced to a few mean free paths. The mean free path is defined by the density of the background gas and is rather long, $\sim 10^2 \text{ um}$ at $\sim 10^0 \text{ Torr}$. In contrast, the pressure behind the shock front is much higher, the mean free path is dramatically reduced, and the collision frequency is significantly increased. The relative speed for

collisions in the interior of the plume is less, as most of the flow is forward directed. If the excitation rate $k_{ji} = \sigma_{ji}(v_r)v_r$ is assumed to be independent of velocity (equivalent to assuming a hard-sphere cross section with no threshold and $q=0$), then the properly normalized intensity represents the velocity distribution. Otherwise, the observed intensities are influenced by both the velocity distribution and the excitation rate.

TOF spectra are created by recording the intensity at a point along the centerline for frames taken at increasing time delays (centerline is defined here to be the average of the center 5 pixels for broadband and Ti I emissions and the center 21 pixels for Ti II emissions to account for low intensity and eliminate any pulse to pulse variation and turbulent front phenomena) (see Figure 27). Exposure times are typically increased at longer plume propagation times and the intensities are normalized accordingly. By knowing the distance of the detector pixel from the target, z , and the timing delay from each frame, t , a velocity (forward directed speed) can be determined, $v=z/t$. This transformation is accurate for the contact front, where the plume is encountering its first collision with the background gas. In the interior of the plume the slowed products after the initial interaction with the background gas are rapidly relaxed to a new distribution. To convert the observed images at various delays, $I(x,z;t)$, to intensity along the centerline ($x=0$) as a function of velocity at various target distances, $I(v=z/t, z)$, requires multiple images. The velocity distribution must account for the non-linear relationship for changes in velocity and time, $dv = \left(\frac{z}{t^2}\right) dt = \left(\frac{v^2}{z}\right) dt$ so that $I(v; z) = I(z; t) \frac{z}{v^2}$. The v^{-2} transformation weights intensity data at low velocity (long time) relatively high.

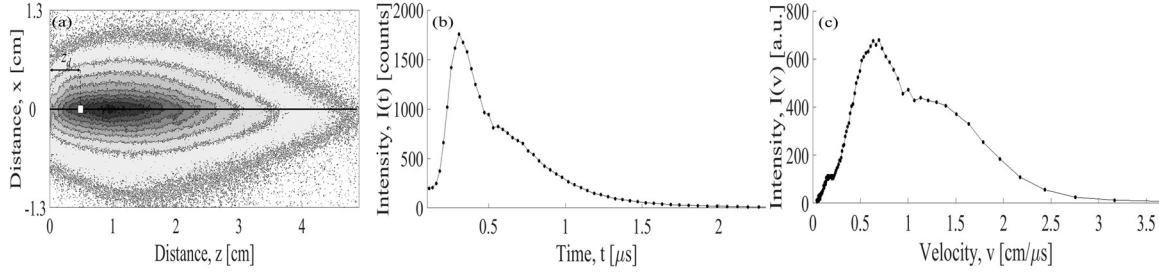


Figure 27. (a) 240 mJ Ti ablation into vacuum intensity contours for time delay of 1630 ns where z_d is the “detector” pixel location at 0.49 cm, (b) the corresponding time distribution formed by recording the intensity at a particular z for a series of spectra or times, and (c) the corresponding velocity distribution.

The advantage to the imaging TOF approach versus a typical TOF setup by monitoring particle flux is that every pixel in the frame can be used as a detector location. Thus, we can simultaneously monitor the velocity distribution at different spatial locations. Furthermore, this technique is passive so as not to disturb the plume expansion. While fast emissions imaging has its advantages, one clear disadvantage is the inability to observe particles that are not excited. Geohegan et al utilized absorption spectroscopy to show that non-excited plume constituents from UV ablation of $\text{YBa}_2\text{Cu}_3\text{O}_{7-x}$ show an additional slower velocity distribution than the excited particles [143].

5.3.2. Velocity Distribution in Vacuum

Ti velocity distributions were constructed at various detector locations in vacuum as shown in Figure 28. Observed emissions in vacuum can only be attributed to intraplume collisions due to a lack of background gas and the fact that emissions occur in approximately the same geographic location in which they are created. At $z=0.31$ cm, the observed distribution appears to be comprised of three components described by most probable velocities of ~ 1 , ~ 0.5 , and 0.1 cm/ μs , respectively, with the middle distribution showing the highest relative intensity. The intensity of the entire distribution decreases

with increasing detector distance z , and can be attributed primarily to the decreasing intraplume pressure as the plume propagates. The fast distribution intensity decreases more rapidly than the two slower distributions with increasing distance from the target due to decreasing density at the leading edge of the plume. The fast distribution becomes difficult to discern at $z > 0.82$ cm. The most probable velocity of the middle distribution increases to ~ 1.1 cm/ μ s at 1.43 cm and the slowest distribution increases to ~ 0.8 cm/ μ s at 2.87 cm. This apparent acceleration phenomenon is discussed further below.

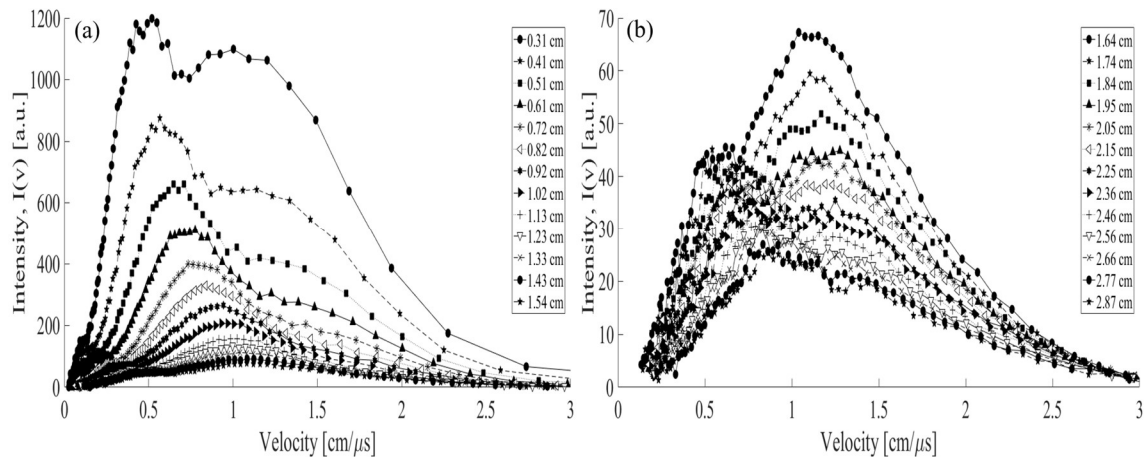


Figure 28. Broadband Ti velocity distribution from 240 mJ ablation in vacuum at various distances, z , from the target.

Singly ionized Ti (Ti II) and neutral Ti (Ti I) excited species are observed in emissive plumes from Ti ablation under these experimental conditions [138]. It has been shown that 61 eV/atom kinetic energy exists in Ti ablated plumes, significantly higher than electronic excitation associated with the observed Ti emissions (~ 2 -5 eV) or the ionization potential (6.83 eV) [72]. Narrow bandpass filters were utilized to limit the emissions to Ti I and Ti II species revealing that the multimode broadband signal can be attributed to

distinct Ti I and Ti II distributions (Figure 29). Further analysis of the vacuum filtered emissions imaging revealed that Ti I is comprised of three distributions while Ti II is comprised of only a single distribution. Here for ease of discussion, we define the Ti I slow, medium, and fast distributions as 1, 2, and 3, respectively. Multicomponent velocity distributions have been observed for expanding plumes from KrF ablation of $\text{YBa}_2\text{C}_3\text{O}_7$ in vacuum and KrF ablation of Si_3N_4 in vacuum [142], [147]. Furthermore, investigation of Ti II from KrF ablation of Ti showed a single distribution only, in agreement with the work here [146]. Distinct velocity distributions likely indicate the existence of multiple ablation mechanisms. Kelly et al have theorized that combinations of vaporization, phase explosion and/or coulombic attraction from escaping electrons might lead to the appearance of particles with distinct speed distributions [148].

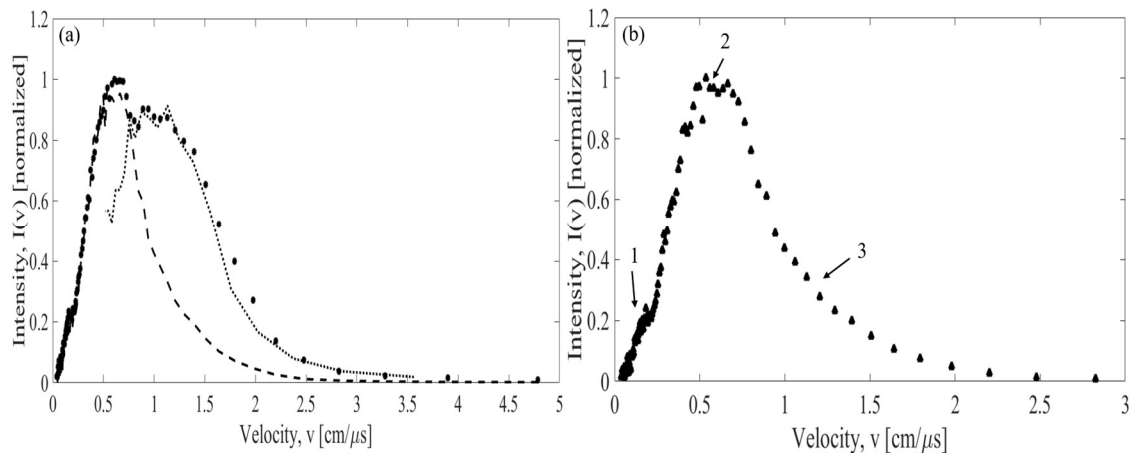


Figure 29. Velocity distribution of 224 mJ Ti ablation in vacuum at a distance, z , of 0.38 cm from the target (a) showing the (●) broadband signal comprised of the Ti I (--) and Ti II (.) data and (b) the Ti I signal defining the multimode distributions for reference.

Shifted Maxwell Boltzmann (SMB) distributions were fit to the Ti I and Ti II intensities:

$$f(v) dv = Av^n e^{-\frac{m(v-u)^2}{2k_b T}} dv \quad (30)$$

where u is the forward directed flow speed in the +z direction (note a 1D flow has been assumed due to the selection of distances from the target along the centerline), T is a temperature parameter describing the width of the distribution (range of forward directed speeds), A is a collection of constants, and n typically equal to three [15], [45], [76]. The best fit criterion was based upon a comparison of the SMB fit root mean square error averaged over various TOF spectra fits or averaged RMSE (aRMSE). There is some discrepancy regarding the velocity exponent n from Eq. 30, with values ranging from $n=-2$ to 4 being reported in the literature [45], possibly reflecting the velocity dependence of the excitation rates. The importance of comparing multiple TOF spectra in making a determination of distribution parameters to ensure a comprehensive analysis is emphasized. TOF data obtained from ICCD images contains an inherent advantage in compiling this data over typical non-array (point detector) TOF methods. Intensity data for Ti II became poor after 1.02 cm, limiting Ti II analysis to distances closer to the target. Ti II fitting was performed for integer values of n ranging from -2 to 4. Unconstrained fitting resulted in physically impossible (negative) flow velocities obtained for Ti II fits with $n > 2$ and flow speeds of $u > 1 \times 10^4$ m/s for $n = -2, -1, 0,$ and 1. The apparent discrepancy for the Ti II distribution between a theoretical SMB with $n = 3$ is not fully understood but the results might indicate that the reaction rate coefficient k_{ji} has an inverse dependence on the velocity as discussed above.

Due to the overlapping of the three Ti I distributions, application of a combined triple SMB fit to the data was difficult. At close distances to the target (<0.7 cm), the Ti I

distribution 1 intensity is insignificant and the Ti I distribution 3 is significant, whereas at long distances (>1.02 cm) the opposite is true. Thus, a more manageable two modal SMB distribution is fit to the data in these limiting regions. Similar to the Ti II, SMB fits were performed for integer values of n ranging from 0 to 6 and negative u values were obtained for $n > 3$. Ti I distribution 3 was difficult to fit with a SMB distribution of any n . Ti I distribution 3 and Ti II distribution exist at similar velocity groups.

Figure 30 displays the results for Ti I distribution 1 and Ti II aRMSE and flow speed as a function of SMB exponent. The u error bounds reflect the 2σ uncertainty in the corresponding fit parameter and the aRMSE error is the standard deviation of the averaged RMSE values. Average RMSEs for both Ti I and Ti II fits show nearly constant errors for fits across all n values. Increasing Ti II n from -2 to 1 results in a decrease in flow speed of 60% yet a change in aRMSE of less than 1%. Similar results are observed for changes in Ti I n . Martin et al analyzed Ti II TOF data obtained from absorption spectroscopy of KrF irradiated Ti in vacuum and obtained flow speeds for fits to a single theoretical SMB ($n=3$) that ranged from -0.81 to 0.58 cm/ μ s [146]. Because of the seemingly unphysical values, he concluded that Ti II distribution should be described by a Maxwell-Boltzmann velocity distribution with $u=0$. Furthermore, Maul et al have experimentally observed both theoretical and non-theoretical SMB components to multimode velocity distribution from UV ablation of gadolinium in vacuum [140]. Because varying combinations of u and n result in similar aRMSE values, a unique determination of the nature of the velocity

distribution

is

difficult.

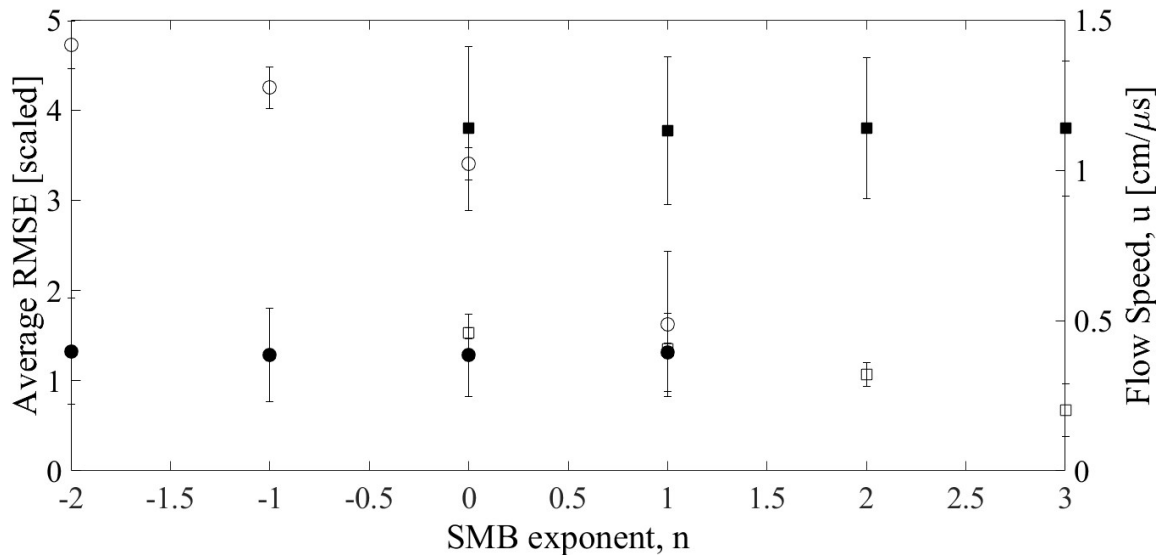


Figure 30. Dependence of Ti I distribution 1 (■) average RMSE x10 and (□) flow speed, u , and Ti II (●) average RMSE x11 and (○) flow speed, u , on SMB exponent n .

Ti I and Ti II fit parameters are now compared in Figure 31 for best fits of select n . A Ti II SMB distribution with $n=0$ is selected because it contains the lowest value of the aRMSE and SMB distributions with $n=3$ for Ti I distributions 1 and 2 are chosen to be consistent with theoretical ($n=3$) SMB distributions. Unconstrained fits of Ti I distribution 2 and 3 at <0.7 cm resulted in negative flow speeds for the Ti I distribution 2, in contrast to the positive flow speed observed for distribution 2 at longer distances. Because of this discrepancy, Ti I distribution 2 and 3 fit parameters at <0.7 cm were obtained through an assumption of a constant Ti I distribution 2 flow speed – 0.18 cm/ μ s – equal to the average of the flow speed values from distributions 1 and 2 in the region where both were statistically equivalent (0.8 to 1.02 cm) and relatively constant.

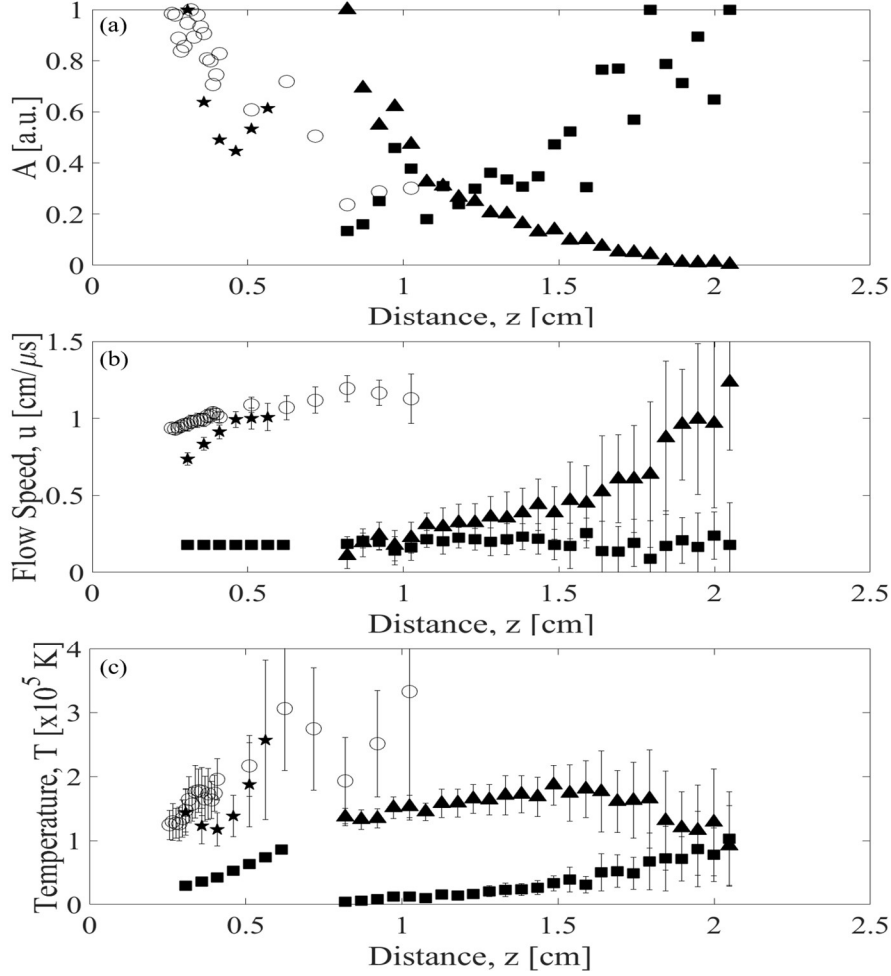


Figure 31. 224 mJ Ti ablation in vacuum showing SMB (a) A vs distance, (b) flow speed vs distance, and (c) temperature vs distance for $n=0$ (○) Ti II and (★) Ti distribution 3 and $n=3$ for (■) distribution 1 and (▲) distribution 2. Error bounds are 2σ .

In Figure 31(a), the Ti II and Ti I distribution 3 intensities decrease quickly at locations close to the target. The Ti I distribution 2 intensity decreases while the Ti I distribution 1 intensity correspondingly increases until ~ 1.3 cm. After 1.3 cm, Ti I distribution 2 begins to disappear. Flow speeds for Ti I increase over a range from 0.1 to 1.2 cm/ μ s, reflecting kinetic energies of up to 36 eV. From 0.82 cm to 1.02 cm, the Ti I distributions 1 and 2 have nearly equivalent flow speeds of on average 0.18 cm/ μ s. At distances >1.5 cm, the error bars on the Ti I distribution 2 flow speed increase to $>100\%$,

reflecting the inability to uniquely resolve this distribution well as it disappears. The Ti I distribution 3 and Ti II flow speeds are significantly higher than those of the two slow Ti I distributions ranging from 0.9 to 1.1 cm/ μ s. The fit temperatures are large, $T = 0.05 - 3 \times 10^5$ K or 0.4 – 26 eV. These temperatures reflect the width of the distribution and the range of forward directed speeds. The widths of these distributions are comparable with the average values. The temperatures of the Ti I distributions 1 and 2 increase mildly, with the temperature of the Ti I distribution 2 consistently greater than that of the Ti I distribution 1 by approximately 1.4×10^5 K until the point at which the Ti I distribution 2 begins to disappear (~ 1.3 cm). Ti II and Ti I distribution 3 display temperatures of $\sim 1.5 \times 10^5$ at 0.31 cm and appear to increase similarly with distance despite large error bounds on both with increasing distance. The Ti II temperature appears to be above that of the Ti I distribution 1 and distribution 2 despite the large error bars in the explicit region of data overlap (>0.8 cm).

The similarity of the Ti I distribution 3 and the Ti II distribution suggests that the species may be produced by a common mechanism. Ions may be created early in the laser pulse due to multi-photon ionization, thermionic emission, and/or photoelectric effect of the surface or with the early expanding plume [56]. Additionally, sufficient energy exists in the leading edge of the plume (~ 60 eV/atom) to ionize Ti by collisional impact with an existing background gas [138]. Ions created from laser interaction with early ablated neutrals would likely result in similar velocity distributions between the ions and parent neutrals. Free electrons that have obtained high kinetic energies due to laser absorption expand out of the plume, possibly accelerating ions via coulombic attraction to high velocities [134]. Neutrals may be produced via recombination of the ions, resulting in

distributions that are likely similar to those of the ions. Material ejected later in the pulse may be produced by a different mechanism, is less ionized, and has less opportunity to be further excited once produced.

Four TOF distributions from Figure 28 and the corresponding trimodal-SMB fits from Eq. 30 are provided in Figure 32. The fits in Figure 32(a) are constrained with $u=1.0 \times 10^3$ m/s and $n=3$ for all three distributions. These fits adequately represent the data with an aRSME of 8.44×10^{-10} . All three temperature parameters increase as the plume propagates, with Ti distribution 1 varying from $T = 1,412 - 14,820$ K as z increases from 0.41 – 1.02 cm. Thus, the apparent acceleration in Figure 31 is not required to adequately characterize the data and is unphysical. Furthermore a flow speed $u=0$ also provides an adequate fit, as seen in Figure 32(b). The $u=0$ distribution is nearly indistinguishable from the $u=1.0 \times 10^3$ m/s, but requires a higher Ti distribution 1 temperature, $T = 3,642 - 19,585$ K for $z = 0.41-1.02$ cm. The SMB fit parameters are clearly not unique.

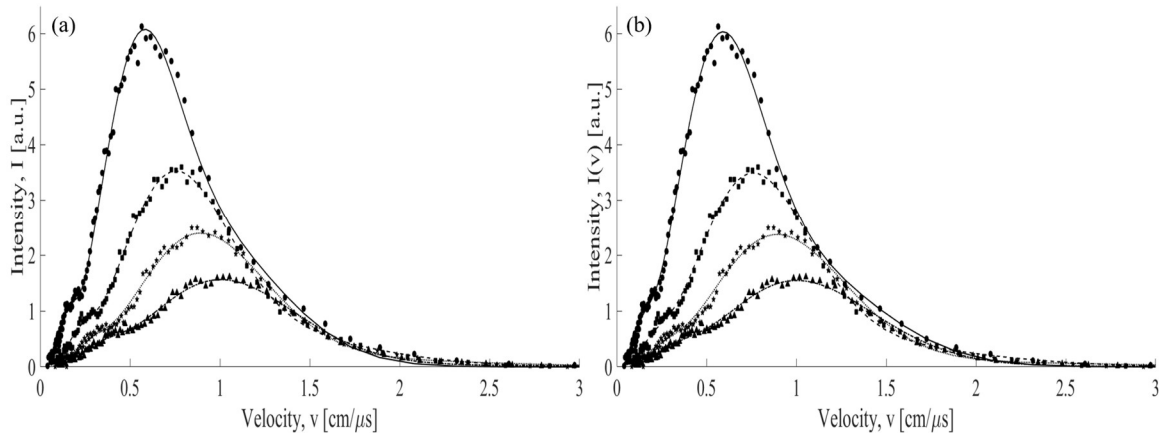


Figure 32. Ti I TOF data and combined SMB distribution fits for distance $z =$ (●) 0.41 cm, (■) 0.61 cm, (★) 0.82 cm, and (▲) 1.02 cm. All three SMB fits utilized $n=3$ and (a) $u=1 \times 10^3$ m/s and (b) $u=0$ m/s.

5.3.3. Pressure Dependent Velocity Distribution

Velocity distributions in various pressures of Ar and He were obtained and prepared in the same manner as in the vacuum case. Figure 33 displays Ti expansion in 1000 mTorr Ar and He. The plume distributions in He and Ar are dramatically different, decidedly non-Maxwellian, multi-modal, and lead to the key results of the present study.

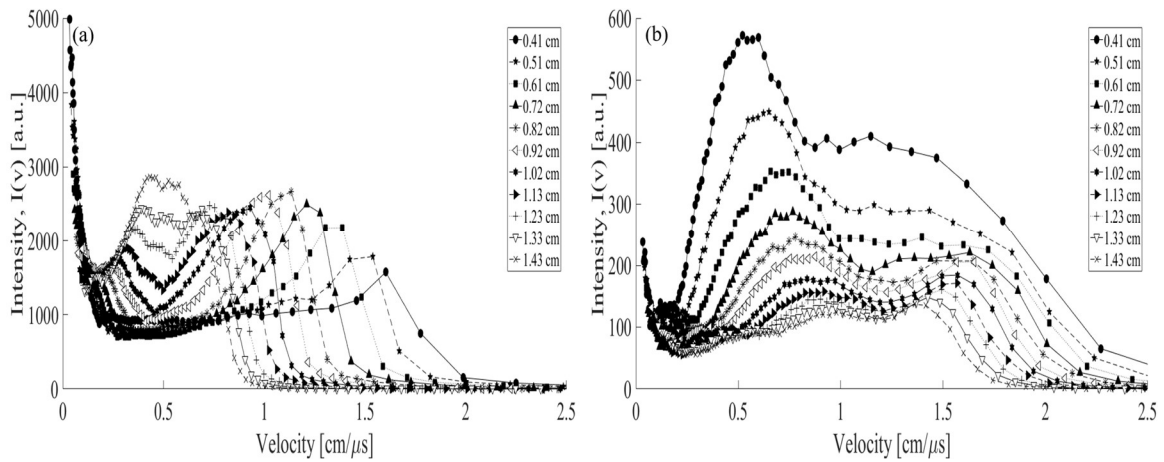


Figure 33. Broadband velocity distributions at different z locations from 240 mJ Ti ablation in (a) 1000 mTorr Ar and (b) 1000 mTorr He.

For Ti expansion in Ar (Figure 33(a)), the peak intensity near the leading edge for $z=0.41$ cm is observed at ~ 1.6 cm/ μ s, quite similar to the previously observed free expansion velocity of 1.57 cm/ μ s [138]. Near the target, the intensity declines rather slowly towards low velocities until increasing at thermal speeds and is clearly non-Maxwellian. Low intensity TOF data at long delays result in fictitiously large intensities of low velocity components due to the $I(v; z)$ conversion. The intensity of the leading edge of the distribution (> 1.6 cm/ μ s) abruptly falls to zero at ~ 2 cm/ μ s in a manner inconsistent with a SMB distribution. As the distance from the target, z , is increased, the leading-edge

velocity, v_{LE} , decreases and the intensity from 0.2 - 0.5 cm/ μ s begins to increase. At $z = 1.33$ cm, the intensity of the peak forming from 0.2 - 0.5 cm/ μ s is equivalent to that of the intensity in the fast distribution and the fast distribution has decreased in velocity enough to form essentially one low velocity distribution.

Ti expansion into He yields far different results than in Ar (Figure 33(b)). At $z = 0.41$ cm, the Ti velocity distribution displays fast and slow distributions described by most probable velocities of ~ 0.6 and ~ 1.2 cm/ μ s. The slow distribution has a higher intensity than that of the fast distribution. As the distance from the target is increased, the intensity of the entire distribution decreases. The most probable velocity of the slow distribution appears to increase to ~ 1 cm/ μ s as the distance from the target increases to 1.43 cm. The leading-edge velocity of the entire distribution decreases gradually with increasing distance from the target with a velocity of ~ 1.6 cm/ μ s at $z = 1.43$ cm. As the leading-edge velocity decreases, the intensity near the leading edge begins to build. The fast distribution decreases in intensity and then ceases to be distinguishable from the increased leading-edge intensity at $z = 0.72$ cm.

The key features from the Ti distribution expansion into vacuum in Figure 28 cannot be distinguished in the distribution of Ti expansion in Ar in Figure 33(a). Instead, Ti expansion into Ar shows a sharp reduction in the leading-edge velocity, an increase in the intensity with increasing z , and an enhancement of slow-velocity components of the distribution with increase z . Comparatively, expansion into He in Figure 33(b) shows many of the key features of the vacuum distribution, initially displaying a distribution almost identical to that of the early Ti vacuum distribution with the exception of a clear low

velocity component similar to the Ti I distribution 1. As z increases, He maintains the appearance of the vacuum distribution at low velocities but shows a decrease in the leading-edge velocity and an enhancement of the intensity of the highest-velocity groups. Ti velocity distribution for expansion into Ar and He is not indicative of a SMB, with expansion into Ar showing most significant deviation from SMB.

To further assess the differences in the distributions into He and Ar, we now examine the rate of plume slowing. Figure 34 displays the velocity corresponding to the 50% intensity maximum on the leading edge of the distribution, v_{LE} , at different detector distances for various pressures of Ar and He. The rate at which v_{LE} decreases with distance is greater at higher background pressures, due to the greater collision frequency. The v_{LE} in Ar is initially higher than He at distances near the target (≤ 0.4 cm). At longer distances, the v_{LE} in Ar decreases to values lower than the He v_{LES} , reflecting the large difference in mass between the two background gases. The v_{LE} is similar for all pressures of Ar until ~ 0.4 cm, at which point the leading-edge velocity begins to decrease at increasing rates with increasing background pressure Ar. While the v_{LE} values in Ar differ, with the smallest decrease in v_{LE} observed for 250 mTorr and the largest observed for 1000 mTorr, after ~ 1.2 cm all of the pressures show similar decreases in v_{LE} at rates of ~ 0.41 to 0.48 cm/ μ s per cm.

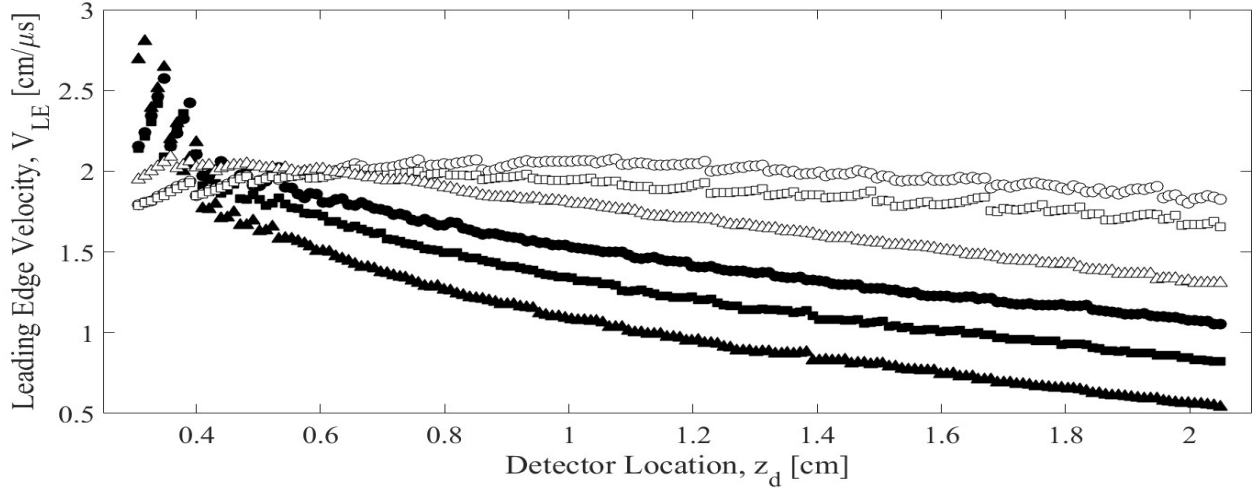


Figure 34. Broadband Ti velocity distribution leading-edge velocity for (●) 250 mTorr Ar, (■) 500 mTorr Ar, (▲) 1000 mTorr Ar, (○) 250 mTorr He, (□) 500 mTorr He, and (△) 1000 mTorr He.

The He v_{LE} begin by increasing over a small range of distances before decreasing. The v_{LE} from Ti expansion into 1000 mTorr of He increases slightly from 0.3 to 0.4 cm before decreasing at a constant rate of $0.476 \pm .004$ cm/ μ s per cm, approximately the same rate at which the v_{LE} from Ti expansion into 1000 mTorr of Ar decreases at long times. The v_{LE} in both 250 and 500 mTorr increase at equivalent rates until approximately 0.55 cm, at which point the 500 mTorr v_{LE} begins to slow and decreases at 0.7 cm and the increase in the 250 mTorr v_{LE} begins to slow and then finally decrease at ~ 1 cm.

Hydrodynamic calculations by Wood et al have calculated a background density of approximately 1 order of magnitude higher than the expanding plume for Si ablation into 175 mTorr He due to momentum transfer from the plume to the background gas [149]. Due to the large mass difference between He and Ti, He atoms are initially easily scattered out of the path oncoming plume, resulting in increasing leading edge velocities despite the

collisions. Only after the He background has had a chance to build up pressure in front of the Ti plume does the v_{LE} begin to slow.

Consideration of conservation of momentum and energy (assuming a collision impact factor of $b=0$) results in plume speed after a collision with the background gas [150]

$$v'_{Ti} = \frac{[(m_{Ti} - m_{background}) * v_{Ti} + 2m_{Abg}v_{background}]}{m_{Ti} + m_{background}} \quad (31)$$

where the Ti mass, m_{Ti} , is comparable to the background gas mass, m_b , only for Ar. Assuming a head-on elastic collision between Ti at a velocity of 1 cm/ μ s in the +z direction and an Ar atom at a velocity indicative of a thermal temperature of 294 K in the same direction ($\sim 3.5 \times 10^{-2}$ cm/ μ s) results in the Ti atom traveling at a speed of 0.122 cm/ μ s in the original direction or a decrease of 88% in velocity. So long as the background gas and the Ti atoms are moving in the same direction (+z), the Ti atom can never be backscattered [149]. A comparative analysis under the same collision circumstances but with a He atom results in only a 14% decrease in Ti velocity. The largest Ti atom scatter angle after the collision is $\sin^{-1}(m_{background}/m_{Ti})$ or 56° and 5° for collisions with Ar and He, respectively [150].

Fits of the SMB distribution (Eq. 30) were applied to higher pressure distribution data of Figure 33. In comparison to the fair agreement between the vacuum velocity distribution data and the SMB distributions, generally poor agreement was observed for the higher background pressure distributions, as the rather abrupt decrease of the distribution at higher velocity results in structured residuals (see Figure 35). The peak residuals in vacuum for similar distance from the target were 10% less than those in Figure 35 and were unstructured, indicating a more quality fit.

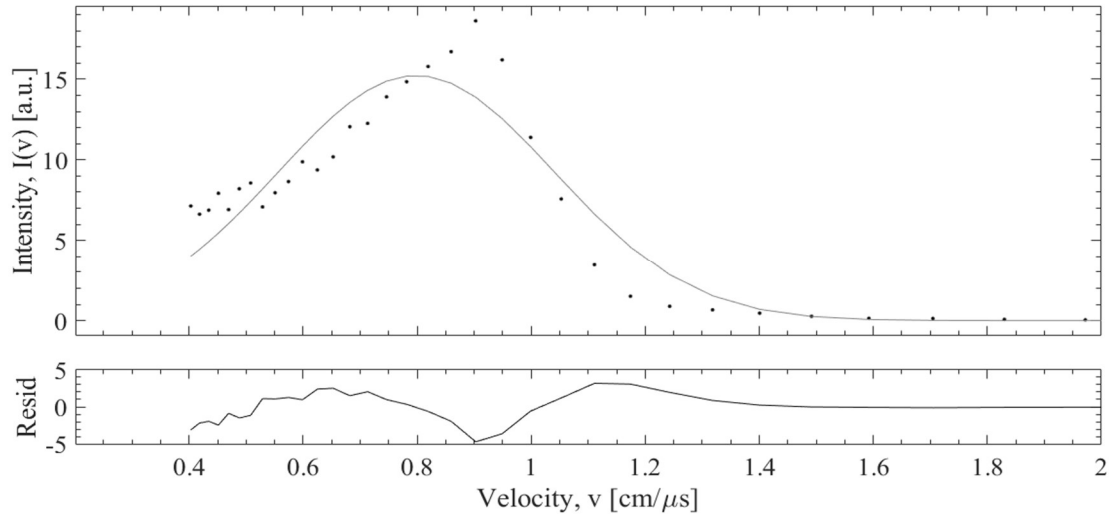


Figure 35. SMB fit and residuals to Ti II velocity distribution for 240 mJ in 1000 mTorr Ar at $z=0.89$ cm (fit parameters $T=33821 \pm 7534$ K, $u=7985 \pm 248$ cm/μs, $n=0$.)

Comparison of the mechanics analysis above with the experimental results from Figure 33 show a considerable difference in the velocity distribution of Ti lost due to a collision. Figure 33 shows that the fastest velocity group for Ti expansion into Ar (~ 1.8 cm/μs) at a detector location of 0.4 cm is removed. The next velocity group shown to be scattered is at ~ 1.7 cm/μs at $z=0.5$ cm, however this velocity group appears with an apparent 13% increase in maximum intensity. Similar apparent discrepancies with classical mechanics exist for the dynamics of the velocity distribution into He background along the leading edge, making interpretation of the data difficult.

In creating conventional TOF profiles (in the manner presented here), it is assumed that the observed intensity is from plume constituents that traveled a distance $z(t)$ with a constant velocity $v=z(t)/t$. This assumption is valid under vacuum plume expansion conditions, in which it is unlikely that intraplume collisions significantly alter the velocity of the particles, and construction of the corresponding velocity distributions is straightforward. Plume expansion into pressure environment, comparatively, is dominated

by collisions with the background gas, resulting in plume slowing with increasing background pressure [138] and scattering of the largest velocity groups. The velocity group at which a detected scattered atom is registered might then correspond to an incorrect velocity group, making interpretation of the data difficult. Additionally, the pressure and temperature behind the Ti expanding plume shock front in 1 Torr Ar have been estimated to be $\sim 1.7 \times 10^6$ mTorr and 10 eV, respectively, at a distance of 0.5 cm from the target [138], resulting in intraplume mean free paths of ~ 0.03 mm assuming a velocity independent cross section [151] (for reference, the mean free path of a Ti atom expanding into 1 Torr Ar is ~ 0.2 mm [151]). Because the mean free path is a fraction of a pixel, it is implied that multiple collisions occur within one pixel. The high intraplume pressures might quickly result in altered nascent product velocity distributions due to intraplume collisions, producing seemingly unexplainable velocity distributions and adding a further complexity to data interpretation.

It is of interest to determine conditions at which the Ti distribution in vacuum might be used as an approximation for a distribution at pressure. Similar trajectory data between expansion into vacuum and expansion into pressure background can be used to reveal regions where it might be appropriate to utilize the vacuum distribution as a surrogate for the distribution into pressure background. Figure 36 shows the trajectory of Ti expansion into various He backgrounds. The Ti front is defined by the location of the emissive front at 10% of the maximum intensity. At delays up to 180 ns, the expanding plume into all pressures shares the same trajectory with a velocity of ~ 1.57 cm/ μ s. As the He pressure is increased, collisions between the expanding plume and the background gas slow the plume. The Ti trajectory into 250 and 500 mTorr He is similar to the trajectory in vacuum for

distances up to ~ 1.2 cm; comparatively, the trajectory into 1000 mTorr He is only similar to the vacuum trajectory for distances up to ~ 0.2 cm from the target. An approximate stopping distance of 3 cm is shown for expansion into 1000 mTorr He; the imaging system field of view limited observation of the stopping distances of the lower He pressures. We have previously shown stopping distances for expanding Ti plume in various Ar pressures ranging from ~ 6 cm for expansion into 50 mTorr Ar to 2.7 cm for expansion into 1000 mTorr Ar [138].

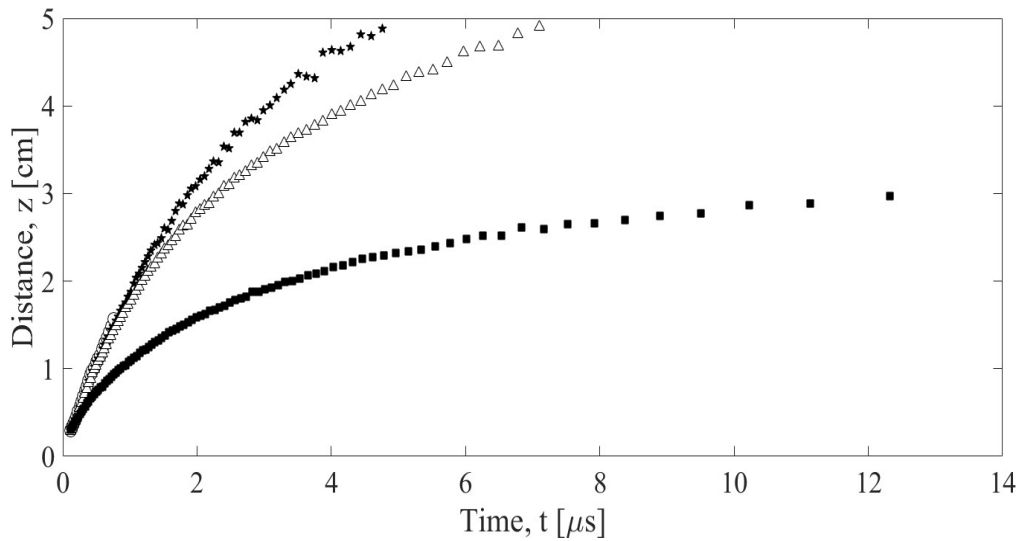


Figure 36. Ti plume trajectories for 240 mJ irradiation expansion into (○) vacuum, (★) 250 mTorr, (△) 500 mTorr, and (■) 1000 mTorr He.

Figure 37 shows the differences between the plume expansion distribution into vacuum and 250 mTorr He and Ar. Here the Ti distribution into 250 mTorr He displays a clear low velocity distribution similar to the Ti I distribution 1, in contrast to the lack of such a clear distribution in the 1000 mTorr He distribution in Figure 33(b). The leading edge of the distribution in 250 mTorr is similar to that of the distribution into vacuum and the three distribution peak intensities appear to be in similar velocity groups to those

observed in the distribution into vacuum. The intensities from 0.7 to 1.3 cm/ μ s and < 0.3 cm/ μ s are decreased some relative to the distribution into vacuum but overall agreement is found between the two distributions within the region of similar trajectories for expansion into vacuum and 250 mTorr He.

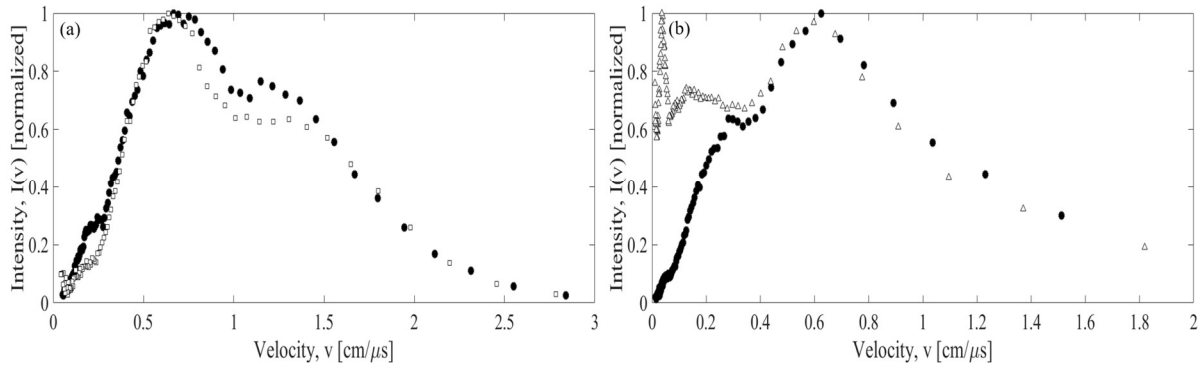


Figure 37. Velocity distribution differences between Ti expansion into (●) vacuum and 250 mTorr (a) (□) He at 0.5 cm and (b) (△) Ar at 0.12 cm.

Figure 37(b) now compares the Ti velocity distribution in vacuum with that into 250 mTorr Ar at 0.12 cm from the target. In contrast to the general agreement observed between the distribution into vacuum and into 250 mTorr He, large disagreement is observed between the Ti velocity distribution into vacuum and into 250 mTorr Ar, particularly at the low velocity groups. Bauer et al have shown that trajectory data from Ti ablation in various Ar pressures up to 1000 mTorr are similar to that of Ti ablation in vacuum for distances up to 0.15 cm away from the target [138]. However, the large discrepancies between the observed velocity distributions at similar early distances make it appear that substitution of the distribution into vacuum for distribution into Ar is not practical at pressures ≥ 250 mTorr. Additionally, the large differences observed between the distributions into He and Ar further highlight that the mass of the background gas is a significant factor in understanding of the plume expansion dynamics.

A summary of the key findings and issues is now warranted. Highly spatially resolved Ti TOF distributions obtained from ICCD images reveals complex evolution of the expanding plume. Multi-modal distributions are observed for expansions into vacuum, He, and Ar and are partially attributed to the presence of neutral and ionized plume species. Combined SMB distribution appears to describe the expanding plume distribution in vacuum; however, the ability to fit the data with various combinations of fit parameters questions the appropriateness of this distribution for the data. At elevated pressure a SMB distribution is completely inadequate to describe the existing distribution. The change in the expanding plume velocity distribution is highly dependent on the ambient environmental parameters leading to the conclusion that velocity distributions are dynamically controlled and statistical analysis arguments are inadequate.

Extracting velocity distributions from the emission TOF data utilized in this work is difficult due to many factors. The evolution of the emissive plumes depends on both the velocity distribution and unknown translation-to-electronic excitation rates. Transformation of evolving intensities to velocity distributions utilizes the linear relationship $v=z/t$, obscuring the product velocities and size of the velocity change. Collisions with the ambient environment significantly affect the plume expansion characteristics. Excitation and speed distributions of the background gas would complement the plume dynamics. Ar emissions were not observed for Ti expansion in these experiments so further diagnostic development is required.

The emissions TOF technique utilized in this work may be adaptable to obtaining high energy collision information that is difficult to determine through conventional

methods. Translational-electronic collision cross section data at the high kinetic energies obtained in expanding laser ablation plumes might be determined through the coupling of laser absorption diagnostics and the emissions TOF experimental techniques and non-hydrodynamic simulations. These cross sections are required for a full description of the evolving velocity distributions and kinetics observed in the expansion of laser ablated plumes.

5.4 Conclusion

Fast emissions imaging has been utilized to construct Ti velocity distributions for different spatial locations along the plume centerline for vacuum and Ar and He background gases at various pressures. Vacuum Ti I velocity distributions appear to be generally consistent with shifted Maxwell Boltzmann velocity distributions. Trimodal distributions are observed for Ti I species but only single distributions are observed for Ti II. The Ti I species fast and distribution displays characteristics strongly indicative of the Ti II distribution. Ti velocity distributions in ≥ 250 mTorr Ar and He are not consistent with shifted Maxwell Boltzmann distributions, reflecting strong velocity changing collisions to the high-velocity groups of the velocity distribution with the background gas. TOF measurements of laser ablated plumes into background pressure are inherently troubled and interpretation of the results should be coupled with strong computational analysis tools to extract the true velocity distribution.

VII. Conclusions

Increased interest in tactical laser weapon use demands a deeper understanding of laser-material interaction to better predict engagement outcomes. The use of target folders from empirical characterization for all tactical scenarios is unrealistic. This work has aimed to accomplish parts of this over-arching goal by focusing on components of two tactical aerospace defense scenarios: characterization of molecular products C₂ and CN from continuous wave (cw) laser heating of graphite and pulsed laser ablation plume dynamics of Al and Ti. Experimental data has been analyzed to not only describe the heating and ablation conditions for the specific laser material interactions in this research but to provide insights into the broader physics occurring during laser lethality engagement. Furthermore, the experimental data sets detailed in this work can serve as high-fidelity benchmark data for laser-material interaction simulations. Non-defense communities such as thin film production, laser welding manufacturing, and laser induced breakdown spectroscopy will also find this data useful to help guide understanding and experimental lab efforts. After summarizing the key conclusions from this dissertation, follow-on research suggestions will highlight areas of laser lethality that are poorly understood and require investigation.

6.1 Visible emission from C₂ and CN during cw laser-irradiated graphite

Investigation of the visible emissions of graphite molecular products C₂ and CN and corresponding surface temperatures from laser heating of graphite with a high irradiance ($\leq 3.5 \text{ kW/cm}^2$) cw laser have been accomplished. The dependence of the ratio of C₂ Swan and CN red emission intensities on laser irradiance, surface temperature, and

sample porosity has been characterized for various graphite samples. Thermal steady-state conditions are reached at less than 20 s for high irradiance cases ($< 3.5 \text{ kW/cm}^2$). An approximately 20 times higher $[\text{C}_2(\text{d})]/[\text{CN}(\text{A})]$ concentration ratio is recorded with modest air flow over the surface at 5 m/s. The corresponding surface temperatures of $\sim 3500 \text{ K}$ at 1.4 kW/cm^2 increase by $< 5\%$ relative to buoyant flow conditions. Surface nitridation kinetics are revealed and are of interest in the development of thermal protection systems for reentry vehicles and for predicting degradation during counter-air laser interaction with carbon containing materials. Significantly lower column densities relative to oxidation products CO and CO_2 suggest that C_2 and CN forming reactions are relatively insignificant, even at elevated surface temperatures. The modeling of carbon composite laser engagements should emphasize combustion over sublimation and nitridation kinetics. The ratio of C_2 and CN total column densities extrapolated from the observed excited states is inconsistent with an equilibrium analysis, suggesting that laser ablation models consider partitioning of energy into electronic, vibrational, and rotational energy. Graphite surface emissivity increases with temperature by about 8% and must be better characterized to more accurately determine the thermal properties of graphite. The sublimation temperature is key to understanding degradation of graphite containing materials like thermal protection systems and carbon fiber skins for aircraft. Furthermore, understanding the emissivity evolution with temperature and phase transition is a more general problem for optical pyrometry and the remote sensing community.

6.2 Comparison of plume dynamics for laser ablated metals: Al and Ti

A self-contained systematic characterization and analysis (relative to other reported studies) of bulk Ti and Al plume expansion dynamics from up to 3.5 J/cm^2 UV pulsed laser

ablation in vacuum and Ar gas environment was accomplished via temporally and spatially resolved emissions imaging and gravimetric analysis. The joint utilization of these techniques provides unique information on the plume dynamics and laser-plume coupling. Ablation thresholds of 1.12 J/cm^2 and 1.73 J/cm^2 for KrF 248 nm irradiation of Ti and Al respectively were determined from gravimetric measurements and less than $0.8 \text{ }\mu\text{g}$ material was ablated for either metal. Highly energetic vapor plumes (up to 61 eV/atom) are formed, presenting extreme momentum transfer conditions that must be considered for either targeting or laser hardening of system components in tactical lethality scenarios. Vapor plasmas containing singly ionized species of Al and Ti are observed and the relationship between vapor plasma shielding of the surface, mass removed, and background pressure is characterized. Mass loss for Ti increases from $0.1 - 0.8 \text{ }\mu\text{g/pulse}$ as pulse energy increases from $174 - 282 \text{ mJ/pulse}$ and decreases by $\sim 30 \%$ as pressure increases from vacuum to 1 Torr. Benchmarking data for pulsed laser ablation of metals is provided for development of laser lethality codes that may then be applied to pulsed laser ablation of other materials of interest (such as those used in optical systems). Optical signatures such as the plume stopping distance are provided to aid in lab design for material manufacturing.

6.3 Laser ablated Ti velocity distribution dynamics

KrF Ti ablated plume velocity distributions were constructed from fast gated emissions imaging time-of-flight data, offering the advantage over other TOF methods in that the spatial evolution of the distribution was easily recorded. Multi-modal velocity distributions are observed, revealing complex laser-target and laser-plume phenomena.

Application of the conventional shifted Maxwell-Boltzmann distribution is inadequate, particularly for expansion into pressure environment. The highest velocity components of the distribution are scattered by collisions with the background gas in a manner inconsistent with a shifted Maxwell-Boltzmann distribution. The distribution dynamics strongly depend on the mass of the background gas, as higher momentum transfer from collisions of the expanding laser plume with heavier background gases resulted in significant differences in the characteristics of the leading-edge velocity components. It is identified that conventional application of TOF technique to laser ablated plumes expanding into pressure environment is hindered by velocity changing collisions of the particles, making interpretation of the results difficult without significant consideration of translation-to-electronic excitation rates, intraplume collisions, and non-hydrodynamic conditions. Finally, a possible method for determining high-energy translation-to-excitation cross sections is identified due to the extreme expansion conditions inherent in laser induced plumes. However, significant computational aid is required to detangle the impact of velocity changing collisions on the recorded data before the cross sections can be recovered.

6.4 Recommendations for Future Work

This work provides a significant contribution to the existing knowledge of laser heating of graphite and laser ablation of metals. However, there remain a large number of related issues that are poorly understood. Additional experimental data (suggested below) can help clarify some of the experimental observations contained in this work and provide further insights into understanding of laser material interaction. Significant theoretical

investigation of plume expansion is also required and additional experimental data may serve as benchmarks to simulations currently available or being developed.

Accurate knowledge of evolving gas temperatures and molecular species concentrations during laser heating of graphite would provide more accurate benchmarks for predictive modeling of carbon composite laser heating. A fair amount of scatter was observed in the gas temperatures derived from the spectroscopy of C₂ and CN due to the moderate spectral resolution of the spectrometer used in the analysis. Graphite laser heating studies utilizing higher spectral resolution instruments would allow for calculating more accurate rovibronic temperatures and a clearer comparison of C₂ and CN excitation temperatures. Furthermore, inclusion of additional electronic states in spectroscopic analysis such as CN violet would allow for determination of the species electronic temperature and total concentration in the plume.

The sublimation temperature of graphite is a key material parameter that is only known to within $\sim\pm 63$ K [50]. The error bounds established in this work for the sublimation temperature (± 91 K) were limited by post-shot emissivity measurements recorded using hemispherical reflectance. Temperature determination via remote thermal emissions collection is hindered by inadequate knowledge of the emissivity dynamics regardless of material. A detailed study of the evolution of graphite emissivity with temperature would lead to a better estimate of the graphite surface temperature (and sublimation temperature) and significant contribution to the remote collections community at large. A start to such a study might be accomplished through the use of a Fourier

transform spectrometer observing a graphite sample of known temperature to extract temperature dependent emissivity information.

A thorough understanding of the partitioning of laser energy into the material and plume is required for predictive laser lethality simulations. Sedov-Taylor blast model is shown to adequately determine the laser-shock front coupling. However, it was noted that the use of gated ICCD can only observe the excited plume constituents, and that the literature has shown that the shock front breaks away from the vapor plume as the contact front slows down due to collisions with the background gas. A study comparing the results from emissions and a technique to observe the actual shock front such as Schlieren imaging for Al and Ti ablation conditions utilized in this work would provide the shock front breakaway location, allowing for more accurate determination of shock energy via Sedov-Taylor model.

Paramount to the understanding of laser plume dynamics is knowledge of the velocity distributions of the ablated species. This research has displayed multi-mode distributions that appear in part to be characterized by a shifted Maxwell Boltzmann distribution. However, deviations from this distribution also appear for both expansion in vacuum and into pressure background. Because this research only observed the excited (emitting) atoms, it is possible that the deviation from theory is based on the excitation rate details. A study of the non-emissive plume constituents through the use of an active probing technique like absorption spectroscopy would allow for comparison of the emitting and non-emitting plume velocity distributions to determine the effect of excitation production. Additionally, a comparative study between the emission and absorption

spectroscopy might allow for development of a method to calculate excitation cross sections of the ablated species, which could then be applied to the larger problem of determining high energy excitation cross sections.

Appendix A. Molecular Spectroscopy Constants

Table 6. Molecular constants for C₂ Swan system (d³Π_g) (cm⁻¹) [80]

v	A	A _D	B _v	D _v
0	-14.00139	0.0005068	1.7455663	6.8205x10 ⁻⁶
1	-13.87513	0.0005740	1.7254062	7.0194 x10 ⁻⁶
2	-13.8205	0.000600	1.704516	7.308 x10 ⁻⁶
3	-13.5361	0.000775	1.681437	7.438 x10 ⁻⁶
4	-13.3892	0.001451	1.656859	7.684 x10 ⁻⁶
5	-13.0324	0.000723	1.630205	8.573 x10 ⁻⁶
6	-12.820	0.001203	1.599876	8.998 x10 ⁻⁶
7	-12.3458	0.000814	1.566047	1.0044 x10 ⁻⁵
8	-12.107	0.00076	1.52675	9.60 x10 ⁻⁶
9	-11.698	0.00076	1.485755	1.185 x10 ⁻⁵
10	-11.297	0.00076	1.441138	1.2837 x10 ⁻⁵

Table 7. Vibrational constants for C₂ Swan system (d³Π_g) and CN Red system (A²Π) (cm⁻¹) [80], [83]

Constant	d ³ Π _g	A ² Π
<i>ω_e</i>	1788.45	1813.28845
<i>ω_ex_e</i>	16.87	12.77789
<i>ω_ey_e</i>	-0.259	-0.001775
<i>ω_ez_e</i>	-0.0396	--

Table 8. Molecular constants for CN Red system ($A^2\Pi$) (cm^{-1}) [83]

v	A_v	$A_{Dv}(\times 10^4)$	$A_{Hv}(\times 10^9)$	B_v	$D_v(\times 10^6)$	$H_v(\times 10^{12})$
0	-52.65443	-2.1998	4.959	1.70713832	6.14473	3.921
1	-52.58078	-2.1979	5.826	1.68986156	6.15575	3.552
2	-52.50526	-2.211	7.96	1.67254021	6.16910	3.418
3	-52.43236	-1.9577	4.650	1.65516963	6.18175	2.734
4	-52.35628	-1.862	4.307	1.63775143	6.19839	2.424
5	-52.28969	-1.416	-5.88	1.62028792	6.22247	2.878
6	-52.24814	-0.77	-1.02	1.60279825	6.25696	3.575
7	-52.3431	-5.46	469	1.5851663	5.629	--
8	-50.6597	1.43	-992	1.5676896	5.167	-1.228
9	-51.4574	-3.725	20.2	1.5497799	6.3091	3.640
10	-51.4287	-3.515	35.2	1.5319138	6.3134	--
11	-51.3129	-2.54	-143	1.513983	6.208	--
12	-51.1664	-3.9	0	1.496057	6.372	--
13	-51.0043	-2.73	0	1.477919	6.311	--
14	-50.8025	-4.46	0	1.459615	6.329	--
15	-50.6074	-3.251	0	1.4412985	6.390	--
16	-50.3830	-2.443	0	1.4229173	6.556	--
17	-50.5251	-12.26	0	1.404828	5.65	--
18	-49.8632	-3.412	0	1.3853108	6.572	--
19	-49.4910	-2.591	0	1.366389	6.663	--
20	-49.1747	-6.14	2800	1.347266	4.855	--
21	-48.7582	-5.76	0	1.327242	6.211	--
22	-48.3969	0	0	1.307745	7.211	--

Bibliography

- [1] G. P. Perram, S. Cusumano, R. L. Hengehold, and S. T. Fiorino, *Introduction to Laser Weapon Systems*. Albuquerque: Directed Energy Professional Society, 2010.
- [2] P. E. Nielsen, "Effects of Directed Energy Weapons," Washington D.C., 1994.
- [3] M. Gunzinger and C. Dougherty, "Changing the Game: The Promise of Directed-Energy Weapons," 2012.
- [4] L. Mastroianni, "Ground-Based Air Defense Directed Energy On-the-Move," *Office of Naval Research Fact Sheet*. [Online]. Available: <https://www.onr.navy.mil/en/Media-Center/Fact-Sheets/GBAD>. [Accessed: 03-Jul-2017].
- [5] "The Army high-Energy Laser Mobile Demonstrator," 2015. [Online]. Available: https://www.army.mil/standto/archive_2015-09-09.
- [6] A. S. A. Board, "New World Vistas Air and Space Power for the 21st Century Directed Energy Volume," 1995.
- [7] A. S. A. Board, "New World Vistas Air and Space Power for the 21st Century Sensors Volume," 1995.
- [8] G. Jennings, "Northrop Grumman to develop laser pod to protect USAF fighters," *IHS Jane's Intermediate Defence Review*, 2016. [Online]. Available: <http://www.janes.com/article/63185/northrop-grumman-to-develop-laser-pod-to-protect-usaf-fighters>. [Accessed: 03-Jul-2017].
- [9] D. Macdonald *et al.*, "New World Vistas Materials Volume," 1995.
- [10] S. J. Lewis, "The use of carbon fibre composites on military aircraft," *Compos.*

- Manuf.*, vol. 5, no. 2, pp. 95–103, 1994.
- [11] C. E. Harris and M. J. Shuart, “An assessment of the state-of-the-art in the design and manufacturing of large composite structures for aerospace vehicles,” Hampton, 2001.
- [12] J. Hale, “Boeing 787 from the Ground Up 06,” *AERO Magazine*, Seattle, pp. 1–9, 2006.
- [13] N. C. Herr, “Degradation of carbon fiber reinforced polymer and graphite by laser heating,” Air Force Institute of Technology, 2016.
- [14] S. S. Harilal, R. C. Issac, C. V Bindhu, V. P. N. Nampoori, and C. P. G. Vallabhan, “Optical emission studies of species in laser-produced plasma from carbon,” *J. Phys. D. Appl. Phys.*, vol. 30, no. 12, pp. 1703–1709, 1999.
- [15] D. B. Chrisey and G. K. Hubler, *Pulsed Laser Deposition of Thin Films*. New York: John Wiley & Sons, Inc., 1994.
- [16] L. St-Onge, R. Sing, S. Bechard, and M. Sabsabi, “Carbon emissions following 1.064 μm laser ablation of graphite and organic samples in ambient air,” *Appl. Phys. A Mater. Sci. Process.*, vol. 69, pp. 913–916, 1999.
- [17] S. Harilal, C. V Bindhu, R. C. Issac, V. P. N. Nampoori, and C. P. G. Vallabhan, “Electron density and temperature measurements in a laser produced carbon plasma,” *J. Appl. Phys.*, vol. 82, no. 5, pp. 2140–2146, 1997.
- [18] R. K. Thareja, R. K. Dwivedi, and K. Ebihara, “Interaction of ambient nitrogen gas and laser ablated carbon plume: Formation of CN,” *Nucl. Instruments Methods Phys. Res. Sect. B Beam Interact. with Mater. Atoms*, vol. 192, no. 3, pp. 301–310, 2002.

- [19] G. Dinescu, E. Aldea, M. L. De Giorgi, A. Luches, A. Perrone, and A. Zocco, "Optical emission spectroscopy of molecular species in plasma induced by laser ablation of carbon in nitrogen," *Appl. Surf. Sci.*, vol. 127–129, pp. 697–702, 1998.
- [20] S. S. Harilal, R. C. Issac, C. V Bindhu, V. P. N. Nampoori, and C. P. G. Vallabhan, "Temporal and spatial evolution of C₂ in laser induced plasma from graphite target," *J. Appl. Phys.*, vol. 80, no. 6, p. 3561, 1996.
- [21] S. Abdelli-Messaci, T. Kerdja, A. Bendib, S. M. Aberkane, S. Lafane, and S. Malek, "Investigation of carbon plasma species emission at relatively high KrF laser fluences in nitrogen ambient," *Appl. Surf. Sci.*, vol. 252, no. 5, pp. 2012–2020, 2005.
- [22] K. F. Al-Shboul, S. S. Harilal, and A. Hassanein, "Gas dynamic effects on formation of carbon dimers in laser-produced plasmas," *Appl. Phys. Lett.*, vol. 99, no. 13, pp. 30–33, 2011.
- [23] A. I. Savvatimskiy, "Measurements of the melting point of graphite and the properties of liquid carbon (a review for 1963 – 2003)," *Carbon N. Y.*, vol. 43, pp. 1115–1142, 2005.
- [24] Steen, William M. and J. Mazumder, *Laser Material Processing*, 4th ed. New York: Springer, 2010.
- [25] P. R. Willmott and J. R. Huber, "Pulsed laser vaporization and deposition," *Rev. Mod. Phys.*, vol. 72, no. 1, pp. 315–328, 2000.
- [26] S. Amoruso, M. Armenante, V. Berardi, R. Bruzzese, and N. Spinelli, "Absorption and saturation mechanisms in aluminium laser ablated plasmas," *Appl. Phys. A Mater. Sci. Process.*, vol. 271, pp. 265–271, 1997.

- [27] P. Écija *et al.*, “Fundamental processes in nanosecond pulsed laser ablation of metals in vacuum,” *Phys. Rev. A*, vol. 77, pp. 0329041–0329048, 2008.
- [28] G. Baraldi, A. Perea, and C. N. Afonso, “Dynamics of ions produced by laser ablation of ceramic Al₂O₃ and Al at 193 nm,” *Appl. Phys. A Mater. Sci. Process.*, vol. 105, pp. 75–79, 2011.
- [29] V. Y. Baranov, O. N. Derkach, V. G. Grishina, M. F. Kanevskii, and A. Y. Sebrant, “Dynamics and stability of an expanding laser-induced plasma in a low-density gas,” *Phys. Rev. E*, vol. 48, no. 2, pp. 1324–1330, 1993.
- [30] S. Amoruso, V. Berardi, R. Bruzzese, R. Capobianco, R. Velotta, and M. Armenante, “High fluence laser ablation of aluminum targets: Time-of-flight mass analysis of plasmas produced at wavelengths 532 and 355 nm,” *Appl. Phys. A Mater. Sci. Process.*, vol. 541, pp. 533–541, 1996.
- [31] S. S. Harilal, G. V. Miloshevsky, P. K. Diwakar, N. L. Lahaye, and A. Hassanein, “Experimental and computational study of complex shockwave dynamics in laser ablation plumes in argon atmosphere,” *Phys. Plasmas*, vol. 19, no. 8, pp. 1–11, 2012.
- [32] S. S. Harilal, C. V Bindhu, M. S. Tillack, F. Najmabadi, and a C. Gaeris, “Plume splitting and sharpening in laser-produced aluminium plasma,” *J. Phys. D. Appl. Phys.*, vol. 35, no. 22, pp. 2935–2938, 2002.
- [33] a. K. Sharma and R. K. Thareja, “Plume dynamics of laser-produced aluminum plasma in ambient nitrogen,” *Appl. Surf. Sci.*, vol. 243, no. 1–4, pp. 68–75, 2005.
- [34] W. F. Luo *et al.*, “Characteristics of the aluminum alloy plasma produced by a 1064 nm Nd : YAG laser with different irradiances,” *Pramana-Journal Phys.*, vol.

- 74, no. 6, pp. 945–959, 2010.
- [35] O. Albert *et al.*, “Time-resolved spectroscopy measurements of a titanium plasma induced by nanosecond and femtosecond lasers,” *Appl. Phys. A Mater. Sci. Process.*, vol. 76, pp. 319–323, 2003.
- [36] A. De Giacomo, “Experimental characterization of metallic titanium-laser induced plasma by time and space resolved optical emission spectroscopy,” *Spectrochim. Acta - Part B At. Spectrosc.*, vol. 58, no. 1, pp. 71–83, 2003.
- [37] M. Hanif, M. Salik, and M. A. Baig, “Optical Spectroscopic Studies of Titanium Plasma Produced by an Nd : YAG Laser 1,” *J. Russ. Laser Res.*, vol. 35, no. 3, pp. 230–238, 2014.
- [38] C. G. Parigger, A. C. Woods, D. M. Surmick, L. D. Swafford, and M. J. Witte, “Measurements of ultra-violet titanium lines in laser-ablation plasma,” *Spectrochim. Acta - Part B At. Spectrosc.*, vol. 99, pp. 15–19, 2014.
- [39] L. Torrisi, D. Margarone, A. Borrielli, and F. Caridi, “Ion and photon emission from laser-generated titanium-plasma,” *Appl. Surf. Sci.*, vol. 254, pp. 4007–4012, 2008.
- [40] O. Albert *et al.*, “Time-resolved spectroscopy measurements of a titanium plasma induced by nanosecond and and femtosecond lasers,” *Appl. Phys. A Mater. Sci. Process.*, vol. 76, pp. 319–323, 2003.
- [41] D. Bauerle, *Laser Processing and Chemistry*, Third. Berlin: Springer, 2000.
- [42] C. P. Grigoropoulos, *Transport in Laser Microfabrication*. New York: Cambridge University Press, 2009.
- [43] W. Bauer, C. Fox, R. Gosse, and G. Perram, “Visible emission from C 2 and CN

- during cw laser-irradiated graphite,” *Opt. Eng.*, vol. 56, no. 1, 2016.
- [44] W. Bauer, G. Perram, and T. Haugan, “Plume dynamics from UV pulsed ablation of Al and Ti,” *SPIE Conf. Proc.*, no. 10114, 2016.
- [45] C. J. Druffner, G. P. Perram, and R. R. Biggers, “Time-of-flight emission profiles of the entire plume using fast imaging during pulsed laser deposition of YBa₂Cu₃O_{7-x},” *Rev. Sci. Instrum.*, vol. 76, no. 9, p. 93101, 2005.
- [46] J. C. S. Kools *et al.*, “Gas flow dynamics in laser ablation deposition,” *J. Appl. Phys.*, vol. 71, no. 9, pp. 4547–4556, 1992.
- [47] W. M. Haynes, *CRC Handbook of Chemistry and Physics, 93rd Edition*. 2012.
- [48] A. M. Prokhorov, V. I. Konov, I. Ursu, and I. N. Mihailescu, *Laser Heating of Metals*. New York: Adam Hilger, 1990.
- [49] G. T. Phillips *et al.*, “Mass removal by oxidation and sublimation of porous graphite during fiber laser irradiation,” *Opt. Eng.*, vol. 56, no. 1, 2016.
- [50] J. Abrahamson, “Graphite sublimation temperatures, carbon arcs, and crystallite erosion,” *Carbon N. Y.*, vol. 12, pp. 111–141, 1974.
- [51] W. Demtroder, *Laser Spectroscopy Volume 2 Experimental Techniques*, 4th ed. Berlin: Springer, 2008.
- [52] N. W. Ashcroft and N. D. Mermin, *Solid State Physics*. Pacific Grove: Brooks Cole, 1976.
- [53] N. M. Bulgakova and A. V. Bulgakov, “Pulsed laser ablation of solids: transition from normal vaporization to phase explosion,” *Appl. Phys. A Mater. Sci. Process.*, vol. 73, no. 2, pp. 199–208, 2001.
- [54] X. Xu, “Phase explosion and its time lag in nanosecond laser ablation,” *Appl. Surf.*

- Sci.*, vol. 197–198, pp. 61–66, 2002.
- [55] C. Porneala, D. A. Willis, C. Porneala, and D. A. Willis, “Observation of nanosecond laser-induced phase explosion in aluminum,” *Appl. Phys. Lett.*, vol. 89, no. 211121, pp. 1–4, 2006.
- [56] C. R. Phipps, *Laser Ablation and its Applications*. New York: Springer, 2007.
- [57] Y. B. Zel’dovich and Y. P. Raizer, *Physics of shock waves and high-temperature hydrodynamic phenomena*. New York: Dover Books, 2002.
- [58] H. Schittenhelm, G. Callies, P. Berger, and H. Hugel, “Investigations of extinction coefficients during excimer laser ablation and their interpretation in terms of Rayleigh scattering,” *J. Phys. D. Appl. Phys.*, vol. 29, pp. 1564–1575, 1996.
- [59] H. Schittenhelm, G. Callies, A. Straub, P. Berger, and H. Hugel, “Measurements of wavelength-dependent transmission in excimer laser-induced plasma plumes and their interpretation,” *J. Phys. D. Appl. Phys.*, vol. 31, no. 418–427, 1998.
- [60] R. Rozman, I. Grabec, and E. Govekar, “Influence of absorption mechanisms on laser-induced plasma plume,” *Appl. Surf. Sci.*, vol. 254, pp. 3295–3305, 2008.
- [61] T. Moscicki, J. Hoffman, and J. Chrzanowska, “The absorption and radiation of a tungsten plasma plume during nanosecond laser ablation,” *Phys. Plasmas*, vol. 22, no. 103303, pp. 1–7, 2015.
- [62] A. De Giacomo, M. Dell’Aglia, D. Bruno, R. Gaudiuso, and O. De Pascale, “Experimental and theoretical comparison of single-pulse and double-pulse laser induced breakdown spectroscopy on metallic samples,” *Spectrochim. Acta - Part B At. Spectrosc.*, vol. 63, no. 7, pp. 805–816, 2008.
- [63] N. M. Shaikh, S. Hafeez, B. Rashid, and M. A. Baig, “Spectroscopic studies of

- laser induced aluminum plasma using fundamental, second and third harmonics of a Nd:YAG laser,” *Eur. Phys. J. D*, vol. 44, no. 2, pp. 371–379, 2007.
- [64] S. S. Harilal, C. V. Bindhu, V. P. N. Nampoori, and C. P. G. Vallabhan, “Influence of ambient gas on the temperature and density of laser produced carbon plasma,” *Appl. Phys. Lett.*, vol. 72, no. 2, pp. 167–169, 1998.
- [65] A. M. Keszler and L. Nemes, “Time average emission spectra of Nd:YAG laser induced carbon plasmas,” *J. Mol. Struct.*, vol. 695–696, pp. 211–218, 2004.
- [66] H. R. Griem, *Plasma Spectroscopy*. New York: McGraw-Hill, 1964.
- [67] G. Bekefi, *Principles of Laser Plasmas*. New York: Wiley, 1976.
- [68] A. De Giacomo *et al.*, “Plasma processes and emission spectra in laser induced plasmas: A point of view,” *Spectrochim. Acta - Part B At. Spectrosc.*, vol. 100, pp. 180–188, 2014.
- [69] T. J. Rockstroh and J. Mazumder, “Spectroscopic studies of plasma during cw laser materials interaction,” *J. Appl. Phys.*, vol. 61, no. 917, 1987.
- [70] C. Phelps, C. J. Druffner, G. P. Perram, and R. R. Biggers, “Shock front dynamics in the pulsed laser deposition of YBa₂Cu₃O_{7-x},” *J. Phys. D. Appl. Phys.*, vol. 40, no. 15, pp. 4447–4453, 2007.
- [71] D. B. Geohegan, “Fast intensified-CCD photography of YBa₂Cu₃O_{7-x} laser ablation in vacuum and ambient oxygen,” *Appl. Phys. Lett.*, vol. 60, no. 22, pp. 2732–2734, 1992.
- [72] A. Kramida, Y. Ralchenko, J. Reader, and NIST Atomic Spectra Database Team, “NIST Atomic Spectra Database (version 5.3),” *National Institute of Standards and Technology, Gaithersburg, MD*. p. Available: <http://physics.nist.gov/asd>,

2015.

- [73] A. Kantrowitz and J. Grey, “A High Intensity Source for the Molecular Beam. Part I. Theoretical,” *Rev. Mod. Phys.*, vol. 22, no. 5, pp. 328–332, 1951.
- [74] J. B. Anderson and J. B. Fenn, “Velocity Distributions in Molecular Beams from Nozzle Sources,” *Phys. fluids*, vol. 8, no. 5, pp. 780–787, 1965.
- [75] J. P. Zheng, Z. Q. Huang, D. T. Shaw, and H. S. Kwok, “Generation of high-energy atomic beams in laser-superconducting target interactions,” *Appl. Phys. Lett.*, vol. 54, no. 3, pp. 280–282, 1989.
- [76] J. P. Zheng, Q. Y. Ying, S. Witanachchi, Z. Q. Huang, D. T. Shaw, and H. S. Kwok, “Role of the oxygen atomic beam in low-temperature growth of superconducting films by laser deposition,” *Appl. Phys. Lett.*, vol. 54, no. 10, pp. 954–956, 1989.
- [77] S. I. Anisimov, “Vaporization of metal absorbing laser radiation,” *Sov. Phys. JETP*, vol. 27, no. 1, pp. 182–183, 1969.
- [78] R. Kelly and R. W. Dreyfus, “On the effect of Knudsen-layer formation on studeis of vaporization, sputtering, and desorption,” *Surf. Sci.*, vol. 198, pp. 263–276, 1988.
- [79] R. . I. Acosta, K. C. Gross, and G. P. Perram, “Combustion kinetics of laser irradiated porous graphite from imaging Fourier transform spectroscopy,” *Combust. Flame*, vol. 163, pp. 90–99, 2014.
- [80] J. S. A. Brooke, P. F. Bernath, T. W. Schmidt, and G. B. Bacskay, “Line strengths and updated molecular constants for the C₂ Swan system,” *J. Quant. Spectrosc. Radiat. Transf.*, vol. 124, pp. 11–20, 2013.

- [81] G. Herzberg, *Spectra of Diatomic Molecules*, 2nd ed. New York: Litton, 1950.
- [82] M. Martin, “C2 spectroscopy and kinetics,” *J. Photochem. Photobiol. A Chem.*, vol. 66, no. 3, pp. 263–289, 1992.
- [83] J. S. A. Brooke, R. S. Ram, C. M. Western, G. Li, D. W. Schwenke, and P. F. Bernath, “Einstein A coefficients and oscillator strengths for the $A2\Pi - X2\Sigma^+$ (red) AND $B2\Sigma^+ - X2\Sigma^+$ (violet) systems and rovibrational transitions in the $X2\Sigma^+$ state of CN,” *Astrophys. J. Suppl. Ser.*, vol. 210, no. 23, pp. 1–15, 2014.
- [84] R. S. Ram, L. Wallace, and P. F. Bernath, “High resolution emission spectroscopy of the $A2\Pi - X2\Sigma^+$ (red) system of $^{12}C^{14}N$,” *J. Mol. Spectrosc.*, vol. 263, pp. 82–88, 2010.
- [85] R. S. Ram, D. P. Davis, L. Wallace, R. Engleman, D. R. T. Appadoo, and P. F. Bernath, “Fourier transform emission spectroscopy of the $B2\Sigma^+ - X2\Sigma^+$ system of CN,” *J. Mol. Spectrosc.*, vol. 237, pp. 225–231, 2006.
- [86] P. F. Bernath, *Spectra of atoms and molecules*, 2nd ed. New York: Oxford University Press, 2005.
- [87] A. Tanabashi, T. Hirao, T. Amano, and P. F. Bernath, “The Swan system of C2: A global analysis of Fourier transform emission spectra,” *Astrophys. J. Suppl. Ser.*, vol. 169, pp. 472–484, 2007.
- [88] A. A. Voevodin, J. G. Jones, J. S. Zabinski, and L. Hultman, “Plasma characterization during laser ablation of graphite in nitrogen for the growth of fullerene-like CN_x films,” *J. Appl. Phys.*, vol. 92, no. 2, pp. 724–735, 2002.
- [89] M. Musella, C. Ronchi, M. Brykin, and M. Sheindlin, “The molten state of graphite : An experimental study,” *J. Appl. Phys.*, vol. 84, no. 5, pp. 2530–2537,

- 1998.
- [90] C. Ronchi, R. Beukers, H. Heinz, J. P. Hiernaut, and R. Selfslag, “Graphite Melting Under Laser Pulse Heating,” *Int. J. Thermophys.*, vol. 13, no. 1, pp. 107–129, 1992.
- [91] A. Whittaker, P. Kintner, L. S. Nelson, and N. Richardson, “Carbon vapor pressure in the range 3450 to 4500K and evidence for melting at ~3800K,” *DTIC Rep. SD-TR-81-60*, pp. 1–59, 1981.
- [92] N. A. Gokcen, E. T. Chang, T. M. Poston, and D. J. Spencer, “Determination of Graphite-Liquid-Vapor,” *DTIC Rep. SAMSO-TR-76-29*, pp. 1–60, 1976.
- [93] A. V. Kirillin, M. D. Kovalenko, S. V. Romanenko, L. M. Kheifets, and M. A. Sheindlin, “Apparatus and method for examining the properties of refractory substances at high temperatures and pressure by stationay laser heating,” *Teplofiz. Vys. Temp*, vol. 24, no. 2, pp. 364–369, 1986.
- [94] A. V. Kirillin, M. . Kovalenko, M. A. Sheindlin, and V. S. Zhivopistsev, “Stationary laser heating in measuring the vapor pressure of carbon at 5000-7000K,” *Teplofiz. Vys. Temp*, vol. 23, no. 4, pp. 699–706, 1985.
- [95] R. Gosse, A. Rbat, W. Patterson, A. Force, S. Gogineni, and S. Roy, “Graphite ablation experiments in the LH MEL laser facility,” in *43rd AIAA Thermophysics Conference*, 2012, no. June, pp. 1–19.
- [96] R. J. Bartell *et al.*, “Methodology for comparing worldwide performance of diverse weight-constrained high energy laser systems,” *Proc. SPIE 5792*, vol. 76, 2005.
- [97] G. M. Fuge, M. N. R. Ashfold, and S. J. Henley, “Studies of the plume emission

- during the femtosecond and nanosecond ablation of graphite in nitrogen,” *J. Appl. Phys.*, vol. 99, pp. 1–12, 2006.
- [98] C. Vivien, J. Hermann, a Perrone, and C. Boulmer-Leborgne, “A study of molecule formation during laser ablation of graphite in low-pressure ammonia,” *J. Phys. D. Appl. Phys.*, vol. 32, no. 4, pp. 518–528, 1999.
- [99] C. Amiot, “Fourier Spectroscopy of the $^{12}\text{C}_2$, $^{13}\text{C}_2$, and $^{12}\text{C}^{13}\text{C}$ (0-0) Swan bands,” *Astrophys. J. Suppl. Ser.*, vol. 52, pp. 329–340, 1983.
- [100] G. M. Lloyd and P. Ewart, “High resolution spectroscopy and spectral simulation of C_2 using degenerate four-wave mixing,” *J. Chem. Phys.*, vol. 110, no. 1, pp. 385–392, 1999.
- [101] E. J. Bakker, E. F. Van Dishoeck, L. B. F. M. Waters, and T. Schoenmaker, “Circumstellar C_2 , CN , and CH^+ in the optical spectra of post-AGB stars,” *Astron. Astrophys.*, vol. 323, pp. 469–487, 1997.
- [102] C. Sneden and D. L. Lambert, “The CN red system in the Solar spectrum,” *Astrophys. J.*, vol. 259, pp. 381–391, 1982.
- [103] D. L. Lambert and A. C. Danks, “High-resolution spectra of C_2 Swan bands from Comet West 1976 VI,” *Astrophys. J.*, vol. 268, pp. 428–446, 1983.
- [104] D. L. Lambert, Y. Sheffer, A. C. Danks, C. Arpigny, and P. Magain, “High-Resolution Spectroscopy of the C_2 Swan 0-0 Band from Comet P/Halley,” *Astrophys. J.*, vol. 353, pp. 640–653, 1990.
- [105] S. W. Lewis, R. G. Morgan, T. J. McIntyre, C. R. Alba, and R. B. Greendyke, “Expansion Tunnel Experiments of Earth Reentry Flow with Surface Ablation,” *J. Spacecr. Rockets*, vol. 53, pp. 887–899, 2016.

- [106] C. O. Asma, B. Helver, T. Magin, and O. P. Chazot, "Spectroscopy Measurements on Ablation Testing In High Enthalpy Plasma Flows," *AFLR-AFOSR-UK-TR Rep. VKI CR 2010-181*, pp. 1–47, 2010.
- [107] S. J. Firchow and K. L. Menningen, "Radical density measurements in an atmospheric pressure oxyacetylene torch," *J. Phys. D. Appl. Phys.*, vol. 32, pp. 937–941, 1999.
- [108] D. B. Geohegan and A. A. Puretzky, "Dynamics of laser ablation plume penetration through low pressure background gases," *Appl. Phys. Lett.*, vol. 67, no. 1995, p. 197, 1995.
- [109] S. S. Chu and C. P. Grigoropoulos, "Determination of Kinetic Energy Distribution in a Laser-Ablated Titanium Plume by Emission and Laser-Induced Fluorescence Spectroscopy," *J. Heat Transfer*, vol. 122, no. 4, p. 771, 2000.
- [110] V. C. Dinca *et al.*, "Nickel-titanium alloy: Cytotoxicity evaluation on microorganism culture," *Appl. Surf. Sci.*, vol. 252, no. 13 SPEC. ISS., pp. 4619–4624, 2006.
- [111] Y. Suda, H. Kawasaki, T. Ueda, and T. Ohshima, "Preparation of high quality nitrogen doped TiO₂ thin film as a photocatalyst using a pulsed laser deposition method," vol. 454, pp. 162–166, 2004.
- [112] M. Ye and C. P. Grigoropoulos, "Time-of-flight and emission spectroscopy study of femtosecond laser ablation of titanium," *J. Appl. Phys.*, vol. 89, no. 9, pp. 5183–5190, 2001.
- [113] S. Eliezer *et al.*, "Synthesis of nanoparticles with femtosecond laser pulses," *Phys. Rev. B - Condens. Matter Mater. Phys.*, vol. 69, no. 14, pp. 144119-1-144119-6,

2004.

- [114] S. Amoruso *et al.*, “Generation of silicon nanoparticles via femtosecond laser ablation in vacuum,” vol. 4502, no. 2004, 2014.
- [115] S. Amoruso, M. Armenante, V. Berardi, R. Bruzzese, and N. Spinelli, “Absorption and saturation mechanisms in aluminium laser ablated plasmas,” vol. 271, pp. 265–271, 1997.
- [116] G. Callies, P. Berger, and H. Hugel, “Time-Resolved Observation of Gas-Dynamic Discontinuities Arising During Excimer-Laser Ablation and Their Interpretation,” *J. Phys. D-Applied Phys.*, vol. 28, no. 4, pp. 794–806, 1995.
- [117] G. Abdellatif and H. Imam, “A study of the laser plasma parameters at different laser wavelengths,” *Spectrochim. Acta Part B*, vol. 57, pp. 1155–1165, 2002.
- [118] S. S. Harilal, B. O’Shay, Y. Tao, and M. S. Tillack, “Ambient gas effects on the dynamics of laser-produced tin plume expansion,” *J. Appl. Phys.*, vol. 99, no. 8, 2006.
- [119] N. Farid, S. S. Harilal, H. Ding, and A. Hassanein, “Emission features and expansion dynamics of nanosecond laser ablation plumes at different ambient pressures,” *J. Appl. Phys.*, vol. 115, no. 3, 2014.
- [120] K. Sasaki, S. Matsui, H. Ito, and K. Kadota, “Dynamics of laser-ablation Ti plasmas studied by laser-induced fluorescence imaging spectroscopy,” *J. Appl. Phys.*, vol. 92, no. 11, pp. 6471–6476, 2002.
- [121] S. S. Harilal, C. V. Bindhu, M. S. Tillack, F. Najmabadi, and A. C. Gaeris, “Internal structure and expansion dynamics of laser ablation plumes into ambient gases,” *J. Appl. Phys.*, vol. 93, no. 5, pp. 2380–2388, 2003.

- [122] A. E. Hussein, P. K. Diwakar, S. S. Harilal, and A. Hassanein, "The role of laser wavelength on plasma generation and expansion of ablation plumes in air," *J. Appl. Phys.*, vol. 113, no. 14, 2013.
- [123] A. A. I. Khalil, M. Richardson, L. Johnson, and M. A. Gondal, "Titanium Plasma Spectroscopy Studies under Double Pulse Laser Excitation," *Laser Phys.*, vol. 19, no. 10, pp. 1981–1992, 2009.
- [124] W. Sdorra, J. Brust, and K. Niemax, "Basic investigations for laser microanalysis: IV. The dependence on the laser wavelength in laser ablation," *Mikrochim. Acta*, vol. 108, no. 1–2, pp. 1–10, 1992.
- [125] Y. Iida, "Effects of atmosphere on laser vaporization and excitation processes of solid samples," *Spectrochim. Acta Part B At. Spectrosc.*, vol. 45, no. 12, pp. 1353–1367, 1990.
- [126] L. Torrisi *et al.*, "Metallic etching by high power Nd : yttrium – aluminum – garnet pulsed laser irradiation," *Rev. Sci. Instrum.*, vol. 71, no. 11, pp. 4330–4334, 2000.
- [127] R. Timm, P. R. Willmott, and J. R. Huber, "Ablation and blow off characteristics at 248 nm of Al, Sn and Ti targets used for thin film pulsed laser deposition," *J. Appl. Phys.*, vol. 80, p. 1794, 1996.
- [128] N. Arnold, B. Luk'yanchuk, and N. Bityurin, "A fast quantitative modelling of ns laser ablation based on non-stationary averaging technique," *Appl. Surf. Sci.*, vol. 127–129, pp. 184–192, 1998.
- [129] L. Torrisi, F. Caridi, A. Picciotto, and A. Borrielli, "Energy distribution of particles ejected by laser-generated aluminium plasma," *Nucl. Instruments Methods Phys. Res. B*, vol. 252, pp. 183–189, 2006.

- [130] L. M. Cabalin and J. J. Laserna, “Experimental determination of laser induced breakdown thresholds of metals under nanosecond Q-switched laser operation,” vol. 8547, no. 98, 1998.
- [131] W. Sdorra and K. Niemax, “Basic investigations for laser microanalysis: III. Application of different buffer gases for laser-produced sample plumes,” *Mikrochim. Acta*, vol. 107, no. 3–6, pp. 319–327, 1992.
- [132] S. Preuss, A. Demchuk, and Stuke, “Sub-picosecond UV laser ablation of metals,” *Appl. Phys. A Mater. Sci. Process.*, vol. 61, pp. 33–37, 1995.
- [133] F. Claeysens, S. J. Henley, and M. N. R. Ashfold, “Comparison of the ablation plumes arising from ArF laser ablation of graphite, silicon, copper, and aluminum in vacuum,” *J. Appl. Phys.*, vol. 94, no. 4, pp. 2203–2211, 2003.
- [134] A. Vertes, R. Gijbels, and F. Adams, *Chemical Analysis Vol 124 Laser Ionization Mass Analysis*. New York: John Wiley & Sons, Inc., 1993.
- [135] D. L. Jones, “National Bureau of Standards Technical Note 155 The Energy Parameter B for Strong Blast Waves,” Boulder, CO, 1962.
- [136] A. Misra, A. Mitra, and R. K. Thareja, “Diagnostics of laser ablated plasmas using fast photography,” *Appl. Phys. Lett.*, vol. 74, no. 7, pp. 929–931, 1999.
- [137] R. B. Hall, “Laser Production of Blast Waves in Low Pressure Gases,” *J. Appl. Phys.*, vol. 40, no. 4, pp. 1941–1945, 1969.
- [138] W. A. Bauer, G. P. Perram, and T. Haugan, “Comparison of plume dynamics for laser ablated metals: Al and Ti,” *Awaiting Submiss.*, 2017.
- [139] L. Torrisi, D. Mascali, I. Istituto, and F. Nucleare, “Measurements of electron energy distribution in tantalum laser-generated plasma,” *J. Appl. Phys.*, vol. 107,

- no. 123303, pp. 1–8, 2010.
- [140] J. Maul, S. Karpuk, and G. Huber, “Bimodal velocity distribution of atoms released from nanosecond ultraviolet laser ablation,” *Phys. Rev. B*, vol. 71, no. 45428, pp. 1–5, 2005.
- [141] P. E. Dyer, R. D. Greenough, A. Issa, and P. H. Key, “Spectroscopic and ion probe measurements of KrF laser ablated Y-Ba-Cu-O bulk samples S,” *Appl. Phys. Lett.*, vol. 53, no. 6, pp. 534–536, 1988.
- [142] V. N. Burimov, A. N. Zherikhin, and V. L. Popkov, “Velocity distribution of Ba + ions in a plasma formed by laser ablation of a high-temperature superconducting target,” *Quantum Electron.*, vol. 25, no. 11, pp. 1060–1062, 1995.
- [143] D. B. Geohegan and D. N. Mashburn, “Characterization of ground-state neutral and ion transport during laser ablation of Y1Ba2Cu3O7-x using transient optical absorption spectroscopy,” *Appl. Phys. Lett.*, vol. 55, no. 22, pp. 2345–2347, 1989.
- [144] C. J. Druffner, P. D. Kee, M. A. Lange, G. P. Perram, R. R. Biggers, and P. N. Barnes, “Optical diagnostics for pulsed laser ablation,” *J. Dir. Energy*, vol. 1, no. 3, pp. 203–218, 2005.
- [145] L. V Zhigilei and B. J. Garrison, “Velocity distributions of molecules ejected in laser ablation,” *Appl. Phys. Lett.*, vol. 71, no. April, pp. 551–553, 1997.
- [146] G. W. Martin *et al.*, “Study of ground-state titanium ion velocity distributions in laser-produced plasma plumes,” *Appl. Phys. Lett.*, vol. 74, no. 23, pp. 3465–3467, 1999.
- [147] Y. Nakata, T. Okada, and M. Maeda, “Time-of-Flight Distributions of Si Atoms Ejected by KrF Laser Ablation of Si3N4,” *Jpn. J. Appl. Phys.*, vol. 34, no. 8A, pp.

4079–4080, 1995.

- [148] R. Kelly *et al.*, “Gas-dynamic effects in the laser-pulse sputtering of AlN: is there evidence for phase explosion?,” *Appl. Surf. Sci.*, vol. 133, no. 4, pp. 251–269, 1998.
- [149] R. F. Wood, J. N. Leboeuf, D. B. Geohegen, A. A. Puretzky, and K. R. Chen, “Dynamics of plume propagation and splitting during pulsed-laser ablation of Si in He and Ar,” *Phys. Rev. B*, vol. 58, no. 3, pp. 1553–1543, 1998.
- [150] L. D. Landau and E. M. Lifshitz, *Mechanics*, 3rd ed. Oxford: Pergamon Press, 1976.
- [151] G. L. Miessler and D. A. Tarr, *Inorganic Chemistry*, 3rd ed. Northfield: Pearson Education Inc., 2004.

REPORT DOCUMENTATION PAGE				<i>Form Approved</i> OMB No. 074-0188	
<p>The public reporting burden for this collection of information is estimated to average 1 hour per response, including the time for reviewing instructions, searching existing data sources, gathering and maintaining the data needed, and completing and reviewing the collection of information. Send comments regarding this burden estimate or any other aspect of the collection of information, including suggestions for reducing this burden to Department of Defense, Washington Headquarters Services, Directorate for Information Operations and Reports (0704-0188), 1215 Jefferson Davis Highway, Suite 1204, Arlington, VA 22202-4302. Respondents should be aware that notwithstanding any other provision of law, no person shall be subject to a penalty for failing to comply with a collection of information if it does not display a currently valid OMB control number.</p> <p>PLEASE DO NOT RETURN YOUR FORM TO THE ABOVE ADDRESS.</p>					
1. REPORT DATE (DD-MM-YYYY) 14-09-2017		2. REPORT TYPE Doctoral Dissertation		3. DATES COVERED (From – To) August 2013 – September 2017	
TITLE AND SUBTITLE Laser Heating of Graphite and Pulsed Laser Ablation of Titanium and Aluminum				5a. CONTRACT NUMBER	
				5b. GRANT NUMBER	
				5c. PROGRAM ELEMENT NUMBER	
6. AUTHOR(S) Bauer, William A., Captain, USAF				5d. PROJECT NUMBER	
				5e. TASK NUMBER	
				5f. WORK UNIT NUMBER	
7. PERFORMING ORGANIZATION NAMES(S) AND ADDRESS(S) Air Force Institute of Technology Graduate School of Engineering and Management (AFIT/EN) 2950 Hobson Way, Building 640 WPAFB OH 45433-8865				8. PERFORMING ORGANIZATION REPORT NUMBER AFIT-ENP-DS-17-S-020	
9. SPONSORING/MONITORING AGENCY NAME(S) AND ADDRESS(ES) High Energy Laser Joint Technology Office 901 University Blvd. SE, Suite 100, Albuquerque, NM 87106 505-248-8208, harro.ackermann@jto.hpc.mil ATTN: Dr. Harro Ackermann				10. SPONSOR/MONITOR'S ACRONYM(S) HEL-JTO	
				11. SPONSOR/MONITOR'S REPORT NUMBER(S)	
12. DISTRIBUTION/AVAILABILITY STATEMENT DISTRUBTION STATEMENT A. APPROVED FOR PUBLIC RELEASE; DISTRIBUTION UNLIMITED.					
13. SUPPLEMENTARY NOTES This material is declared a work of the U.S. Government and is not subject to copyright protection in the United States.					
14. ABSTRACT Tactical missions for laser weapons include a wide variety of targets, increasing the demands on the laser lethality community. New approaches to reducing the dimensionality of laser and materials interactions are necessary to increase predictive capability. Self-contained systematic experimental study was conducted on continuous wave and pulsed laser interaction with graphite, Al, and Ti. The spectroscopy and plume dynamics from the heating and ablation of these materials was examined to characterize laser weapons effects, develop graphite response for thermal protection systems, and provide optical diagnostics for materials processing. Furthermore, analysis of ablated plume velocity distributions shows application of conventional Maxwell-Boltzmann distribution is inadequate, particularly for expansion into pressure environment.					
15. SUBJECT TERMS Graphite, cw laser, CN, C ₂ , Pulsed Laser Ablation, Metals, Fast Emissions Imaging, Shock Front, Velocity Distribution					
16. SECURITY CLASSIFICATION OF:			17. LIMITATION OF ABSTRACT UU	18. NUMBER OF PAGES 147	19a. NAME OF RESPONSIBLE PERSON Dr. Glen P. Perram, AFIT/ENP
a. REPORT U	b. ABSTRACT U	c. THIS PAGE U			19b. TELEPHONE NUMBER (Include area code) (937) 255-6565, ext 4504 Glen.Perram@afit.edu